

Titre: Thin Coatings for Heavy Industry: Advanced Coatings for Pipes and Valves
Title: Valves

Auteur: Luc Vernhes
Author:

Date: 2015

Type: Mémoire ou thèse / Dissertation or Thesis

Référence: Vernhes, L. (2015). Thin Coatings for Heavy Industry: Advanced Coatings for Pipes and Valves [Thèse de doctorat, École Polytechnique de Montréal]. PolyPublie.
Citation: <https://publications.polymtl.ca/1686/>

 **Document en libre accès dans PolyPublie**
Open Access document in PolyPublie

URL de PolyPublie: <https://publications.polymtl.ca/1686/>
PolyPublie URL:

Directeurs de recherche: Ludvik Martinu, & Jolanta-Ewa Sapiuha
Advisors:

Programme: Génie physique
Program:

UNIVERSITÉ DE MONTRÉAL

THIN COATINGS FOR HEAVY INDUSTRY:
ADVANCED COATINGS FOR PIPES AND VALVES

LUC VERNHES
DÉPARTEMENT DE GÉNIE PHYSIQUE
ÉCOLE POLYTECHNIQUE DE MONTRÉAL

THÈSE PRÉSENTÉE EN VUE DE L'OBTENTION
DU DIPLÔME DE PHILOSOPHIÆ DOCTOR
(GÉNIE PHYSIQUE)
FÉVRIER 2015

UNIVERSITÉ DE MONTRÉAL

ÉCOLE POLYTECHNIQUE DE MONTRÉAL

Cette thèse intitulée:

THIN COATINGS FOR HEAVY INDUSTRY:
ADVANCED COATINGS FOR PIPES AND VALVES

présentée par : VERNHES Luc

en vue de l'obtention du diplôme de : Philosophiæ Doctor

a été dûment acceptée par le jury d'examen constitué de :

Mme SANTATO Clara, Doctorat, présidente

Mme KLEMBERG-SAPIEHA Jolanta-Ewa, Doctorat, membre et directrice de recherche

M. MARTINU Ludvik, Ph. D., membre et codirecteur de recherche

M. LÉVESQUE Martin, Ph. D., membre

M. MOREAU Christian, Ph. D., membre externe

“To Sophie, who makes this extraordinary journey possible.”

ACKNOWLEDGMENTS

I thank the French government for enabling me to benefit from an advanced educational system oriented toward entrepreneurship, and for opening up my horizons. I thank the Canadian government for welcoming me as an immigrant and for facilitating my integration at the highest professional and academic levels.

I thank Pascal Broeckx, who gave me the opportunity to join the Velan Granby laboratory in 2003, where I was exposed to my first tribological challenges while developing new products. I would like to thank the rest of the Velan Engineering management team, especially Rana Bose and Gil Perez, for all the other opportunities they have given me since then, and for maintaining the pressure at work while I was pursuing my academic career at full steam. I would like to thank all the Velan staff who have contributed to this work in one way or another, including Mirek Hubacek, Vahe Najarian, Christian Beguian, Bernard Gelineau, Mario Beaumier, Grégorio Balagot, Jérôme Bélanger, Subhash Saini, Simon Bricteux, Rwa Salman, and Nicolas Lourdel. I also thank the Velan family for their pragmatic, business-oriented vision, their science philanthropy, and their long-term commitment to support research, product innovation, and technology in Montreal.

I thank Polytechnique Montréal for making it possible to pursue my engineering studies in parallel with a professional career. I wish to extend special thanks to my thesis directors Professor Jolanta Ewa Klemberg-Sapieha and Professor Ludvik Martinu for admitting me to the Functional Coating and Surface Engineering Laboratory (FCSEL). I thank the entire FCSEL group for integrating a rather unconventional candidate who was rarely present during regular hours. I would especially like to thank my coauthors Marwan Azzi, Duanjie Li, and Etienne Bousser for their substantial contributions.

I would like also to thank the National Research Council Industrial Materials Institute (NRC-IMI) for their instrumental support for this project. I would particularly like to thank Dominique Poirier and Rogerio Lima for their significant contributions as coauthors and for all our fruitful exchanges. Thermal spray and weld overlays were new to FCSEL when I began my thesis, and

the intense discussions with Dominique and Rogerio were tremendously helpful for understanding these coating processes.

I would also like to thank all the partners I had the immense pleasure of working with during those five years, especially Danie de Wet, David Lee, and Matthew Yao at Kennametal Stellite, who generously lent their expertise to help refine my understanding of both thermal sprays and weld overlays. I would also like to mention the helpful linguistic editing by Margaret McKyes.

Finally, I would like to express my immense gratitude to my family, who supported me without begrudging the evenings, week-ends, paternity leaves, and vacations I spent managing simultaneous professional and academic careers.

RÉSUMÉ

La robinetterie et la tuyauterie industrielles sont des appareils sous pression qui permettent de réguler le flux de matériaux (liquides, gaz et boues) en contrôlant les sections de passages. L'optimisation des processus, la réduction des coûts et les réglementations gouvernementales exigent des équipementiers de maintenir leurs produits à la fine pointe de la technologie. La robinetterie a été développée il y a plus de 3000 ans pour alimenter en eau les fermes et les villes en utilisant des alliages de bronze, qui fournissent à la fois une résistance à la corrosion et des performances tribologiques acceptables. Durant la révolution industrielle, ces antiques robinets ont évolué et des matériaux tribologiques plus modernes tels que les alliages Monel cuivre-nickel, Stellite cobalt-chrome, et le chromage dur appliqué par placage électrolytique ont été développés au début du XX^e siècle pour optimiser le comportement tribologique et maximiser la durée de vie en service de ces équipements. Depuis cette époque, de nouveaux matériaux ont été régulièrement introduits pour étendre le champ d'application de la robinetterie tel que le fluoropolymère téflon, pour contrôler certains produits chimiques nécessaire aux procédés pétrochimiques, les superalliages à base nickel Hastelloy et Inconel pour les applications pétrochimiques et les aciers riches en chrome F91 pour les centrales supercritiques. Plus récemment, l'industrie de la robinetterie a adopté l'utilisation des revêtements appliqués par projection thermique pour les applications les plus difficiles et continu d'investir massivement dans la recherche de revêtements plus performants pour chaque application. Il est de plus en plus évident que la solution optimale aux problèmes d'usure érosive, corrosive et par frottement rencontrés dans la robinetterie réside dans la conception et la fabrication de revêtements multicouches, nanostructurés qui contrôlent à la fois la dureté et l'élasticité, tout en assurant une bonne adhérence. Les objectifs généraux de cette thèse sont donc de réaliser, pour la tuyauterie et la robinetterie industrielles, l'état de l'art des revêtements protecteurs durs contrôlés structurellement offrant des propriétés mécaniques, élasto-plastiques et thermiques sur mesure et de développer des solutions innovantes pour améliorer la résistance au frottement, à l'érosion et à la corrosion et autres caractéristiques adaptées.

À partir de ces objectifs généraux, trois objectifs spécifiques ont été identifiés : 1) Sélectionner et évaluer les meilleurs candidats pour remplacer le chromage dur qui a été classé par l'agence

étatsunienne pour la protection de l'environnement (EPA) comme un processus irrespectueux de l'environnement; 2) Enquêter sur les défaillances récurrentes du revêtement HVOF $\text{Cr}_3\text{C}_2\text{-NiCr}$ appliquée par projection thermique sur l'Inconel 718 PH lorsqu'il est exposé à des chocs thermiques présent dans les centrales électriques conventionnelles supercritiques et à cycles combinés, l'objectif étant de comprendre la cause des échecs de ce revêtement et d'évaluer des solutions de revêtements possibles pour pallier à ces défaillances; 3) Développer de nouvelles architectures de revêtements multicouches, et de comprendre les propriétés tribo-mécaniques qui en résultent. Les principaux résultats sont présentés sous la forme d'articles dans des revues révisés par des pairs.

Dans le premier article, une variété de revêtements ne contenant pas de chrome ont été évalués comme solutions de rechange au chromage dur (HC), tels que le cobalt-phosphore nanostructuré (NCP) appliqué par placage électrolytique et le carbure de tungstène/tungstène (W/WC) déposé en phase vapeur. Une série d'essai de dureté, de micro rayures, de friction bille-sur-plan et de polarisation électrochimique a été effectuée afin de comparer les performances de différents revêtements. En outre, la résistance mécanique et la résistance à la fatigue ont été évaluées à l'aide de prototypes exposés à des conditions d'essais sévères. Le revêtement W/WC a présenté une résistance supérieure à l'usure et à la corrosion en raison de sa dureté élevée et de sa haute résistance à la corrosion, tandis que le revêtement NCP a offert une meilleure résistance à l'usure que le chromage dur dans certaines conditions et un potentiel de corrosion faible ce qui permet de l'utiliser comme revêtement de protection. Les revêtements nanostructurés ont donc présenté des caractéristiques prometteuses par rapport au chrome dur.

Le second article présente une analyse des modes de défaillance d'un revêtement HVOF 80/20 $\text{Cr}_3\text{C}_2\text{-NiCr}$ protégeant des boisseaux sphériques à portées métalliques d'isolation utilisés dans les lignes de vapeur supercritique de centrales électriques et ainsi que la qualification de revêtements alternatifs qui se sont montrés moins sensibles à ce mode de défaillance. Le revêtement HVOF 80/20 $\text{Cr}_3\text{C}_2\text{-NiCr}$ est utilisé pour protéger des milliers de robinets sans incident. Cependant, dans ce cas spécifique, les robinets sont exposés à des variations rapides de pression et de température entraînant une situation unique où le revêtement fissure. Il a été constaté que la précipitation de carbure est un facteur majeur causant la fragilisation du

revêtement. Une fois que la dureté augmente et que la ductilité est réduite, les contraintes thermiques, mécaniques et résiduelles peuvent initier et propager des fissures, provoquant la défaillance du revêtement lorsqu'il est exposé à des chocs thermiques. Pour pallier à ce problème, des solutions de rechange ont été évaluées.

Le troisième article présente les propriétés mécanique, tribologique, et la résistance à la corrosion de deux nouveaux revêtements hybrides: 1) une couche supérieure de W/WC et une couche intermédiaire de rechargement dur d'alliage chrome-cobalt (Co-Cr) (Stellite 6) appliquée sur un substrat d'acier inoxydable 316; et 2) une couche supérieure W/WC et une couche intermédiaire Ni-W-Cr-B déposé par HVOF et refondu (Colmonoy 88) appliquée sur un substrat d'Inconel 718. La diffractométrie par rayons X, l'analyse dispersive en énergie et la microscopie électronique à balayage ont été utilisés pour l'analyse de la microstructure de ces revêtements hybrides. La microindentation a été utilisée pour mesurer la dureté de surface et le profil de dureté des systèmes de revêtements. L'indentation Rockwell a servi à évaluer l'adhérence du revêtement selon la norme ISO CEN/TS 1071-8. La capacité de charge a été évaluée en mesurant la micro- et macroduretés à des charges élevées. Les propriétés tribologiques ont été évaluées avec un tribomètre linéaire alternatif bille-sur-plan, et la résistance à la corrosion a été mesurée par la technique de polarisation potentiodynamiques et la spectroscopie d'impédance électrochimique.

ABSTRACT

Pipes and valves are pressure vessels that regulate the flow of materials (liquids, gases, and slurries) by controlling the passageways. To optimize processes, reduce costs, and comply with government regulations, original equipment manufacturers (OEMs) must maintain their products in state-of-the-art condition.

The first valves were invented over 3,000 years ago to supply water to farms and cities. They were made with bronze alloys, providing good corrosion resistance and acceptable tribological performance. The industrial revolution drove manufacturers to develop new and improved tribological materials. In the 20th century, innovative alloys such as Monel copper–nickel and Stellite cobalt-chrome as well as hard chrome plating were introduced to better control tribological properties and maximize in-service life. Since then, new materials have been regularly introduced to extend the range of applications for valves. For example, Teflon fluoropolymers are used in corrosive chemical and petrochemical processes, the nickel-based superalloys Hastelloy and Inconel for petrochemical applications, and creep-resistant chromium-rich F91 steel for supercritical power plants. Recently, the valve industry has embraced the use of hard thermal sprayed coatings for the most demanding applications, and is investing heavily in research to develop the most suitable coatings for specific uses. There is increasing evidence that the optimal solution to erosive, corrosive, and fretting wear problems lies in the design and manufacture of multi-layer, graded, and/or nanostructured coatings and coating systems that combine controlled hardness with high elastic modulus, high toughness, and good adhesion. The overall objectives of this thesis were 1) to report on advances in the development of structurally controlled hard protective coatings with tailored mechanical, elastoplastic, and thermal properties; and 2) to describe enhanced wear-, erosion-, and corrosion-resistance and other characteristics suitable for applications such as pipes and valves.

From these general objectives, three specific objectives were derived: 1) to select and assess the best candidates for alternatives to hard chromium electroplating, which has been classified by the U.S. Environmental Protection Agency (EPA) as an environmentally unfriendly process; 2) to investigate recurrent failures occurring in the field with thermal sprayed HVOF Cr₃C₂-NiCr coating applied to Inconel 718 PH when exposed to supercritical steam lines and thermal shocks

in supercritical power plants (determining the root causes of coating failures and assessing potential coating alternatives to alleviate these issues); and 3) to develop new coating architectures, including complex microstructures and interfaces, and to better understand and optimize complex tribomechanical properties. The main results are presented in the form of articles in peer-reviewed journals.

In the first article, a variety of chromium-free protective coatings were assessed as alternatives to hard chromium (HC) electroplating, such as nanostructured cobalt-phosphor (NCP) deposited by electroplating and tungsten/tungsten carbide (W/WC) applied by chemical vapor deposition. In order to compare performance across the coatings, a series of laboratory tests were performed, including hardness, microscratch, pin-on-disk, and electrochemical polarization measurements. Mechanical and fatigue resistance were also determined using prototype valves with coated ball under severe tribocorrosion conditions. It was found that W/WC coating exhibits superior wear and corrosion resistance due to high hardness and high pitting resistance, respectively, whereas NCP exhibits better wear resistance than HC with alumina ball as well as low corrosion potential, making it suitable for use as sacrificial protective coating. Both nanostructured coatings exhibited superior tribomechanical and functional characteristics compared to HC.

The second article presents an investigation of an HVOF 80/20 Cr_3C_2 -NiCr coating failure in an on-off metal-seated ball valve (MSBV) used in supercritical steam lines in a power plant, along with an assessment of alternative coating solutions that are less susceptible to this failure mode. HVOF 80/20 Cr_3C_2 -NiCr coating has been used to protect thousands of MSBVs without incident. However, in this case the valves were challenged with exposure to rapid variations in high-pressure flow and temperature, resulting in a unique situation that caused the coating to undergo cracking and cohesive failure. Carbide precipitation was found to be a major factor, resulting in coating embrittlement. Reduced coating toughness and ductility allowed thermal, mechanical, and residual stresses to initiate cracks and propagate them more easily, leading to coating failure with exposure to thermal shock. To alleviate these issues, possible coating alternatives were assessed.

The third article presents the mechanical, tribological, and corrosion properties of two novel hybrid coating systems: 1) a tungsten–tungsten carbide (W-WC) top layer and a laser cladded cobalt–chromium (Co-Cr) interlayer (Stellite® 6 superalloy) applied to a 316 stainless steel substrate; and 2) the same W-WC top layer and an HVOF spray-and-fused Ni-W-Cr-B interlayer (Colmonoy® 88 superalloy) applied to an Inconel® 718 substrate. X-ray diffraction, energy dispersive spectroscopy, and scanning electron microscopy were used to analyze the microstructure of the coating layers. Microindentation was used to measure surface hardness and the hardness profile of the coating systems. Rockwell indentation was used to assess coating adhesion according to CEN/TS 1071-8. Surface load-carrying capacity was also assessed by measuring micro- and macrohardness at high loads. Tribological properties were assessed with a linear reciprocating ball-on-flat sliding wear test, and corrosion resistance was measured by potentiodynamic polarization and electrochemical impedance spectroscopy.

TABLE OF CONTENTS

AKNOWLEDGMENTS	IV
RÉSUMÉ	VI
ABSTRACT	IX
TABLE OF CONTENTS.....	XII
LIST OF TABLES	XVI
LIST OF FIGURES	XVII
LIST OF ACRONYM AND SYMBOLS	XXI
LIST OF APPENDICES	XXVI
CHAPTER 1 INTRODUCTION.....	1
CHAPTER 2 LITERATURE REVIEW	13
2.1. Surface engineering methods applied to valves	13
2.1.1. Historical development	13
2.1.2. State-of-the-art materials and challenges.....	17
2.2. Surface engineering techniques	28
2.2.1. Surface modification	28
2.2.2. Coating deposition	31
2.3. Surface mechanical response	49
2.3.1. Hardness.....	49
2.3.2. Modulus of elasticity.....	52
2.3.3. Toughness	53
2.3.4. Load-carrying capacity	54
2.3.5. Adhesion	55
2.3.6. Thermal expansion.....	57

CHAPTER 3	EXPERIMENTAL METHODOLOGY	58
3.1.	Mechanical characterization	58
3.1.1.	Microhardness	58
3.1.2.	Load-carrying capacity	58
3.1.3.	Nanohardness and modulus of elasticity.....	58
3.1.4.	Scratch hardness.....	60
3.1.5.	Sliding wear resistance	60
3.1.6.	Friction coefficients	60
3.1.7.	Bond strength	61
3.1.8.	Dry sand abrasion resistance	61
3.1.9.	Wet sand abrasion resistance	61
3.1.10.	Variable temperature galling resistance.....	62
3.2.	Structure and chemical composition.....	63
3.2.1.	Scanning electron microscopy	63
3.2.2.	X-ray diffraction	63
3.2.3.	Crystallinity index.....	64
3.3.	Functional testing	64
3.3.1.	Corrosion.....	64
3.3.2.	Endurance cycle testing	65
3.3.3.	Aging test	65
3.3.4.	Thermal shock test	65
CHAPTER 4	ARTICLE 1: ALTERNATIVES FOR HARD CHROMIUM PLATING: NANOSTRUCTURED COATINGS FOR SEVERE-SERVICE VALVES	67
4.1.	Introduction	67
4.2.	Experimental.....	69

4.2.1. Material	69
4.2.2. Characterization techniques	69
4.3. Results and discussion	72
4.3.1. Microstructure	72
4.3.2. Tribo-mechanical properties	74
4.3.3. Corrosion properties.....	78
4.3.4. Functional properties	80
4.4. Conclusions	82
4.5. Acknowledgements	82
CHAPTER 5 ARTICLE 2: HVOF COATING CASE STUDY FOR POWER PLANT PROCESS CONTROL BALL VALVE APPLICATION.	83
5.1. Introduction	84
5.2. Failure analysis	85
5.2.1. Experimental methodology	87
5.2.2. Results.....	89
5.2.3. Discussion	95
5.3. Solution.....	97
5.4. Conclusion	101
5.5. Acknowledgements	101
CHAPTER 6 ARTICLE 3: HYBRID Co-Cr / W-WC AND Ni-W-Cr-B / W-WC COATING SYSTEMS.....	102
6.1. Introduction	103
6.2. Experimental.....	105
6.2.1. Materials	105
6.2.2. Characterization methods.....	107
6.2.3. Microstructure.....	107

6.2.4. Tribo-mechanical properties	107
6.2.5. Corrosion properties.....	108
6.3. Results and discussion	109
6.3.1. Microstructure.....	109
6.3.2. Tribo-mechanical properties	111
6.3.3. Corrosion properties.....	117
6.4. Conclusions	121
6.5. Acknowledgements	122
CHAPTER 7 GENERAL DISCUSSION, CONCLUSION AND PERSPECTIVES	123
REFERENCES	132
APPENDICES	150

LIST OF TABLES

Table 1: Peer-reviewed publications.....	10
Table 2: Peer-reviewed publications written in collaboration	10
Table 3: Working paper	10
Table 4: Conference proceedings and poster presentations	10
Table 5: Patents.....	12
Table 6: Memberships.....	12
Table 2.1: Norem 02 nominal composition (mass %) and physical properties	20
Table 2.2: Nominal composition of Stellite 6 (mass %) and physical properties.....	34
Table 2.3: Most commonly used TS coatings for severe-service valves [119].	43
Table 4.1: Corrosion parameters.....	79
Table 5.1: Comparison of failed versus new HVOF 80/20 Cr ₃ C ₂ + [80Ni-20Cr] coating and OEM specification.	89
Table 5.2: Nanohardness of the oxide phase compared to the Cr ₃ C ₂ phase and the overall coating nanohardness.	91
Table 5.3: Crystallinity Indices of powder, “as sprayed” and aged coating of the original HVOF coating.....	93
Table 5.4: List of potential solutions	98
Table 5.5: Crystallinity Indices of powder and “as sprayed” HVOF coating.....	100
Table 6.1: Chemical composition and physical properties.	106
Table 6.2: Microhardness obtained on cross section.	112
Table 6.3: Surface hardness measurements.	114
Table 6.4: EIS spectra simulation results.....	119
Table 6.5: Corrosion current i_o and breakdown potential E_b for each coating system.....	120
Table A.1: Spraying parameters.	154
Table A.2: Variable temperature galling test procedure.	158
Table A.3: Coating properties.....	161

LIST OF FIGURES

Figure 1: Ancient Roman in-line serviceable valve from Pompeii [4].	1
Figure 2: Modern severe-service metal-seated ball valve.....	2
Figure 3: Typical damage to the sealing surfaces of a MSBV after service.	3
Figure 2-1: Wear mechanism of Stellite under highly loaded sliding contact: a) the typical dendrite structure is visible in the bulk material along with the heavily deformed top layer; b) the thin top layer is transformed under high load from fcc phase to hcp phase; c) fragmented carbides are visible in the top layer; and d) transmission electron microscopy of the top layer, showing the thin top layer composed of hcp phase oriented parallel to the sliding interface [19].	15
Figure 2-2: Summary of threshold galling stress values for various Fe-based and Ni-based hardfacing alloys and the Co-based hardfacing alloy Stellite 6. Except for the Nucalloy 453/Nucalloy 488 couples, all hardfacings were tested in the self-mated condition [40].	20
Figure 2-3: Typical burnishing effects with varying force using a 22 mm roller on steel of 220 HV hardness (0.20% C; 0.30% Si; 0.80% Mg; 0.05% P; 0.05% S) [89].	29
Figure 2-4: Hardness as a function of temperature obtained by diffusion coatings made with different compounds [70].	31
Figure 2-5: Schematic illustration of plasma transfer arc welding [104].	33
Figure 2-6: Schematic illustration of laser welding [104].	33
Figure 2-7: Energy density required for various welding methods [103].	34
Figure 2-8: Typical surface finish after hard chromium electroplating [70].	35
Figure 2-9: Thermal sprayed coating deposition with typical lamellar microstructure [110].	37
Figure 2-10: Cross section of a basic flame spray gun [104].	38
Figure 2-11: Cross section of a High-Velocity Oxy-Fuel gun [104].	39
Figure 2-12: Cross section of an arc wire gun [104].	39
Figure 2-13: Cross section of a plasma spray gun [104].	40
Figure 2-14: Cross section of a cold spray gun [104].	41
Figure 2-15: Particle velocity and gas temperature for various thermal spray processes [110]. ...	42
Figure 2-16: Wear rate of several TS coatings compared to HC coatings during the Taber Abraser test – ASTM F1978 [117].	44
Figure 2-17: Cross section of agglomerated and sintered cermet powder prior to deposition.	44
Figure 2-18: A typical physical vapor deposition system [123].	45

Figure 2-19: Schematic representation of a typical chemical vapor deposition system [123].	46
Figure 2-20: nanocrystalline-TiN/aSiN nanocomposite formation and mechanical properties [128]......	47
Figure 2-21: Stress-strain curve for a ductile material [142]......	50
Figure 2-22: Categories of hard materials with characteristic crystal structures [144].	51
Figure 2-23: Stress–strain curve for brittle material in tension and in compression [142].....	53
Figure 2-24: Schematic representation of fracture toughness as a function of yield stress [155].	54
Figure 2-25: Schematic illustration of various limiting factors that determine the load-carrying capacity of a coated surface. Limiting factors: (a) coating fracture, (b) spallation, (c) substrate elastic deformation, (d) substrate plastic deformation, (e) substrate fracture, and (f) plowing friction [159].	55
Figure 3-1: Typical load–displacement curve obtained by depth-sensing indentation.....	59
Figure 3-2: Custom-designed, automated variable temperature galling tester.	63
Figure 4-1: XRD patterns of (a) HC, (b) NCP, and (c) W/WC materials.....	73
Figure 4-2: a)SEM images of NCP and W/WC cross section, b) EDS spectra of NCP, W/WC and HC materials.	74
Figure 4-3: Nano-hardness and Young’s modulus (a), Micro-hardness, Scratch-hardness at 10 N, and indentation depth/coating thickness as a function of load (b) for different coating types.	75
Figure 4-4: Scratch track at a 10N load for (a) HC, (b) NCP, (c) W/WC coatings.	76
Figure 4-5: Wear rate and friction coefficient for different counterparts and different coating types.	76
Figure 4-6: Micrographs of the wear track on a) HC with Al ₂ O ₃ ball – 5kx, b) HC with Co # 6 ball – 500x, c) NCP with Al ₂ O ₃ ball – 5kx, and d) W/WC with Al ₂ O ₃ ball – 10kx.....	77
Figure 4-7: Potentiodynamic polarization curves of HC, NCP, W/WC and bare SS316 materials.	79
Figure 4-8: SEM images of (a) NCP and (b) W/WC coatings after corrosion testing.	80
Figure 4-9: Images of valve components after the steam cycle test: (a) HC after 3,000 cycles, (b) NCP after 10,000 cycles, (c) W/WC coatings after 10,000 cycles.	81
Figure 4-10: Steam cycle test results: Valve torque as a function of the number of cycles for HC coating.....	81

Figure 5-1: HVOF 80/20 Cr_3C_2 -NiCr coating exhibiting cohesive failure after 1 year in service.	85
Figure 5-2: HVOF 80/20 Cr_3C_2 -NiCr coating, sprayed with C_3H_6 after 1 year in the field.	90
Figure 5-3: HVOF 80/20 Cr_3C_2 -NiCr coating, sprayed with C_3H_6 after 1 year in the field.	91
Figure 5-4: HVOF 80/20 Cr_3C_2 -NiCr coating, sprayed with C_3H_6 , after 30 thermal shocks going from ambient temperatures to 675°C .	92
Figure 5-5: XRD spectrums of HVOF 80/20 Cr_3C_2 -NiCr powder and coating, sprayed with C_3H_6 . Cr_7C_3 and Cr_{23}C_6 phases, even though not shown on the graph, could also be present. Peaks overlapping has impeded their identification on all XRD spectrums presented in the paper.	93
Figure 5-6: Microstructure evolution during aging test at 704°C (1300°F) after (a) 4 hour exposure; (b) 120 hour exposure.	94
Figure 5-7: XRD spectrums of HVOF 80/20 Cr_3C_2 -NiCr powder, “as sprayed” and aged coatings, after 4 hour and 120 hour exposure to 704°C (1300°F) respectively.	95
Figure 5-8: Coating #1 and #3 were repeatedly subjected to thermal shocks going from ambient temperatures to 675°C . Then they were put through liquid penetrant tests to check for any cracking.	99
Figure 5-9: XRD spectrums of HVOF material #1 and #2; powder and “as sprayed” coating.	100
Figure 6-1: Schematic of sample configurations (a) 316 / W-WC, (b) 316 / Co-C / W-WC, (c) 718 / W-WC, and (d) 718 / Ni-W-Cr-B / W-WC.	106
Figure 6-2: Cross section views of the coating systems a) 316 / Co-Cr / W-WC, b) Co-Cr / W-WC high magnification, c) Co-Cr high magnification, and d) 718 / Ni-W-Cr-B / W-WC.	109
Figure 6-3: XRD spectra of the thin film and the two hardfacing materials.	110
Figure 6-4: a) EDS spectra of the thin film and the two hardfacing materials, b) line scan across a precipitated crystal in the Ni-W-Cr-B interlayer.	111
Figure 6-5: Adhesion using Rockwell C indentation according to CEN/TS/1071-8 standard for (a) 316 / W-WC, (b) 316 / Co-Cr / W-WC, (c) 718 / W-WC, and (d) 718 / Ni-W-Cr-B / W-WC coatings.	112
Figure 6-6: Cross section view of the microhardness measurements on 718 / Ni-W-Cr-B / W-WC.	113
Figure 6-7: Hardness with load for the different coating systems.	114
Figure 6-8: Wear rate (bars) and COF (dots) for each coating system.	115

Figure 6-9: Wear track profile for each coating system.	115
Figure 6-10: SEM images of wear tracks for (a) 316 / W-WC, (b) 316 / Co-Cr / W-WC, (c) 718 / W-WC, and (d) 718 / Ni-W-Cr-B / W-WC coatings.	116
Figure 6-11: OCP measurements for a) substrate and hardfacings, and b) the four coating systems.	118
Figure 6-12: EIS spectra for a) substrate and hardfacings, and b) the four coating systems.	119
Figure 6-13: Potentiodynamic polarization curves for a) substrate and hardfacings and b) the four coating systems.	120
Figure A-1: n-TiO ₂ powder characteristics: (a) SEM micrographs – A: anatase, R: rutile, (b) XRD pattern, and (c) particle size distribution – logarithmic scale.	153
Figure A-2: Custom-designed automated variable temperature galling tester.	157
Figure A-3: Coating microstructures: Cr ₂ O ₃ at (a) 150X and (b) 1000X. TiO ₂ -Cr ₂ O ₃ at (c) 150X and (d) 1000X. n-TiO ₂ at (e) 150X and (f) 1000X. n-TiO ₂ -Cr ₂ O ₃ at (g) 150X and (h) 1000X.	159
Figure A-4: EDS spectra of the Cr ₂ O ₃ , TiO ₂ -Cr ₂ O ₃ , n-TiO ₂ -Cr ₂ O ₃ and n-TiO ₂ -Cr ₂ O ₃ materials.	160
Figure A-5: Coefficient of friction vs. sliding distance for the different coatings.	162
Figure A-6: Wear rate for the different coatings.	162
Figure A-7: Wear tracks after pin-on-disc tests at 50X.	163
Figure A-8: Wear tracks for specimens after dry abrasion testing.	164
Figure A-9: Wear tracks for specimens after wet abrasion testing.	164
Figure A-10: Galling resistance of self-mated specimens after variable temperature galling resistance. Mass loss is given between 0 (initial mass) and 100 cycles (i.e., after Step 2).	165
Figure A-11: Wear patterns of specimens after variable temperature galling test.	166

LIST OF ACRONYM AND SYMBOLS

Acronyms

AISI	American Iron and Steel Institute
ASTM	American Society for Testing and Material
APS	Air plasma spray
BHN	Brinell hardness number
BRC	Break torque to close
BTO	Break torque to open
CEA	Comité à l'Énergie Atomique
CTE	Coefficient thermal expansion
CVD	Chemical vapor deposition
DC	Direct current
DLC	Diamond like carbon
DPH	Diamond pyramid hardness
DSI	Depth-sensing indentation
EDS	Energy dispersive spectroscopy
EIS	Electrochemical impedance spectroscopy
EOLVD	End of life vehicles directive
EPA	Environmental protection agency
EPR	European pressurized reactor
EPRI	Electric Power Research Institute
ETC	End torque to close
ETO	End torque to open

FCP	Free corrosion potential
FCSEL	Functional Coating and Surface Engineering Laboratory
FEM	Finite element modeling
HAZ	Heat affected zone
HC	Hard chromium
HPAL	High pressure acid leaching
HRC	Rockwell hardness number
HRSG	Heat recovery steam generator
HRV	Vickers hardness number
HVOF	High velocity oxy-fuel
IBAD	ion beam assisted deposition
ISO	International organization for standard
MIG	Metal inert gas
MSBV	Metal-seated ball valve
NCP	Nanostructured cobalt-phosphor
NRC	National research council of canada
NSERC	Natural sciences and engineering research council
OCP	Open circuit potential
OEM	Original Equipment Manufacturers
PECVD	Plasma enhanced chemical vapor deposition
POx	Pressure oxydation
PTA	Plasma transfer arc
PTFE	Polytetrafluoroethylene
PVD	Physical vapor deposition
PWR	Pressurized water reactor

ROHS	Restriction of hazardous substances
RTC	Run torque to close
RTO	Run torque to open
S&F	Spray and fuse
SCE	Standard electrode
SEM	Scanning electron microscope
SMWA	Shielded metal arc welding
TIG	Tungsten inert gas
TS	Thermal spray
UASC	Ultra advanced super critical
WWII	World war II
XRD	X-ray diffraction

Symbols

3D	Three-dimensional
D _g	Grain size
E	Young modulus
E _b	Breakdown potential
E _c	Young modulus of the coating
E _{corr}	Corrosion potential
E _r	Reduced young modulus
E _s	Young modulus of the substrate
F	Applied load
H	Hardness

H/E	Elastic strain to failure
H^3/E^3	Yield pressure
H_N	Nano-hardness
H_M	Micro-hardness
H_S	Scratch hardness
H_v	Vickers hardness
I_c	Crystallinity index
I_o	Corrosion current density
k	Hall-Petch material constant
K	Wear Rate
K_{Ic}	Fracture toughness
N	Normal load
S	Sliding distance
SCE	Standard calomel electrode
V	Worn volume
W	Scratch width

Greek Symbol

Δm	Mass loss
λ	Wave Length
ϵ	Strain
ρ	Density
σ	Stress
σ_y	Yield strength

ν	Poisson Ratio
μ	Shear modulus

LIST OF APPENDICES

APPENDIX A NANOSTRUCTURED AND CONVENTIONAL Cr ₂ O ₃ , TiO ₂ AND TiO ₂ -Cr ₂ O ₃ THERMAL SPRAYED COATINGS FOR METAL-SEATED BALL VALVE APPLICATIONS IN HYDROMETALLURGY	150
A.1. Introduction	150
A.2. Experimental.....	152
A.2.1. Materials	152
A.2.1.1. Base Material.....	152
A.2.1.2. Powder Materials.....	152
A.2.2. Deposition Techniques.....	154
A.2.3. Characterization techniques	155
A.2.3.1. Microstructure	155
A.2.3.2. Mechanical Property Characterization	155
A.2.3.3. Tribological Behavior Assessment.....	156
A.3. Results and discussion	158
A.3.1. Microstructure.....	158
A.3.2. Microhardness.....	160
A.3.3. Adhesion	161
A.3.4. Tribomechanical properties	161
A.3.5. Sliding Wear Resistance	161
A.3.5.1. Dry Sand Abrasion	163
A.3.5.2. Wet Sand Abrasion.....	164
A.3.5.3. Variable Temperature Galling Resistance.....	165
A.4. Conclusions	167
A.5. Acknowledgements	168

APPENDIX B	TRIBOLOGY TERMS	170
B.1.	Abrasion.....	170
B.2.	Adhesion.....	170
B.3.	Coefficient of friction	170
B.4.	Debris.....	171
B.5.	Erosion.....	171
B.6.	Galling	171
B.7.	Load-carrying capacity	171
B.8.	Plastic deformation	171
B.9.	Sliding wear	172
B.10.	Spallation.....	172
B.11.	Wear.....	172

CHAPTER 1 INTRODUCTION

Many industrial sectors, including transport, power generation, manufacturing, aerospace, and automobiles, are seeking new functional coatings, engineered surfaces, and interfaces in order to meet increasingly demanding performance requirements. Specifically, improvements are sought in the tribological properties (i.e., wear and corrosion resistance) as well as characteristics such as long-term stability in hostile environments.

According to the National Association of Corrosion Engineers, the cost of corrosion in the USA in 2006 was 430 billion US\$, or 3.5% of the GDP. A more recent study by a private laboratory estimated the corrosion cost in the USA in 2013 at over \$1 trillion, or 6.1% of the GDP [1]. Similar studies have shown that wear imposes 90 billion US\$ in costs, or 0.75% of the GDP [2]. The seminal 1966 Jost Report, which generated a significant impact worldwide, estimated that up to 4% of the GDP could be saved in the UK by eliminating friction-related losses [3].

In this context, the valve industry is seeking new technologies that could provide high-quality coatings combining well-controlled tribological and corrosion performance with high mechanical integrity and environmental stability.



Figure 1: Ancient Roman in-line serviceable valve from Pompeii [4].

Pipes and valves are pressure vessels that regulate flow of materials, including liquids, gases, and slurries, by controlling the passageways. Pressure vessels have been used for thousands of years for various applications. Ancient depictions of piping systems show how they improved the quality of daily living. Based on remnants discovered by archeologists, we suspect that farming

villages were first established from 6,000 to 7,000 years ago during what historians refer to as the Neolithic Age.

It was during this time that the first successful systems to control water-irrigated agricultural fields were designed in Mesopotamia and Egypt, with the Sadd-el-Kafara dam in Egypt considered the world's oldest large-scale dam [5]. Neolithic piping systems were intended mainly to prevent flooding, and were built of stone and terracotta. During the Bronze Age, Greeks and Romans developed sophisticated systems to supply water to urban centers around the Mediterranean, including dams, aqueducts, and reservoirs. They also developed an extensive canal transport system. Moreover, they initiated the design and manufacture of standard valves made of a copper alloy very similar to ASTM B67, illustrated in Figure 1.

Today, although valves are still used for water regulation and farming, the industrial revolution has considerably extended the scope of application. Valves are used to control steam machines and power plants that deliver electricity to cities and industries. Valves are also used to control the flow of natural resources such as oil, gas, and mining products during extraction, transportation, and processing, whereby these crude minerals are transformed into refined products.

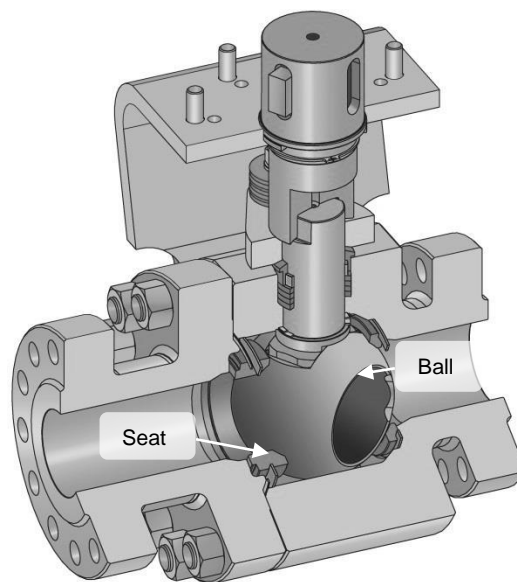


Figure 2: Modern severe-service metal-seated ball valve.

To be competitive and to meet an enormous range of requirements, these processes are continuously optimized to target maximum production rates at lower cost and maintenance.

Optimizing processes typically involve the use of higher pressure and temperature and/or more aggressive chemicals that cannot be handled using off-the-shelf valves. These are usually referred to as severe-service conditions, which require tailored materials and valve designs. Whereas almost any valve type can be optimized for severe-service, metal-seated ball valves (MSBVs) are usually the preferred choice. As illustrated in Figure 2, the sphere of a MSBV is located within the valve body, where it opens and closes by rotating 90 degrees. In open position, the tunnel bore across the ball is aligned with the piping so that the flow is unobstructed, whereas in closed position the tunnel bore is perpendicular to the piping, blocking the flow. Two surfaces, called the *sealing surfaces*, provide the seal in closed position: one is the outside surface of the ball and the other is the spherical radius of the seats, which are located in the body and guide the ball. MSBV sealing surfaces are inherently protected from particles present in the flow in both open and closed position, ensuring a reliable shut-off. MSBVs are relatively easy to operate in a slurry application, because the ball rotates on itself without displacing solids present in the line while tolerating the use of very powerful drive systems. This ensures rapid closure in critical situations.



Figure 3: Typical damage to the sealing surfaces of a MSBV after service.

Severe-service MSBVs are therefore exposed to high pressure, high temperature, and/or highly corrosive environments. These grueling operating conditions are exacerbated by solids present in the flow that are wedged between the sealing surfaces. Sealing surface degradation is a major cause of severe-service valve failure, and can result in two different failure modes. The first occurs when the valve fails to cycle on demand due to excessive friction between the sealing

surfaces. The second occurs when the valve performs a cycle on demand but fails to seal in closed position due to imperfections in the sealing surfaces. Both failure modes can be caused by degradation of the sealing surfaces resulting from one of the wear mechanisms, including plastic deformation, abrasion, erosion, galling [6], and spallation combined with corrosion. As reported by several authors who performed failure analysis on severe-service MSBVs, and as illustrated in Figure 3, surface degradation is frequently caused by a combination of wear mechanisms that may or may not act in synergy [7-9]. Nevertheless, to prevent premature failure and mitigate wear, original equipment manufacturers (OEMs) use various types of surface treatments and invest heavily in R&D on surface engineering.

In response to the needs of valve manufactures, this research focuses on the development and characterization of a new generation of protective coating systems designed to extend valve life, whereby the microstructural features of films are controlled to achieve an optimal combination of surface and substrate properties that meet specific application requirements, with significant economic impact.

Background

After completing my Master's degree in mechanical engineering in 2003, I arrived in Canada from France with a one-year visa and was soon hired as an R&D technician at the Velan Granby laboratory. My main duties were to help perform prototype tests on industrial valves exposed to pressures and temperatures ranging from cryogenic to 650 °C. With my academic qualifications, I was pretty comfortable running R&D test set-ups, operating the old steam boiler, installing strain gauges, and using data acquisition systems. However, I was not prepared to properly inspect worn surfaces, draw conclusions, or select surface treatments.

Finding myself isolated in the countryside, I began to self-study wear, friction, and surface treatments. This interest was exacerbated by the Quebec climate with its unique challenges, namely the corrosion, temperature transients, and icing conditions (i.e., the extremely long and harsh winter). In 2005, after obtaining OIQ membership, I was placed in charge of the Velan Granby laboratory, where I developed a collaboration between Velan and the Functional Coating and Surface Engineering Laboratory (FCSEL) at Polytechnique Montréal. At first, we characterized worn surfaces and helped perform failure analyses on returned products. A year later, when Velan decided to merge the Granby laboratory with a new, larger entity located in Montreal, I moved back to the metropolis and returned to Polytechnique Montréal to follow evening classes on materials science and friction. In 2008, the three engineers who were developing the Velan severe-service MSBV line left the company almost simultaneously. Velan asked me to step in as manager of this line, which combines exotic materials with sophisticated surface treatments. The mandate was not only to oversee the engineering, but also to develop Velan's coating know-how. I accepted both challenges and ended up with a considerable backlog, including boxes full of calculations, several products that had problems in the field, and no one to answer my questions.

It was at this time when I intensified Velan's collaboration with FCSEL, working primarily with Professor Jolanta Ewa Klemberg-Sapieha to characterize worn surfaces, but also to assess and compare the tribological and mechanical behavior of various surface treatments used by Velan. The outcome of this relationship was the creation of a coating matrix designed to compare the

tribo-mechanical properties of different coatings applied to valves. Hardness (H), Young's Modulus (E), and toughness were measured using microhardness indentation testers, and wear resistance under different conditions such as sliding wear and abrasion were measured by pin-on-disc and abrasion tests. In parallel, I helped prepare an application for a grant to enable us to acquire a novel high load tribometer to perform galling testing. This equipment is currently being purchased and will be used to complete our coating matrix.

With all those collaborations and my personal involvement as an external candidate, it was only natural that in 2009, when Professors Jolanta-Ewa Klemberg-Sapieha and Ludvik Martinu invited me to start a Ph.D. program within their group, I accepted their offer without hesitation. This was a way for me to not only strengthen the relationship between Velan and FCSEL, but more importantly, to develop new technologies.

Objectives

I have devoted the majority of my professional life to designing and manufacturing better valves. The objectives of this thesis are motivated by this long-term commitment, and by tangible opportunities that I believe are instrumental for advancing valve technology through a better understating of the fundamental physico-chemical mechanisms that govern surface degradation. Once the surface degradation mechanisms are fully understood (i.e., at the atomic level), a more suitable surface treatment can then be selected to inhibit specific wear mechanisms and ultimately extend valve life. Consequently, the fundamental chemical, metallurgical, mechanical, and physical concepts that govern surface degradation mechanisms must be accurately determined, and a variety of surface treatments can then be developed or improved.

- The first objective arose from the fact that the U.S. Environmental Protection Agency (EPA) has classified hard chromium electroplating as an environmentally unfriendly process. In accordance with Porter's hypothesis that environmental regulations should trigger the discovery and introduction of not only cleaner but also more efficient technologies, thereby improving a company's commercial competitiveness, nanostructured coatings appeared to be viable alternatives from both an engineering and a commercial perspective. Therefore, the objective of the study was to select the best

candidates for alternatives to hard chromium electroplating. To do so, several factors were considered, including the mechanical and tribological performance of recently developed coating technologies, potential supply chains, and long-term economic viability. In order to further mitigate the risks associated with the use of alternative treatments, the wear mechanism of hard chromium plating slid against Stellite 6 was examined to comprehend the tribological behavior behind the superior galling resistance of this material couple, and to compare it with the mechanisms for potential alternative coating materials when slid against Stellite 6. The ultimate goal was to select surface treatments that provide the equivalent mechanism to that for hard chromium.

- The second objective was to determine the cause of the recurrent failures occurring in the field with thermal sprayed HVOF $\text{Cr}_3\text{C}_2\text{-NiCr}$ coating applied to Inconel 718 PH when exposed to supercritical steam lines and thermal shocks in modern power plants. HVOF 80/20 $\text{Cr}_3\text{C}_2\text{-NiCr}$ coating has been used to protect thousands of MSBVs over the years, without incident. However, modern power plants expose valves to the added challenge of rapid high pressure and temperature variations, resulting in a severe-service situation where coatings undergo cracking and cohesive failure. The purpose of this study was therefore to fully understand the degradation mechanism causing the coating failures and to evaluate potential coating alternatives to reduce the effects and improve the reliability.
- The third objective was to study the effects of the mechanical properties of a material carrying a thin surface treatment on the tribo-mechanical and corrosion performance of the coating system. This objective was driven by thin film failures reported by end-users, attributed to high stresses at the interface and within the substrate material when subjected to highly concentrated load, leading to high stress levels that eventually cause permanent surface indentation, crack formation, and/or spallation. These failure modes are called brinelling (indentation due to substrate plastic deformation) and eggshell-effect (coating fracture and/or coating spallation). The purpose of this study was to design and produce innovative graded coating systems consisting of 1) a thin surface treatment with high hardness (H) and excellent sliding wear properties, and with superior mechanical behavior to that of conventional base materials used in the valve industry; and 2) a

hardfaced interlayer with a strain-to-failure characteristic between that of the substrate and surface material in order to reduce the mechanical properties gradient and therefore reduce the risk of premature failure due to inadequate load carrying capacity.

Thesis outline

This thesis is divided into seven chapters, beginning with the introduction.

Chapter 2 presents a literature review of the key elements required to fully understand this project. Chapter 3 presents the methods used for coating characterization. The three articles resulting from this work report the main results, and are presented in chapters 4 to 6.

Specifically, Chapter 4 presents a comparative analysis of two nanostructured coatings as alternatives to hard chromium: electrodeposited nanostructured cobalt-phosphor and chemical-vapor-deposited tungsten/tungsten carbide. The wear mechanisms that occur when hard chromium plating is slid against Stellite 6 under high load were investigated. After examining these interactions at the crystal structure level and determining those that are responsible for the exceptional tribological behavior of this material couple, the authors recommended an alternative material to hard chromium that provides a similar wear mechanism when slid against Stellite 6.

Chapter 5 presents a case study stemming from an investigation of a thermal sprayed HVOF $\text{Cr}_3\text{C}_2\text{-NiCr}$ coating failure for an on-off metal-seated ball valve (MSBV) used in supercritical steam lines in a power plant. HVOF 80/20 $\text{Cr}_3\text{C}_2\text{-NiCr}$ coating has been used to protect thousands of MSBVs, without incident. However, in this case the valves were exposed to the additional challenge of rapid high pressure and temperature variations, resulting in a severe-service situation where the coating underwent cracking and cohesive failure. After an in-depth failure analysis, the authors determined the mechanism that led to the failure and subsequently evaluated potential coating alternatives.

Chapter 6 examines the combination of hardfaced superalloy and thin film to produce superior mechanical performance to that of each individual layer. A critical issue in the deposition of hard

coatings onto softer substrates is the mismatch between thermal expansion and the elasto-plastic and structural characteristics. This causes high compressive mechanical stress, and hence weak adhesion [10]. There is increasing evidence that the optimum solution to erosive, corrosive, and adhesive wear problems lies in the design and manufacture of multilayered, graded, and/or nanostructured coatings and coating systems that combine controlled hardness and elastic modulus, high toughness, and good adhesion [11]. The aim of this study was to characterize two coating systems composed of 1) a hard thin film top layer, which provides superior tribological properties, and 2) a hardfaced interlayer, which increases the surface load-carrying capacity by reducing the elasto-plastic gradient and peak stresses. The first coating system consists of a tungsten–tungsten carbide thin film (W-WC) deposited by chemical vapor deposition onto a laser clad Co-Cr hardfaced interlayer (Stellite® 6) applied to a 316 stainless steel substrate, and the second consists of the same W-WC top layer and a high velocity oxygen fuel sprayed and fused Ni-W-Cr-B hardfaced interlayer (Colmonoy® 88) applied to an Inconel® 718 substrate.

Chapter 8 summarizes the contributions of this thesis and recommends avenues for future research.

Appendix A presents a detailed characterization project in which promising ceramic coatings were assessed for mechanical and tribological resistance. The goal was to better understand and harness the performance of the most promising ceramic coatings for hydrometallurgy processes, including pressure oxidation (POx) and high-pressure acid leaching (HPAL). Included was a novel $n\text{-TiO}_2\text{-Cr}_2\text{O}_3$ blend as a candidate for hydrometallurgy application, where air plasma sprayed ceramic coatings are vital to protect machines in the harsh abrasive conditions of corrosive POx and HPAL processes. Hardness, Young's modulus, adhesion, shear strength, and toughness were assessed using microhardness indentation testers and universal tensile testing equipment. Wear resistance of the coatings under various conditions such as sliding wear and abrasion were measured by standard pin-on-disc and abrasion tests.

My research work as presented in this thesis has resulted in numerous publications, as follows:

Table 1: Peer-reviewed publications

L.Vernhes, M. Azzi, E. Bousser and J.E. Klemberg-Sapieha, “Hybrid Co-Cr / W-WC and Ni-W-Cr-B / W-WC Coating Systems Hardfacing Superalloy as Interlayer for Thin Film”, submitted to Journal of Thermal Spray Technology, 2014.

L.Vernhes, D.A. Lee, D. Poirier, D. Li and J.E. Klemberg-Sapieha, “HVOF Coating Case Study for Power Plant Process Control Ball Valve Application”. Journal of Thermal Spray Technology, 2013.

L. Vernhes, M. Azzi and J.E. Klemberg-Sapieha, “Alternatives for hard chromium plating: Nanostructured coatings for severe-service valves”. Materials Chemistry and Physics, 2013.

Table 2: Peer-reviewed publications written in collaboration

M. Azzi, **L.Vernhes**, E. Bousser and J.E. Klemberg-Sapieha, “Mechanical, Tribological and Corrosion Properties of Co-Cr and NiWCrB Hardfacing Superalloy Coating Systems”. ASME 2014 International Mechanical Engineering Congress and Exposition, 2014.

Table 3: Working paper

L.Vernhes, C. Bekins, N. Lourdel, D. Poirier, R.S. Lima, D. Li and J.E. Klemberg-Sapieha, “Nanostructured and Conventional Cr₂O₃, TiO₂ And TiO₂-Cr₂O₃ Thermal Sprayed Coatings for Metal-seated Ball Valve Applications in Hydrometallurgy”.

Table 4: Conference proceedings and poster presentations

L.Vernhes, C. Bekins, N. Lourdel, D. Poirier, R.S. Lima, D. Li and J.E. Klemberg-Sapieha, “Nanostructured and Conventional Cr₂O₃, TiO₂ and TiO₂-Cr₂O₃ Thermal Sprayed Coatings for Metal-seated Ball Valve Applications in Hydrometallurgy”. International Thermal Spray Conference, Barcelona, Spain, 2014.

L.Vernhes, C. Bekins, N. Lourdel, D. Poirier, R.S. Lima, D. Li and J.E. Klemberg-Sapieha, “Nanostructured and Conventional Cr₂O₃, TiO₂ and TiO₂-Cr₂O₃ Thermal Sprayed Coatings for Metal-seated Ball Valve Applications in Hydrometallurgy”. Alta, Perth, Australia, 2013.

L.Vernhes, D.A. Lee, D. Poirier, D. Li and J.E. Klemberg-Sapieha, “HVOF Coating Case Study for Power Plant Process Control Ball Valve Application”. Reliability, Durability and Performance Assessment of Thermal Spray Coatings Conference, Albany, New York, USA, 2013.

L.Vernhes, D.A. Lee, D. Poirier, D. Li and J.E. Klemberg-Sapieha, “HVOF Coating Case Study for Power Plant Process Control Ball Valve Application”. Valve World, Dusseldorf, Germany, 2012.

L.Vernhes, D.A. Lee, D. Poirier, D. Li and J.E. Klemberg-Sapieha, “HVOF Coating Case Study for Power Plant Process Control Ball Valve Application”. International Thermal Spray Conference, Houston, USA, 2011.

L.Vernhes, D.A. Lee, D. Poirier, D. Li and J.E. Klemberg-Sapieha, “HVOF Coating Case Study for Power Plant Process Control Ball Valve Application”. Saudi Aramco Global Reliability and Safety conference, Houston, USA, 2011.

L. Vernhes, M. Azzi and J.E. Klemberg-Sapieha, “Alternatives for hard chromium plating: Nanostructured coatings for severe-service valves”. Society of Vacuum Coaters Conference, poster, FCSE, Montréal, QC Canada, 2011

L. Vernhes, M. Azzi and J.E. Klemberg-Sapieha, “Alternatives for hard chromium plating: Nanostructured coatings for severe-service valves”. Society of Vacuum Coaters Conference, Albuquerque, USA, 2010.

Table 5: Patents

Seat arrangement with cavity pressure relief for a ball valve, US Patent No. 8,002,237, 2010.

A ball valve resilient seat arrangement is provided that permits relief of cavity pressure. When the cavity pressure reaches a certain level, a sealing point between the seat and the valve body is lost. Communication is thereby provided between the space and the valve passage to achieve cavity pressure relief.

Spring energized resilient Seat for a ball valve, US Patent No. 8,500,090, 2013.

A ball valve resilient sealing ring is provided for sealing between a ball valve member and a valve body. The sealing ring may comprise a ring body having a ball valve member-contacting surface and one or more valve body-contacting shoulders for contacting the valve seat. The resilient sealing ring may comprise an elastic ring core for providing bending resistance.

Table 6: Memberships

Ordre des Ingénieurs du Québec

American Society for Testing and Materials, Committee officer, Subcommittee G02

International Organization for Standardization, P-member, Subcommittee SMC/ISO/TC153/SC1

American Society of Materials

CHAPTER 2 LITERATURE REVIEW

The literature review is divided into three sections to address the three components of this doctoral thesis. The first section provides a historical and state-of-the-art review on materials and surface engineering methods used in the valve industry, along with their limitations; the second summarizes surface engineering methods used to improve tribological behavior; and the third reviews the relationships between material properties and tribological behavior. A glossary of tribological terms is provided in the Appendix, including wear mechanisms and the underlying tribological processes.

2.1. Surface engineering methods applied to valves

2.1.1. Historical development

As mentioned in the introduction, valves were invented thousands of years ago to supply water to farms and cities. These antique valves were made of bronze alloys. Bulk bronze provides good corrosion resistance and acceptable tribological performance, and bronze continues to be used today for similar applications. The first significant technological challenge that triggered the introduction of new materials for valves occurred in 1705, when Thomas Newcomen invented the first steam engine able to convert steam power into mechanical work using the Rankine thermodynamic cycle. Although valves that were originally designed for water piping systems were first used for steam engines, the advent of the railroad facilitated access to cast iron, and valve manufacturers adopted this strong material to manufacture steam valves [12]. The first patent for a valve in the U.S. was filed by James Robertson in 1840. At that time, some of the legendary valve companies were founded, including Crane and Powell, which are still in operation today. In the 1860s, the Chapman Valve Manufacturing Company patented the now classical wedge gate valve.

Steam engine designs were optimized over the years, gradually replacing horses to power industrial equipment such as water pumps and locomotives. Efforts to improve the efficiency of the Rankine cycle by raising steam temperature and pressure began during the industrial revolution (approximately 1760–1840). In the 19th century, iron valves with bronze sliding surfaces were introduced. Higher-strength cast irons were also developed toward the end of the

19th century to support increasing temperature and pressure requirements at power plants where steam-powered turbines drove electrical generators. Engineering firms such as Boulton & Watt, founded by Matthew Boulton and James Watt in the UK in 1775, were pressing valve manufacturers to develop new valve materials capable of regulating steam flows at temperatures up to 260 °C and pressures up to 13.7 bars. Up to the beginning of the 20th century, valve sliding surfaces were made of bronze, and the first major innovation in materials was the invention of a copper–nickel alloy by David H. Brown in 1906. It was commercialized under the trade name Monel. Solid Monel provided greater hardness combined with better corrosion and wear resistance compared to bronze. It therefore replaced bronze for the protection of critical sliding areas of valves, thereby extending their in-service life [13].

The next new material to be adopted by the valve industry was martensitic stainless steel, patented in 1912 by Elwood Haynes, who discovered it while developing corrosion-resistant materials for horseless carriages. With its typical body-centered tetragonal microstructure obtained by heat treatment, martensitic stainless steel provides higher strength than Monel and good tribological performance. In addition, the 13% chrome content ensures satisfactory corrosion resistance, which made it the material of choice at that time for critical valve sliding areas [14]. Elwood Haynes subsequently patented a cobalt alloy commercialized under the trade name Stellite in 1913. Composed of **chrome carbides embedded in a cobalt-based matrix**, this alloy exhibits a low friction coefficient under highly loaded sliding contact, and it has **become the standard wear-resistant material in the valve industry** [15].

A low coefficient of friction, superior corrosion resistance, and high resistance to adhesion between the contact surfaces under high sliding load (called galling) are the three primary wear attributes of Stellite. These features prevent equipment seizure, surface deterioration, and gross material transfer between two counter bodies [16]. As reported by several authors, Stellite alloys exhibit a particular wear mechanism under high-load sliding wear: material transfer is restricted to a nanoscale thin superficial layer that is easily sheared, and which acts as a solid lubricant while preventing catastrophic galling and seizure [17]. This thin layer results from a phase transformation under high load: from face-centered cubic (fcc) to hexagonal close-packed (hcp), providing a preferred slip on the basal plane oriented parallel to the sliding interface. The

preferred slip plane provided by the low COF of hcp structures was theoretically demonstrated by Buckley and Johnson (1968), and the resulting lamellar structures are useful features of common solid lubricant materials such as graphite, molybdenum disulfide, and boron nitride [18]. Figure 2-1 shows Stellite under highly loaded sliding contact, revealing a thick fcc interlayer and an easily sheared hcp top layer that is regenerated when worn.

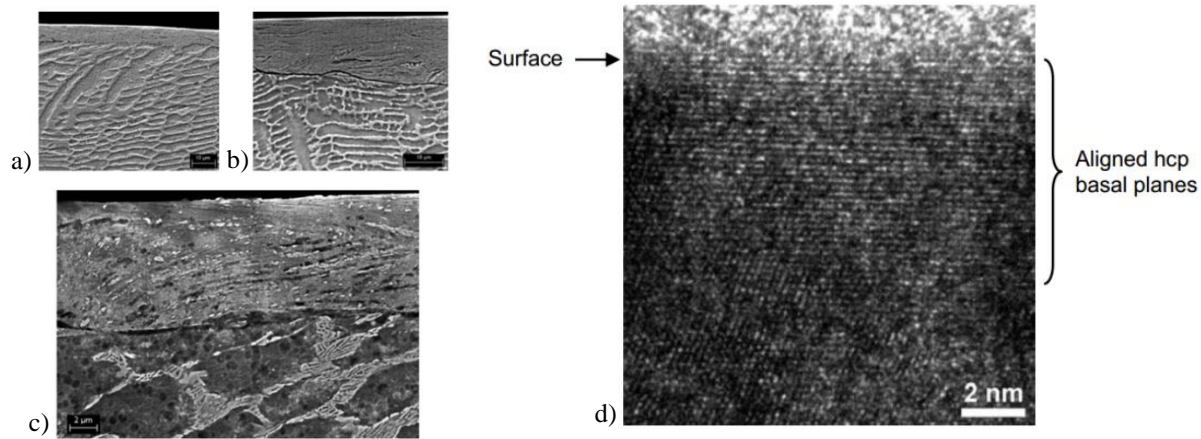


Figure 2-1: Wear mechanism of Stellite under highly loaded sliding contact: a) the typical dendrite structure is visible in the bulk material along with the heavily deformed top layer; b) the thin top layer is transformed under high load from fcc phase to hcp phase; c) fragmented carbides are visible in the top layer; and d) transmission electron microscopy of the top layer, showing the thin top layer composed of hcp phase oriented parallel to the sliding interface [19].

This easily sheared superficial layer eases the transfer to a non-stellite counter material, and therefore Stellite against Stellite sliding contact occurs, even when only one of the two counter bodies is originally constituted of Stellite, as discussed in Chapter 4 [19].

The invention of this adaptive material marked the beginning of a century of Stellite's quasi-monopoly in the valve industry, with grade 6 being the most widely used, disturbed only by the introduction of a novel non-metallic material called Teflon, which Dupont patented in 1938. During World War II, the US army, needing a fast-acting tight shutoff compact valve with better corrosion resistance than martensitic steel, developed the resilient-seated austenitic stainless steel ball valve. Based on the ball valve design patented in 1871 by John Warren and John Chapman, which required bronze sliding surfaces, the first mass-produced ball valves were built with the

now ubiquitous fluoropolymer material. These innovative ball valves played an instrumental role in high octane gasoline refining and the production of other valuable oil-based products required to support the war effort [20].

After the war, resilient-seated austenitic stainless steel ball valves were first commercialized by the Jamesbury Corporation, founded by Howard G. Freeman. They are still used extensively for corrosive chemical and petrochemical processes, where they have been made more abrasion-resistant, and where the range of application has been extended beyond the PTFE temperature limit [21]. Thus, valve manufacturers have developed austenitic stainless steel ball valves equipped with Stellite seat rings and hard chrome plated austenitic stainless steel balls that can operate at 700 °C while providing excellent corrosion resistance. New nickel-based superalloys such as Alloy 20, Hastelloy X (also developed by Haynes, the trade name being a combination of Haynes and Stellite), Monel K-500, Inconel 625, Nimonic, and Waspalloy were developed during the boom decades after the Second World War, extending both the operating temperature and corrosion resistance of valves and piping [22]. Electroless nickel plating combined with heat treatment was also introduced for application to austenitic stainless steel balls coated with hard chrome that were exposed to attack by weak acids solutions (e.g. nitric or hydrochloric acid). Occasionally, electroless nickel was applied between the austenitic stainless steel and hard chrome layers as a corrosion barrier to mitigate corrosion attack while retaining the superior wear resistance of hard chrome [22].

In parallel with the arrival of new chemicals, petrochemicals, and corrosion-resistant alloys, newly engineered chromium-rich steels helped raise the operating temperatures of steel valves, enabling engineering firms to improve power plant efficiency by operating above the vapor–liquid critical point. In the 1960s, the first supercritical power plant operating with steam at 600 °C and 290 bar was launched in Ohio, US [23]. Since the close of the 20th century, the severe-service metal-seated valve industry has moved away from traditional, relatively soft anti-galling Stellite to embrace hard thermal sprayed coating materials for the most demanding applications. The two main drivers for this change were 1) the severe corrosiveness of modern chemical processes, which require application-specific surface treatments, and 2) the need for more wear-

resistant surface treatments that resist erosion and abrasion caused by particles present in the flow while providing a longer life cycle [24].

2.1.2. State-of-the-art materials and challenges

Stellite, hard chrome plating, and Teflon remain the dominant wear-resistant materials in the valve industry. However, continuous advances in industrial processes have called for the development of new corrosion- and wear-resistant surface treatments that, despite their enhanced performance, have difficulty meeting ever-evolving industry needs. Optimized tribological solutions developed over the last decade have already reached their limit for certain extreme applications, and the evidence shows that a substantial number of surface treatment challenges remain to be overcome.

This chapter describes some of the new materials used in the valve industry over the past two decades as well as the most pressing challenges that remain, including those addressed in this doctoral research project.

2.1.2.1. Fossil power generation

In the last 20 years, combustible costs, environmental policies, and a growing demand for electric power have motivated engineering companies such as GE and Siemens to improve the efficiency of power plants [25]. Accordingly, coal-fired power generation technologies have evolved to operate with steam at higher temperatures and pressures in order to increase efficiency, as explained by the thermodynamic laws [12]. Today, most modern power plants operate at above the vapor–liquid critical point, producing more power output at higher thermal efficiency. These state-of-the-art power plants, called supercritical (SC) combined cycle power plants, work at 600 °C, use 9% chromium steel alloy valves with superior high temperature properties, and are equipped with heat recovery steam generators (HRSG) that recover waste heat from hot exhaust gas in order to power auxiliary turbines, hence converting over 45% of the fuel energy into electricity [26].

In addition to operating under extreme steam temperatures and pressures, the power plants are run during peak usage times. Consequently, SC power plants cycle several times per day in order

to adjust supply to demand, thereby minimizing fuel consumption. Each time a power plant is turned off and on, the piping undergoes intense thermal and pressure stresses, accelerating materials aging and shortening valve life, with the worst impacts on the highest temperature components [27]. Several cases have been reported in which the Stellite overlay failed prematurely, leading to shutdown. One typical failure mechanism is debris present in the flow that plows the Stellite overlay, hampering valve tightness. A second typical failure mechanism is delamination due to heat affected zone (HAZ) embrittlement combined with thermal stresses induced by differing expansion coefficients [28, 29]. Developmental initiatives are ongoing to either improve the performance of Stellite or to find alternative solutions to improve valve reliability. For example, a study by Bharat Heavy Electricals Limited (2000), the largest Indian power plant manufacturer, revealed the superior tribological behavior of an HVOF $\text{Cr}_3\text{C}_2\text{-NiCr}$ coating over Stellite during laboratory testing at high temperature, and reported the successful use of HVOF $\text{Cr}_3\text{C}_2\text{-NiCr}$ -coated valves for four years in one of its power plants [30]. In 2006, similar results were found in an experiment using the Advanced Test Reactor at the US Department of Energy's Idaho National Laboratory.

The original Stellite valves, which controlled high temperature steam circulating at 377 °C and 262 bars, required frequent maintenance to contain leakage. Since their replacement in 1998 by valves coated with HVOF $\text{Cr}_3\text{C}_2\text{-NiCr}$, failures have stopped and preventive maintenance is no longer required [31]. The low coefficient of friction and the mild wear regime for self-mated HVOF $\text{Cr}_3\text{C}_2\text{-NiCr}$ under the highly loaded sliding contact encountered in power generation are generally attributed to the formation of a strongly adherent oxide tribolayer containing Cr_2O_3 and NiCr_2O_4 as well as the presence of graphite on the sliding surfaces (graphitization, or graphite formation), which prevents adhesive wear. HVOF $\text{Cr}_3\text{C}_2\text{-NiCr}$ material loss during sliding is commonly attributed to carbide pull-out, matrix extrusion, and carbide fracturing [32]. However, HVOF $\text{Cr}_3\text{C}_2\text{-NiCr}$ coatings are not infallible in SC power plants; Chapter 5 describes an investigation of an HVOF $\text{Cr}_3\text{C}_2\text{-NiCr}$ coating failure by crack propagation in supercritical steam lines and presents a proposed solution. Low ductility and high hardness are generally mentioned as contraindications for SC power plant application. Accordingly, researchers have attempted to create tougher coating materials, such as the NASA-developed PS304 and PS400, which contain

a high-strength nickel–chrome matrix with solid lubricants such as Cr_2O_3 , silver, and $\text{BaF}_2/\text{CaF}_2$, designed to prevent adhesion at high temperatures and maintain a low COF up to 650 °C [33].

Even as surface treatments for SC power plants continue to be optimized, major engineering firms have already demonstrated the technical and commercial viability of Advanced Ultrasupercritical Power plants (A-USC) operating at up to 760 °C and 500 bar and equipped with Ni-based alloy piping, which will require new tailored surface treatments [34]. Companies such as Fuji Electric Systems are currently performing tribological tests at temperatures over 700 °C in a high pressure steam environment to select the best candidates, including Ni-based superalloy, Tribaloy, and Stellite [35].

2.1.2.2. Nuclear power generation

One of the most compelling challenges for society is to produce carbon-free electrical energy, and nuclear power plants are viewed as a highly promising solution. Nuclear power plants have a wide range of applications. Among others, they generate the steam that drives modern submarines, aircraft carriers, and other naval vessels, and they produce radioisotopes that are used to diagnose diseases. However, most of the valves currently in use in nuclear power plants were hardfaced with Stellite, which is problematic. Ocken determined in 1985 that the presence of cobalt in the primary circuit of pressurized water reactors (PWRs) is a major cause of high radioactivity of the primary circuit water, with the cobalt originating from the wear of the Stellite coating that protects the valve sliding surfaces [36]. Since then, cobalt has been identified as the main contributor to the radiation exposure of maintenance staff, via the formation of the isotope ^{60}Co [37]. This has prompted several nuclear institutes, including the Atomic Energy Commission (CEA), the Westinghouse Atomic Power Laboratory, and the Electric Power Research Institute (EPRI), to develop and test various cobalt-free alloys as replacement materials for Stellite, including Deloro 50 and Colmonoy 5 [38].

One positive outcome of these studies is an alloy called Norem 02. Norem is an iron-based wear-resistant alloy originally developed by EPRI. It has a higher threshold galling stress (TGS) than nickel-based superalloys, as indicated in Figure 2-2 (taken from the Westinghouse Atomic Power Laboratory, Laboratory galling tests of several commercial cobalt-free weld hardfacing alloys, 1997). Norem contains an iron-based austenitic matrix with carbides precipitated at the grain

boundaries. Norem is used in valves installed in several commercial nuclear power plants in the US and in the three first European pressurized reactors (EPRs) in Finland, France, and China, the most recent nuclear reactor design, produced by Areva. Unfortunately, laboratory assessments of Norem have reported higher friction coefficients and inferior sliding wear performance compared to Stellite, particularly at temperatures above 180 °C [39].

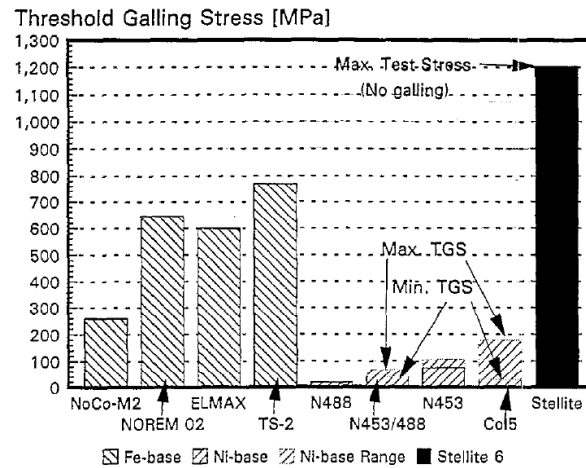


Figure 2-2: Summary of threshold galling stress values for various Fe-based and Ni-based hardfacing alloys and the Co-based hardfacing alloy Stellite 6. Except for the Nucalloy 453/Nucalloy 488 couples, all hardfacings were tested in the self-mated condition [40].

Table 2.1: Norem 02 nominal composition (mass %) and physical properties

Fe	Cr	Mn	Ni	Others	Hardness [HV]	Density [g/cm ³]	Melting Range [°C]
Base	23–26	4–5	3.7–5	Mo, Si, N, P, S, B	400–500	N/A	N/A

As seen in Figure 2-2, the Norem TGS properties are significantly lower than for Stellite at ambient temperature, and the adhesion susceptibility rises dramatically at over 180 °C, limiting its use to mild temperature applications. Because Norem is not fully interchangeable with Stellite, products designed for Stellite have to be reinforced to accommodate Norem's tribological properties, and they have a limited temperature range [39]. Consequently, considerable research efforts around the world are being directed to develop a better alternative to Stellite for PWR applications [41]. In a report by Sumitomo Energy, the total amount of cobalt

dilution in a multilayer $\text{Al}_2\text{O}_3/\text{TiN}/\text{TiC}$ coating applied by chemical vapor deposition onto Stellite is less than 1% of that for pure Stellite [42]. More recently, Sumitomo reported that a 7 μm thick CrN film applied by CVD onto Stellite reduced the cobalt dissolution rate into hot water by four orders of magnitude while improving sliding wear and galling resistance [43]. Hitachi has also developed a cobalt-based alloy with similar chemical composition to that of Stellite, but with a different microstructure that mitigates wear, reducing cobalt dissolution by a factor of ten [44].

Apart from cobalt dissolution, nuclear power generation poses other tribological challenges. One such challenge is the use of molten fluoride salts as coolant, due to their higher heat transfer capabilities compared to water. Because fluoride salts are extremely corrosive at high temperatures, they preclude the formation of protective oxides, and therefore require the use of nickel-based piping such as Hastelloy [45]. Manley (1958) previously determined that, due to this high corrosion and the absence of oxide formation, conventional hardfacing materials tend to bond in molten fluoride salts at temperatures above 1000 °F (537.78 °C). Following preliminary wear tests, the most promising materials appear to be ceramics and cermets, and particularly TiC-Ni and WC-Co [46]. Molten salts are also used in non-nuclear power plants, such as solar power plants, for heat transfer and storage, with similar tribological challenges [47].

2.1.2.3. Exploration and production – The upstream oil sector

One of the most frequently reported tribological challenges for valves used to control the ground to surface flow of crude oil and/or natural gas in sand laden regions is sand particle erosion. Extracting crude petroleum from underground deposits requires pressures up to 1000 bars, temperatures up to 200 °C, and a flow velocity that exceeds 500 m/s. The concentration of sand particles in the oil-field soil normally ranges from 10 to 100 ppm by weight and from 60 to 100 μm by size [48]. Valve operation becomes critical in such conditions, as underscored by the 2010 Deepwater Horizon oil spill (also called the BP oil spill) in the Gulf of Mexico. This environmental and financial disaster could have been mitigated if at least one of the blowout preventer valves had not failed to close. Why all these valves failed at the same time is still under investigation, but the dominant wear mechanism for this type of valve application has been well documented: the usual culprit is sand particles in the flow.

The API 6AV1 and ISO 10432 standards specify the requirements for critical valves operating in sandy service in order to reduce the risk of valve failure prior to installation. The significant financial impact of valve failure has driven research and innovation in the field of surface treatments. In 1997, BP estimated the replacement cost at £500,000 (about \$US 795,000) per damaged valve, with the annual cost of valve failure at around £30 million (\$US 47,567,000) for BP alone [49]. Wheeler and Wood (1998) found that because traditional valve-protective coating (including hard chrome plating) has lower hardness than sand, the erosion rate is five times higher than that for thermal sprayed WC-based coating [50]. Thermal sprayed WC-CoCr is therefore one of the most popular coatings for this type of service, particularly for high velocity applications. In addition to its superior erosion resistance, it forms a superficial tungsten trioxide tribolayer in oxidizing environments, providing good sliding wear properties and low COF while preventing adhesion. Tungsten trioxide, which has a lamellar structure similar to graphite, is considered a solid lubricant [51]. Because the tribolayer provides no protection against sand particles, the erosion mechanism for WC-CoCr, a two-phase anisotropic material, consists of minor cutting in the ductile CoCr matrix and cracking in the WC. However, most of the damage is caused by subcritical crack growth along the splats and parallel to the surface, followed by spallation [52].

Researchers are currently seeking better alternatives and identifying promising materials. For instance, Haugen et al. (1995) demonstrated the superior erosion resistance of solid tungsten carbide components and SiC ceramics, which are currently used for critical applications [53]. In the same study, borided Stellite with a hardness of 1500 HV obtained excellent performance for velocities below 50 m.s^{-1} , although premature failure occurred at 200 m.s^{-1} . Mann et al. (2006) investigated other thin surface treatments for oil and gas extraction applications, including a TiAlN PVD coating with erosion resistance roughly similar to that of WC-CoCr HVOF coating. However, this solution was discarded due to numerous pin hole defects in the coating that reduced the corrosion resistance and resulted in premature failure [54]. Wheeler et al. (2006) [55] found that a CVD-applied DLC coating on solid tungsten carbide components provided a 50 to 60% greater resistance to sand particle erosion damage.

2.1.2.4. Refining and petrochemical industries – The downstream oil sector

Once the oil is extracted, it is delivered to petroleum refineries where it is subjected to high temperature processes to produce useable fuel, and where further challenges await. Here, hard chromium plating is particularly valued for its wear-resistance and anti-sticking properties. It is highly useful for applications where oil residues build up and must be removed. Removal is facilitated by the natural disaffinity between chromium and carbon-based materials, generally attributed to the slow diffusion rate for chrome and carbon, which lowers the risk of adhesion problems. Fluid catalytic cracking (FCC) is a traditional high-temperature low-pressure refining process that was developed when Stellite and hard chromium plating were more commonly used to protect valves [56]. FCC uses a catalyst, a fine silica–alumina powder with a particle distribution ranging from 10 to 150 μm , to break long-chain hydrocarbon molecules at temperatures up to 740 $^{\circ}\text{C}$ [57]. To mitigate catalytic erosion at high temperatures, valve manufacturers have been replacing Stellite and hard chrome plating with boron diffusion into Stellite (Cooper et al., 1992). The result is case hardening: a 50 μm deep layer with a hardness exceeding 1500 Hv is formed at the surface while allowing the material underneath to remain soft, improving the abrasive wear resistance by approximately two orders of magnitude and erosion resistance by 50% [58].

Another alternative described by Shidu et al. (2007) is a thermal spray deposited $\text{Cr}_3\text{C}_2\text{-NiCr}$ coating that provides a more robust protection than WC-Co coating at the higher temperatures used for coal gasification, where hot corrosion resistance is required [59]. However, when a process fluid contains up to 25% of hydrogen sulfide and carbon dioxide, high temperature erosive refining processes can generate sulfide stress cracking (SCC) and hydrogen embrittlement. One solution investigated by Cataldo (2000) is boron diffusion into nickel to protect valves used for oil and gas valve applications in sour gas environments, where resistance to abrasion, erosion, and corrosion is required [60].

Another solution examined by Isakaev (2009) and adopted by the valve industry is the use of nickel-based self-fluxing hardfacing such as Colmonoy to prevent SCC in these environments [61]. In addition to superior SCC resistance, this type of hardfacing provides high hardness at high temperatures, improving resistance to the abrasive and erosive wear generated by the

catalyst [62]. Stott et al. (1973) showed that self-mated nickel-based superalloys also obtain good sliding wear behavior at high temperatures due to the formation of a wear protective glaze layer composed of compacted oxide particles that dramatically reduces the coefficient of friction and prevents adhesive wear [63]. Gurumoorthy et al. (2007) also observed that the formation of an oxide wear-protective glaze layer at 300 °C reduced the wear rate of a self-mated nickel alloy to less than 5% of the rate for the same alloy measured at room temperature during a sliding wear test under high load (50 N load applied to a 3 mm diameter tip) [64].

The coal-powered industries are facing similar challenges. In an attempt to produce cleaner, more efficient energy, they have developed new technologies such as the Integrated Gasification Combined Cycle (IGCC) and Pressurized Fluidized Bed Combustion (PFBC). These next-generation energy sources use a gasifier to convert coal into synthesis gas via the Fischer–Tropsch process. In these environments, valves control the flow of coal, fly ash, slag, and coke at pressures up to 300 bars, resulting in high velocities and intense slurry flow erosion. In addition, gasification temperatures above 900 °C preclude the use of self-fluxing nickel-based hardfacing: as explained above, the application temperature is too close to the alloy's melting point. Therefore, ceramic materials are required in areas operating at extremely high temperatures [17]. Lugschedier (1991) reported that Tribaloy T-800, consisting of a hard intermetallic Laves phase dispersed in a softer cobalt alloy matrix, is used in the valve industry for abrasive applications at over 600 °C. It exhibits almost constant hardness, at around 400 HV₃₀₀, from 400 °C to 800 °C, while the presence of stable adherent oxides minimizes friction and prevents adhesion, providing good sliding wear behavior [62]. At the low end of the temperature spectrum, Wang et al. (2011) demonstrated that a CVD-deposited DLC film onto the working surface of conventional WC-Co valve components extended the working lifetime to ~1200 hours, more than three times that of conventional tungsten carbide valve components in certain low temperature areas of the IGCC [65].

Petrochemical plants use a variety of chemical processes to transform refined petroleum products into detergents, adhesives, and polymers. The most severe-service petrochemical processes require the use of zirconium, Hastelloy, Inconel, or titanium vessels, with valve sliding surfaces protected by ceramic coating materials such as chrome oxide or titanium dioxide applied by

thermal spray and other processes [66, 67]. Hood (2010) observed that a zirconia layer formed by diffusing oxygen into zirconium effectively protects severe-service MSBVs that handle acetic acid, allowing the use of solid zirconium valves in acetic acid applications where they were previously considered inadequate [68]. Hood (2010) also successfully used a fluidized bed furnace to diffuse nitrogen into titanium, tantalum, and niobium, which are commonly used in the manufacture of valves for sulfuric and hydrologic service. Scrivani investigated thermal sprayed WC–CoCr carbide coatings and found high erosion resistance due to their high microhardness, which helps mitigate the wear of high pressure gas valves while preventing pollution and safety problems [69].

Although hard chrome plating is not the only solution, refineries and petrochemical plants continue to use it extensively, not only for its good wear and corrosion resistance, but also for its anti-sticking property, which facilitates oil-based product handling [70]. Finding a viable alternative poses a tough but unavoidable challenge for valve manufacturers. For instance, the US Environmental Protection Agency (EPA) has declared that short-term exposure to hexavalent chromium, the hexavalent oxidation state that is the most toxic form of chromium, may cause skin irritation, and long-term exposure can damage the liver, kidneys, circulatory system, and nervous system. Accordingly, hexavalent chromium has been classified as one of 17 high-priority toxic chemicals for voluntary reduction.

It has therefore become critical for the valve industry to find alternative coatings that provide similar performance to that of hard chrome plating, but without the risks. The European Union (EU) has largely prohibited the use of hexavalent chromium in electronic equipment under the Restriction of Hazardous Substances Directive (RoHS) as well as the End-of-Life Vehicle Directive (EOLVD), which was adopted to reduce the amount of hazardous waste coming from junk vehicles. Identified in the EOLVD as one of the hazardous materials used in vehicle manufacturing, hexavalent chromium has been banned in the industry by the EU nation states starting in July 2003 [71]. These restrictions have pushed the valve industry to seek cleaner alternatives, as evidenced by the number of publications devoted to this topic [72, 73]. To date, nanostructured coatings produced by vacuum-based techniques and Cr^{6+} -free plating have shown great promise as environmentally friendly, cost-effective alternatives to HC [74]. Chapter 3 of this thesis addresses this topic.

2.1.2.5. Mining

Mining is synonymous with erosion and abrasion. In mining, valves are instrumental for transporting slurry, which is mud composed of solids mixed with water. Conversely to oil and gas flow, the solids in the slurry flow are the desirable materials, whereas the liquid serves as the carrier. In mining, the ratio of solids to liquid can range from 10% up to 80%, compared to around 0.5% to 2% in oil and gas extraction. In a solids carrying pipeline, the transported material must be finely ground so it can be suspended in water to achieve a liquid-like flow pattern, with a particle size distribution that can span three orders of magnitude. In order to reduce friction and mitigate erosion, the flow velocity is typically maintained at 0.5 m/s above the flow velocity at which solids deposition occurs [75]. More efficient than trucks and trains, slurry pipelines can hurtle mountains, traverse countries, and cross borders to bring mining products to processing plants.

The first commercial slurry pipeline, the East Lake slurry line in Ohio, US, was engineered in 1957 by the Consolidation Coal Company. It was 250 mm in diameter and 170 km long, and could carry 1.3 million tons of coal per year from mines near Cadiz to coal-fired power stations in Cleveland. It was shut down when the railroad offered tariffs below the pipeline's rate. At that time, due to the limited availability of specific ore-handling equipment, oil extraction companies used equipment that was designed to handle solids entrained in the flow. Thus, ball valves designed for oil and gas transportation were transposed to the mining industry [76]. These sub-optimal contrivances, with their relatively soft wear-resistant surface treatments such as Stellite and hard chrome plating, incurred high maintenance costs and inconvenient shutdowns.

Hocke et al. (1978) examined the use of polyurethane, rubber, stainless steel, and ceramic materials and found that, compared to steel, they provided a six- to sixteen-fold increase in life in terms of slurry pipeline flow resistance [77]. Haugen et al. (1995), in a laboratory study mimicking field conditions, demonstrated that thermal sprayed WC-NiCr coating had markedly superior erosion resistance over Stellite [53]. Hawthorne (1999) showed that thermal sprayed coating with a chrome-free matrix was more prone to erosion-corrosion (i.e., impingement damage of the natural protective oxide layer, resulting in corrosion acceleration), and should be

avoided [78]. Other ceramic-based materials were investigated by Goyal et al. (2012), who found that thermal sprayed Cr_2O_3 , $\text{Cr}_3\text{C}_2\text{-NiCr}$ and WC-CoCr coatings enhanced slurry erosion resistance, which was attributed to their higher hardness compared to uncoated CA6NM steel [79-81]. More recently, nanostructured cermet powder has emerged as a promising candidate [82]. Harrison's (2009) review describes how valve technology has evolved: high pressure slurry pipelines are now equipped with severe-service ball valves that are optimized by finite element analysis (FEA) and protected by HVOF WC coating. These valves are designed to control flows through pipelines as wide as 750 mm in diameter and operating at pressures up to 280 bars to transport zinc, nickel, copper, iron, phosphate, and coal [83].

Slurry pipelines move mining products from mines to mineral processing plants. Hydrometallurgy, a mineral processing technology, is also a major user of severe-service valves. For these applications, protective coatings are selected according to vastly different criteria. The valves are usually manufactured with either titanium or duplex stainless steel substrates to ensure corrosion resistance, and are protected by a ceramic coating to enhance tribological performance. Conventional Cr_2O_3 applied by Air Plasma Spray (APS) was the coating of choice 20 years ago to protect severe-service valves against the extreme abrasion, pressure, and high temperatures inherent to the hydrometallurgy recovery process, where the ore is mixed with sulfuric acid in an autoclave. Hydrometallurgy has evolved since then: the most advanced recovery process involves leaching ore in a sulfuric acid–oxygen media in an autoclave at up to 4.1 bars and at temperatures above 240 °C. These conditions would corrode the previously used APS-deposited Cr_2O_3 coatings. Because it is relatively inert in this environment, TiO_2 appears to be a natural alternative to Cr_2O_3 [7]. However, the mechanical and tribological performance of conventional TiO_2 is significantly lower than that for Cr_2O_3 , resulting in higher wear rates. The industry has therefore been working on optimizing coating solutions for hydrometallurgy [84-86]. Appendix A of this thesis presents a detailed characterization study in which the mechanical and tribological resistance of the most promising ceramic coatings for hydrometallurgy applications are assessed, including a novel nanostructured n- $\text{TiO}_2\text{-Cr}_2\text{O}_3$ blend.

2.2. Surface engineering techniques

Surface treatments to improve tribological performance are frequently preferred to using bulk materials with the required properties. Surface treatments allow benefiting from highly optimized tribological properties only where needed, providing superior wear performance while avoiding the undesirable effects of strengthening processes (such as ductility loss) in other areas of the components. Surface engineering methods can generally be divided into two categories: surface modification and coating. Surface modification methods include some of the material strengthening mechanisms that are described in section 2.3.1, but applied to the surface only.

2.2.1. Surface modification

2.2.1.1. Peening

Surface mechanical and tribological properties can be modified by superficial plastic deformation. This shallow work hardening may involve blasting the surface with pellets, referred to as shot peening. Alternatively, a hard tool can be rolled over the surface, called knurling for a textured finish or burnishing for a smooth finish. The burnishing process causes the metal to flow plastically from surface peaks to valleys, thereby smoothing the surface finish. Both knurling and burnishing increase the surface strength of the material and induce compressive residual stresses that make the material more fatigue resistant. Shot peening and knurling produce rough surfaces, and are therefore used as an intermediate process prior to coating, whereas burnishing produces a mirror finish, and is usually performed as a final operation [87, 88]. Peening generates relatively low hardness, as shown in Figure 2-18, and is therefore used on non-sealing surfaces that are subjected to relatively low contact pressure. For example, driving shafts that slide against seals are burnished to mitigate wear and adhesion while reducing friction.

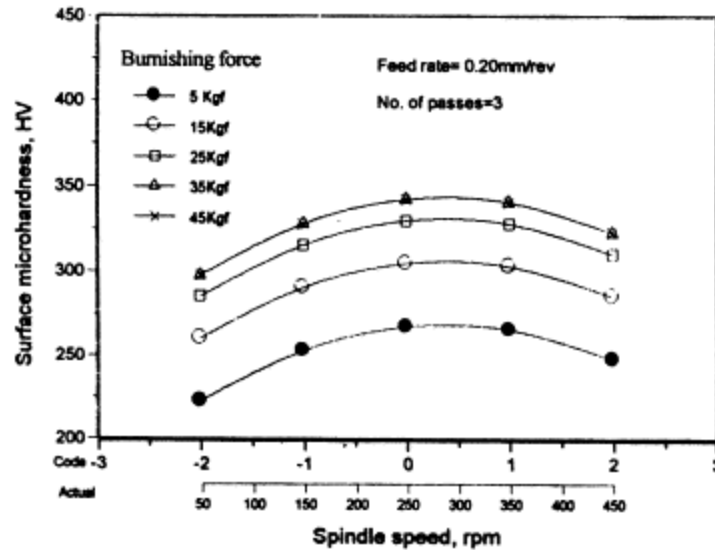


Figure 2-3: Typical burnishing effects with varying force using a 22 mm roller on steel of 220 HV hardness (0.20% C; 0.30% Si; 0.80% Mg; 0.05% P; 0.05% S) [89].

Peening is also used to condition sealing surfaces prior to other surface treatments in order to obtain the required surface roughness and to increase the strength of the substrate carrying the coating.

2.2.1.2. Superficial quenching

Superficial quenching involves a process in which the component is heated superficially using a flame, an induction system, or other local heating source to perform a shallow heat treatment, with induction hardening used extensively for steel and cast iron. The component is heated superficially to the austenitizing temperature and then cooled rapidly (quenched) to allow the face-centered cubic (fcc) austenite to form a body-centered tetragonal (bct) martensite. This produces high dislocation density, thus increasing hardness. The result is the formation of a 700 HV hard surface layer up to 16 mm thick with relatively minor deformations [90]. Unfortunately, this surface engineering method drastically reduces the corrosion resistance by segregating the chromium, and is therefore unsuitable for sealing surfaces exposed to corrosive environments. Nevertheless, this process is used for worm gears that drive valve shafts [90].

2.2.1.3. Diffusion

Superficial hardening can be performed by diffusing metalloids or metals into a material surface. Diffusing metalloids such as carbon (called carburizing) or nitrogen (called nitriding) increases the strength of the surface while reducing its chemical affinity. Carburizing, the first discovered diffusion process, was originally developed using solid coal as the carbon source and a process temperature above 1,000 °C, resulting in a diffusion layer up to 3 mm thick into steel. Since then, carburizing has been refined to reduce part distortion, and gaseous precursors such as carbon dioxide or methane are now commonly used. Nitriding was developed later, using urea and cyanides as a source of nitrogen, which typically starts diffusing into the metal at 600 °C, generating less distortion than carburizing. The two diffusion processes can be combined in a process called nitrocarburizing. One drawback common to carburizing, nitriding, and nitrocarburizing is the potential formation of chromium-based precipitates (precipitation strengthening) such as CrN (1100 HV) and Cr₂C₃ (2150 HV), which decreases the corrosion resistance by segregating chromium. This drawback can be offset by modern high-pressure low-temperature plasma-assisted diffusion processes that retain metalloids within the metal crystalline matrix (solid solution strengthening) [91]. Other diffusion methods include boriding, or using the metalloid bore to form the borides Fe₂B (1750 HV) or CrB₂ (2250 HV) [92], and siliconizing, or using silicon to form the silicide MoSi₂ (1200 HV) [93].

The most commonly used metalloid for diffusion coating in the valve industry is boron. Cataldo (2000) reported that parts manufactured from borided nickel were virtually impervious to attack from hydrochloric, hydrofluoric, and sulfuric acids, and their resistance to abrasion, erosion, and corrosion has been substantiated in several applications [60]. Hood also described diffusion coating processes whereby oxygen is diffused into zirconium to form a zirconia layer, using a fluidized bed furnace process, and where nitrogen is diffused into titanium, tantalum, and niobium to protect materials from sulfuric, hydrologic, and acetic acid service [68]. Figure 2-4 illustrates the strength obtained on steel by the two most commonly used diffusion processes in the valve industry: nitriding and boriding [70].

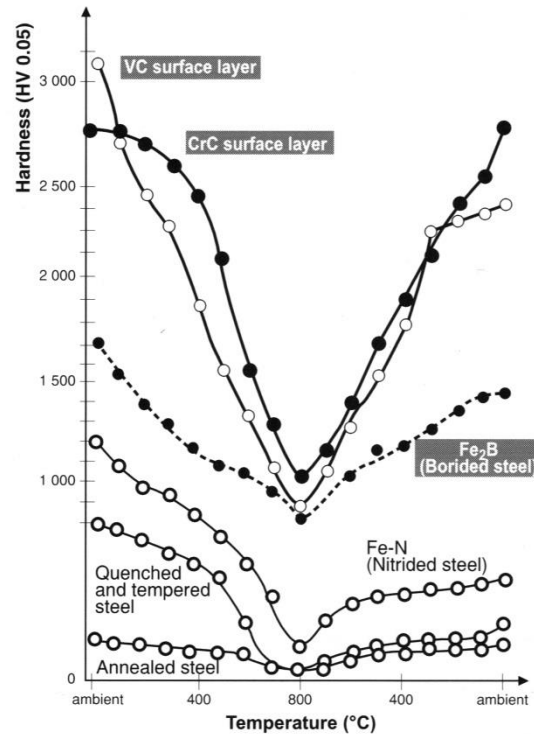


Figure 2-4: Hardness as a function of temperature obtained by diffusion coatings made with different compounds [70].

Materials can also be saturated with metals, most often aluminum and chromium, which are diffused using processes known as aluminizing and chromizing, respectively. The result is oxide formation, which improves the oxidation resistance of coated metals [94]. Aluminizing and chromizing are used mainly on gas turbine parts to further improve the high-temperature oxidation resistance of superalloys. Publicly disclosed in 1914, the process was developed by General Electric Research Laboratories, and was first used on low alloy steel for aircraft engines during the Second World War. Since the 1970s, the process has been applied to cobalt and nickel alloys for modern engines [95]. Other recently developed technologies include tungstenizing (using tungsten) to form WC [96], titanizing (using titanium) to form TiC [97], and vanadizing (using vanadium) to form VC [98].

2.2.2. Coating deposition

The second category of surface engineering methods involves depositing an additional top coat onto the surface to be protected. There is currently a substantial range of film deposition methods

for hard protective coating, each using different processes and materials. The most popular are weld overlay cladding, wet chemical methods, thermal spraying, and vapor deposition methods [99-101]. As mentioned in the introduction, a special effort was made to conduct a thorough review of the literature on weld overlay cladding and thermal spraying, which have been newly introduced at FCSEL.

2.2.2.1. Weld overlay cladding

Weld overlay claddings are metallic coatings bonded onto a substrate by melting both the substrate and coating material during deposition. Under the high temperature of the welding process, a molecular bond is formed with the base metal, resulting in a fully dense, metallurgically bonded coating. Weld overlays have a long history of use in the pipe and valve industry [16, 102].

Among the many welding methods applied today, probably the simplest and most widely used is shielded metal arc welding (SMAW). Stick welding uses a consumable rod, or electrode, which is typically jacketed to minimize oxidation. An electric arc is ignited between the base metal and the tip of the rod. This creates an intense heat that liquefies both the substrate and the rod to form an alloy of the two metals. Metal inert gas (MIG) welding, also called gas metal arc welding (GMAW), is a semi-automated version of SMAW, where instead of a welding rod, the electric arc is formed between the substrate and a consumable wire spool (the electrode) to allow continuous deposition, while the welding gun feeds a constant flow of inert shielding gas around the weld pool to prevent oxidation.

Gas tungsten arc welding (GTAW), formerly known as tungsten inert gas (TIG) welding is an advanced form of MIG in which the electrical arc is generated between a nonconsumable tungsten electrode and the weld pool, providing a more stable electric arc. As in MIG, a constant flow of inert gas around the weld pool prevents oxidation, and the coating material is introduced in wired form by an automatic feeder mechanism [103]. Plasma transfer arc welding (PTAW) is the latest fully adopted evolution of the arc welding process, and is widely used in the valve industry for hardfacing. Although similar to TIG in that an electric arc is formed between a fixed tungsten electrode and a substrate, in PTAW the electric arc is isolated from the shielding gas by

a plasma arc, as illustrated in Figure 2-5. PTAW obtains higher energy density while inputting less energy to the base material compared to other electric arc welding methods. For example, the PTAW temperature is typically around 28,000 °C, versus about 5,500 °C for other arc welding methods.

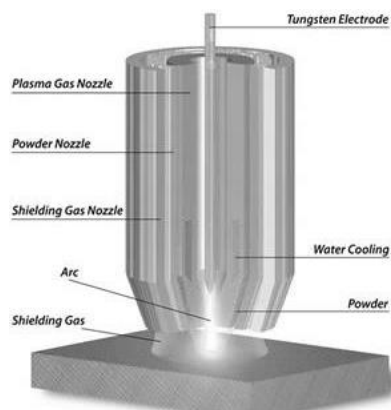


Figure 2-5: Schematic illustration of plasma transfer arc welding [104].

The most recent welding method used in the valve industry, and the one that entails the lowest energy input, is undoubtedly laser welding [105]. Laser welding melts both the substrate and coating using a high-energy-density laser beam, as illustrated in Figure 2-6. As in PTAW, the coating material is automatically fed in powder or wire form to allow continuous welding, and the weld pool is protected by a constant flow of shielding gas.

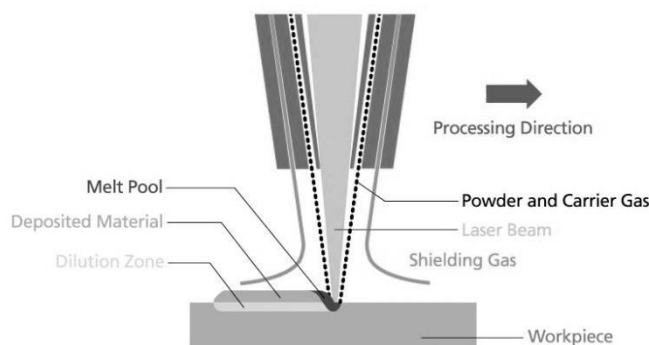


Figure 2-6: Schematic illustration of laser welding [104].

One drawback to the welding process is the formation of a heat-affected zone (HAZ). The HAZ is the area where the substrate has not melted, but its microstructure and the resultant physical properties have been modified by the energy produced during welding. A second drawback to the welding process is the change in the chemistry of the deposited overlay due to an interaction

between the base metal and the overlay alloy, called dilution. To minimize both these drawbacks, high energy density methods that use less heat input to melt the materials are recommended. Figure 2-7 shows the energy density for various welding heat sources [103].

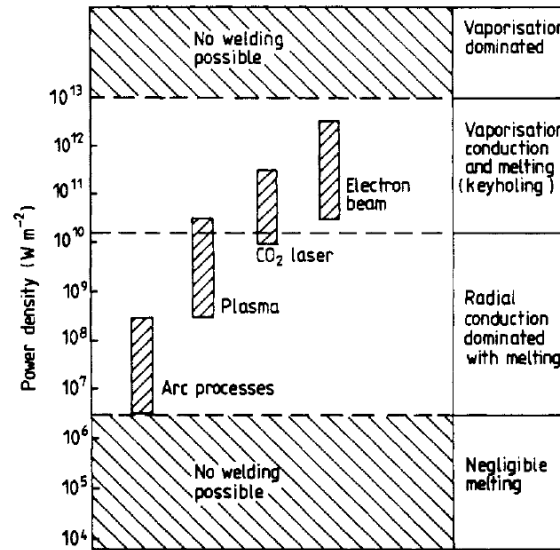


Figure 2-7: Energy density required for various welding methods [103].

As mentioned in the introduction, the cobalt-based superalloy Stellite is by far the most commonly used wear-resistant alloy deposited via weld overlay to protect valves, as reported in numerous publications [16].

Table 2.2: Nominal composition of Stellite 6 (mass %) and physical properties

Co	Cr	W	C	Others	Hardness [HV]	Density [g/cm³]	Melting Range [°C]
Base	27–32	4–6	.9–1.4	Ni, Fe, Si	380–490 HV	8.44	1285–1410

As alternatives to Stellite, iron-based (Norem) or nickel-based (Deloro, Colmonoy) superalloys are preferred when Cobalt has to be avoided (Ref. 2.1.2.2) or when high abrasion resistance at high temperature is required (Ref. 2.1.2.4), respectively. However, high energy input renders weld overlay claddings incompatible with precipitation hardened substrates, and limited hardness yields relatively high wear rates. Consequently, other surface treatments having a more controlled microstructure were developed to compensate for these limitations, as described next.

2.2.2.2. Wet chemical processes

Wet chemical processes are used to deposit alloys and metals that are harder than weld overlays at lower temperature, using relatively simple and economical equipment. They have therefore been extensively used in the valve industry. There are basically two wet chemical processes for producing a coating: electroplating and electroless plating.

(i) *Electroplating*

Electroplating refers to the deposition of a metallic coating onto a metallic or other conducting surface by passing an electric current through a liquid electrolyte. The current produces an oxidizing–reducing reaction, whereby the metal cations are dissolved in the solution and reduced, and they consequently form a coating on an electrode. One major drawback to electroplating is the tendency to exacerbate surface defects as the coating builds up. For the same reason, non-spherical components generate an uneven electrical field, resulting in the build-up of an uneven coating that requires extra thickness and final grinding.

Hard chromium (HC) is the most commonly used electroplated coating. In hard chromium electroplating, an electrolytic bath containing hexavalent chromium (Cr^{6+}) is used to deposit a layer of chromium onto a metal component. The HC layer is typically 50 to 150 μm thick with a microhardness of around 1,000 HV, and with a microcrack network due to the stresses generated during deposition. After plating, a typical surface shows a “cauliflower” morphology, which requires grinding, as seen in Figure 2-8. Although the microcrack network limits corrosion protection, it is advantageous in that it allows lubrication storage, debris evacuation, and improved toughness by withstanding strain without macrofracturing.

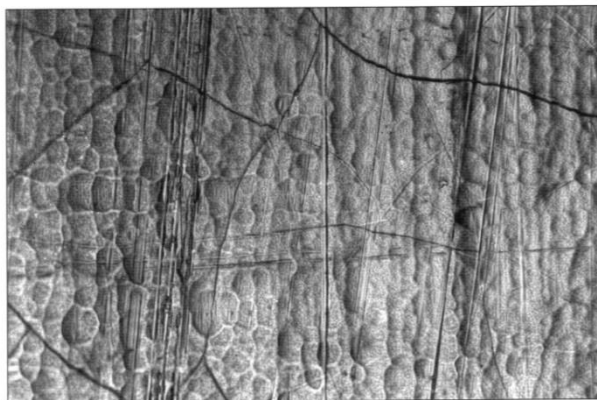


Figure 2-8: Typical surface finish after hard chromium electroplating [70].

Several studies have demonstrated the effectiveness of chromium plating in reducing the wear of components exposed to sliding wear and abrasion while preventing adhesion. The low COF and wear rate of chromium plating are usually attributed to the formation of a Cr_2O_3 passivation film. One limitation of HC is the significant decrease in hardness with increasing temperature: the HC layer shows only 600 HV at 400 °C [70]. As reported by Hadachi et al., HC decrease in hardness is irreversible after 50 thermal cycles from room temperature to 800 °C, which could be due to stress relief [106]. Another drawback is the very limited control of the deposition process, due in part to the low cathode efficiency of Cr^{6+} , which necessitates excessive coating build-up in high current density areas in order to cover low current density areas. The use of Cr^{6+} is further limited by strong environmental concerns raised by the Environmental Protection Agency (EPA) and other government agencies that classify Cr^{6+} as a human carcinogen and one of the high-priority toxic chemicals for voluntary reduction [71]. Nevertheless, HC is unanimously considered the first choice among the wet chemical processes when high wear resistance is required [107]. HC is therefore used to protect not only severe-service valves, but also piston rings, gun barrels, hydraulic rods, and aircraft landing gears.

(ii) *Electroless plating*

Electroless plating is a non-electrical chemical reduction process that, unlike electroplating, uses catalytic reduction in a solution containing a reducing agent. This makes the process insensitive to part geometry, which makes the coating distribution more uniform. The choice of electroplating materials is also limited, the most popular hard compound material being NiP [108]. Electroless nickel plating uses a nickel–phosphorus alloy with phosphorous content from 4 to 13%. After deposition, the nickel plating layer is typically from 10 to 100 μm thick, amorphous, fully dense, and with a microhardness of around 500 HV. Nickel plating can then be precipitation hardened up to 1,000 HV, but it becomes more brittle, and therefore, it generally performs worse than HC on wear tests (nickel phosphide Ni_3P precipitates). Being pore-free, nickel plating seals the substrate from the environment, and is useful as an intermediate layer between the HC and the substrate [109].

Unfortunately, wet coating processes such as hard chrome plating cause significant pollution, and they have steadily lost popularity due to environmental restrictions (Smurkowski 1994). They are now being replaced by alternative coatings such as thermal spray, which are less polluting while offering better consistency and superior tribological performance.

2.2.2.3. Thermal spraying

Thermal spraying (TS) encompasses various methods in which a material powder is totally or partially melted in a high temperature gas flame and then sprayed through a nozzle onto the substrate. The thermal and kinetic energy of the impact deforms the molten or nearly molten droplets of material. These particles strike the surface and undergo rapid deformation and solidification to form disk-like splats, which spread onto the surface and are mechanically anchored to previously deposited splats as illustrated in Figure 2-9. Multiple passes are needed to build up the total coating thickness.

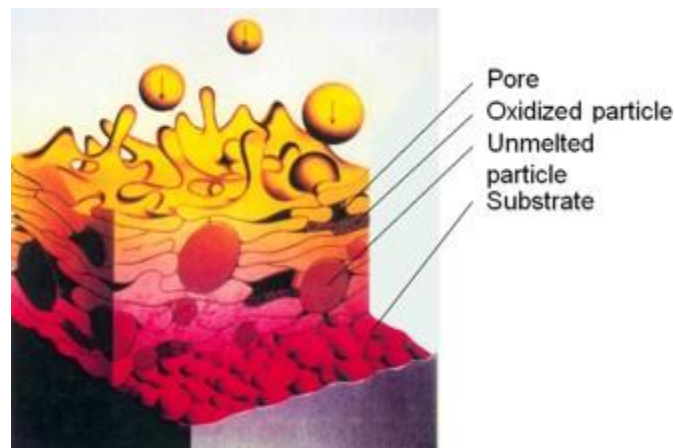


Figure 2-9: Thermal sprayed coating deposition with typical lamellar microstructure [110].

TS processes allow depositing layers containing high concentrations of hard phases, which are difficult to synthesize using the previously described surface engineering methods. As mentioned in the mechanical properties section, the carbides, borides, and oxides produced from the combination of metalloids and metals have the highest bonding energy. Indeed, TS is one of the few surface treatment processes in which these high strength compounds are deposited directly onto component surfaces. Furthermore, TS allows tailoring the chemical composition and

microstructure of the final coating material to obtain the required mechanical and tribological behavior.

The first TS process was invented in 1911 by Max Ulrick Schoop, in Zurich. In his patent, he described a “jet of molten particles forming a coating.” In TS, the coating materials are sprayed at a high deposition rate to form relatively thick coatings ranging from ten to several hundreds of μm [111, 112]. Thermal spray processes fall into three main categories, according to the energy source.

(i) Chemical heat source – Combustion

The first category, called flame spraying, involves burning a combustible material mixed with oxygen to generate thermal and kinetic energy. Several variants of flame spraying have been developed over the years to improve coating density and adhesion. Powder flame spraying was the first TS technology to be adopted, introduced in the 1930s. The powder was simply fed into the middle of a nozzle where it was melted, accelerated toward the substrate by the exhaust gases, and sprayed onto the surface. However, with relatively low speed and high oxygen content, these types of coatings have high porosity and are oxidized over 20%. A typical gun is illustrated in Figure 2-10.

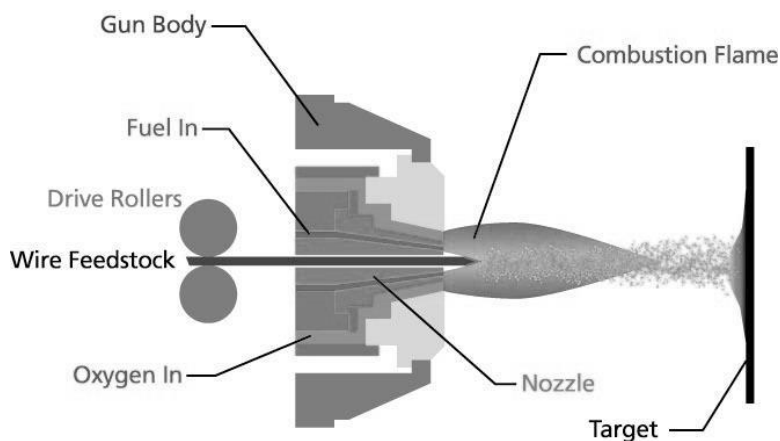


Figure 2-10: Cross section of a basic flame spray gun [104].

The flame spraying process was improved during the 1980s, and today the most commonly used flame spraying process is the High Velocity Oxygen Fuel (HVOF) process (also known as High-Velocity Oxy-Fuel). The main difference from a regular flame spray gun is that the exhaust gases

are compressed in a chamber and then passed through a converging–diverging nozzle where supersonic velocity can be achieved. The powder is typically fed axially into the nozzle, where it is heated and accelerated toward the substrate.

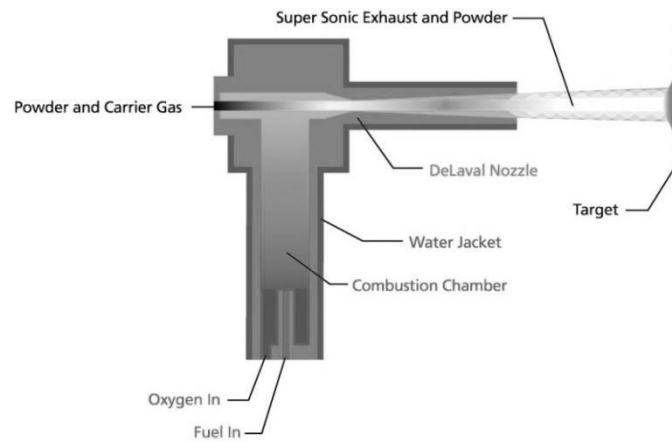


Figure 2-11: Cross section of a High-Velocity Oxy-Fuel gun [104].

HVOF coatings are extensively used as thermal barriers and wear- and abrasion-resistant coatings on turbine blades, valves, and moving machine components [112, 113].

(ii) *Electrical heat source*

The second category of TS uses electricity to generate heat. The first such process was electric arc wire spraying. Two wires of coating material, charged with opposing polarity, are fed into the arc gun. As they come into contact, they generate a large amount of heat, which melts the tips. Compressed air is used to atomize the molten material and accelerate it toward the substrate (Figure 2-12). The electric charge generates higher temperatures than combustion does and reduces the risk of contamination from combustion by-products.

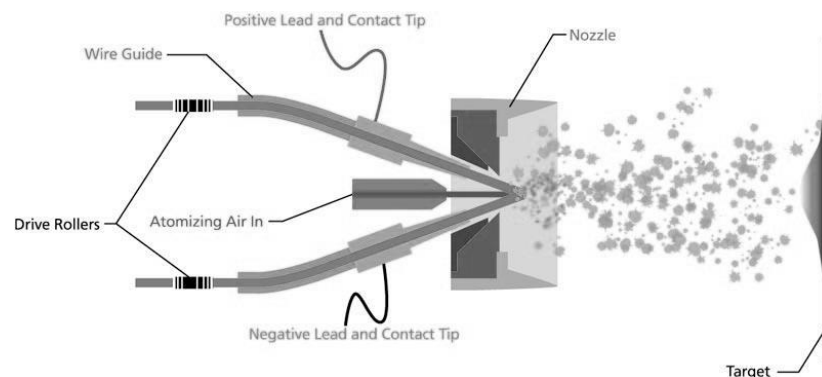


Figure 2-12: Cross section of an arc wire gun [104].

One major drawback to arc wire spraying is that the material must be conductive and in the form of a wire. The second limitation, similar to flame spraying, is the relatively low particle velocity obtained. Air plasma spraying (APS) was developed to offset both these limitations. In plasma spraying, the material can be deposited in powder form, including non-conductive materials such as ceramics. The converging–diverging nozzle also allows the particles to exceed supersonic velocity as illustrated in Figure 2-13. Plasma spraying can also be carried out in a controlled environment inside a sealed chamber in low-pressure inert gas atmosphere to mitigate oxidation and is then referred to as vacuum plasma spraying (VPS).

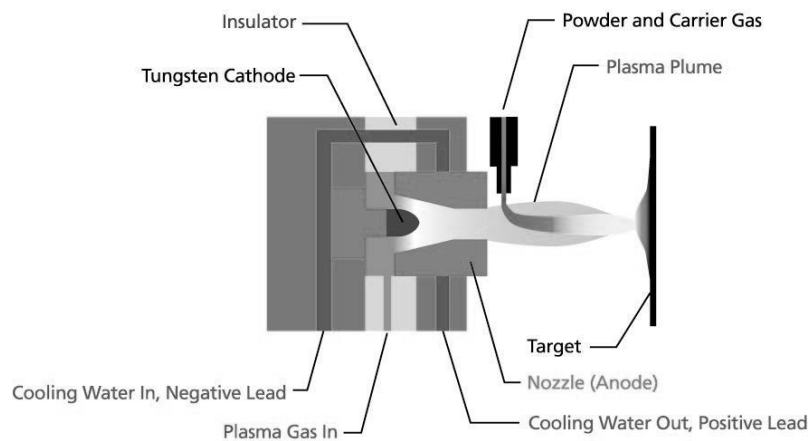


Figure 2-13: Cross section of a plasma spray gun [104].

(iii) *Cold spraying*

As the name implies, cold spraying uses mainly kinetic energy to deposit a coating. This method was developed in Russia in the 1990s when a coating was accidentally formed during erosion tests. In cold spraying, particles are accelerated to very high speeds by the carrier gas, which is forced through a converging–diverging nozzle. Particles with sufficient kinetic energy deform plastically and bond mechanically with the substrate to form a coating. The critical velocity required to form bonding depends on the material properties, the powder size, and temperature. Soft metals such as Cu and Al are best suited for cold spraying, but coatings made with other materials (W, Ta, Ti, MCrAlY, WC–Co, etc.) have been reported [114].

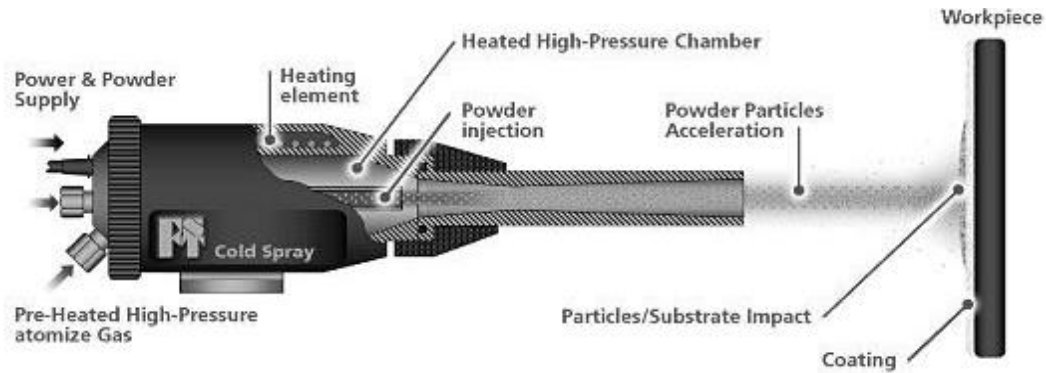


Figure 2-14: Cross section of a cold spray gun [104].

(iv) *Spraying and Fusing*

Spraying and fusing (S&F) is a variant of TS in which a self-fluxing alloy is first deposited onto the surface using one of the TS processes described above. In a second step, the coating material is heated above its melting point, providing a metallurgical bond (also called a diffusion bond) between the splats and substrate while sintering it. This fusing step can be performed with various heating sources, including an oxy-acetylene torch and/or a controlled vacuum furnace. S&F coatings combine the advantage of weld overlay cladding by forming a metallurgical bond and the flexibility of thermal spraying in terms of application. S&F is frequently used to deposit abrasion-resistant coatings with high packing density and cohesive strength [115].

With the exception of S&F, a limitation of TS is the weak mechanical bond that is formed between the splats and substrate, which limits both the adhesive and cohesive strength of the coating, increasing the risk of spallation. This mechanical bond is further compromised by the presence of porosities in the TS coating, which increase the risk of crevice corrosion. Therefore, when high bond strength and/or low porosity are required, the process must be optimized with respect to the combination of thermal and kinetic energy (see Figure 2-15).

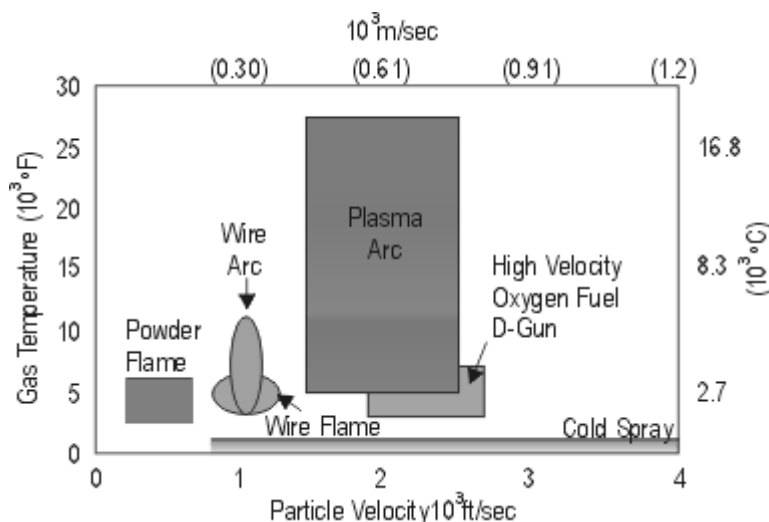


Figure 2-15: Particle velocity and gas temperature for various thermal spray processes [110].

In addition to the mechanical bond and porosity, a third limitation of TS, as described in Chapter 5, and with the exception of S&F, is the quenching of the relatively hot sprayed particles on impact with the colder substrate. Consequently, the deposited material is typically in tension and in a metastable state, with some amorphous phases; even tough residual stresses can be controlled via deposition parameters, some HVOF-deposited and most cold spray-coatings end it up in compression.

Hard materials deposited by thermal spray are generally classified into three categories: ceramics, cermets, and alloys. The pure ceramic materials, such as Cr_2O_3 and $\text{TiO}_2\text{-Cr}_2\text{O}_3$, are usually deposited by APS because they have a higher melting temperature and are oxidation-resistant. Table 2.3 shows that APS ceramic coating exhibits microhardness up to 1,500 HV, providing greater sliding wear resistance than hard chromium plating or Stellite 6. In addition to superior sliding wear resistance, APS ceramic coatings have a low CTE while maintaining high hardness at high temperatures, and are known for corrosion resistance [116]. Despite their excellent hardness, however, APS ceramic coatings have relatively low resistance to abrasive wear, as shown in Figure 2-16. This puzzling behavior has been attributed to the relatively low bond strength between splats and the brittle nature of ceramics, both properties that favor crack propagation and debris formation during abrasive wear [117]. This failure mechanism can be mitigated by either controlling the chemical composition of the coating (i.e., blending ceramics

with differing ductility) or by controlling the microstructure and grain morphology through the deposition process and/or the original powder (i.e., fine-structured ceramics are more ductile than conventional ceramics) [118].

Table 2.3: Most commonly used TS coatings for severe-service valves [119].

Coating Material	Typical TS deposition method	Nominal Composition (mass %)	Microhardness at room temperature HV-300g	Sliding wear rate Pin-on-disc test at room temperature mm ³ /(N.m)*
Ceramics	Plasma Spraying	Cr ₂ O ₃	1500	5.5x10 ⁻⁸
		TiO ₂ – Cr ₂ O ₃	900	3.7x10 ⁻⁵
Cermets	HVOF	Cr ₃ C ₂ – NiCr (75/25)	900	1.6x10 ⁻⁶
		WC – Co (83/17)	1200	1.5x10 ⁻⁸
		WC – NiCr (73/20/7)	1100	2.1x10 ⁻⁸
Self-fluxing Alloys	Spraying & Fusing	NiCrB	800	2.0x10 ⁻⁵
		NiCrWB	750	1.8x10 ⁻⁵
References		HC electroplating	1000	3.6x10 ⁻⁴ **
		Stellite 6 overlay	450	3.3x10 ⁻⁵

*A normal load of 25 N was applied to a tungsten carbide 4.75 mm diameter ball. The diameter of the wear track ring was 7 mm and the rotation speed was 546 revolutions per minute.

**Substrate was reached.

Another solution is to form composite materials composed of ceramic particles embedded into a metallic matrix (see Figure 2-17). Called cermets, these composites constitute the second category of thermal spray materials, with higher cohesive strength than pure ceramics [112]. This additional cohesive strength compensates for the lower hardness, and produces greater resistance to abrasive wear, as shown in Figure 2-16. Given their low melting point and temperature-sensitive constituents, cermets are usually deposited using HVOF.

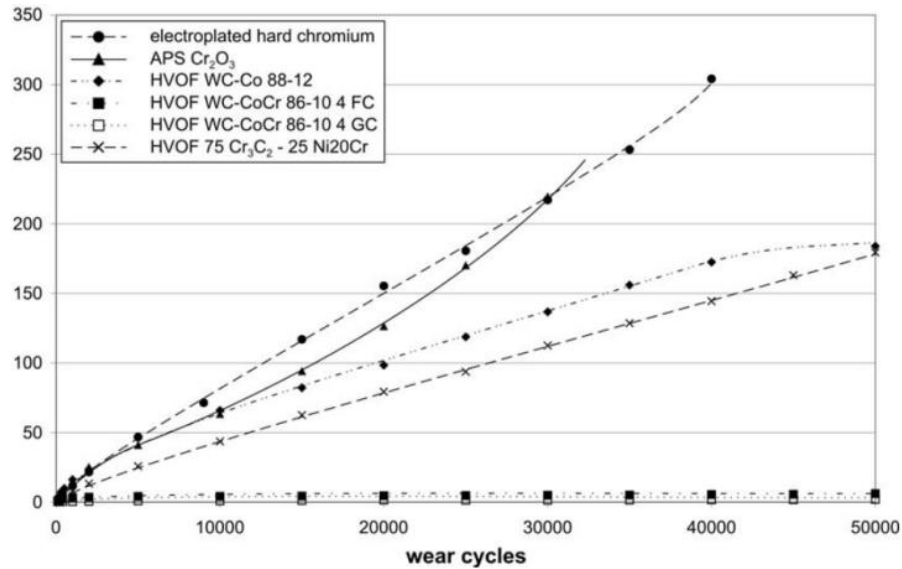


Figure 2-16: Wear rate of several TS coatings compared to HC coatings during the Taber Abraser test – ASTM F1978 [117].

Although metallic alloys can also be deposited by TS, their porosity and mechanical anchoring limit the mechanical and tribological performance. Therefore, with the exception of S&F, TS is mainly used to deposit alloys when the deposited overlay materials crack during welding (Tribaloy alloys) or when the substrate cannot tolerate high temperature (precipitation hardened materials). S&F allows sintering and diffusion at the interface with the substrate and between the splats. However, it is limited to self-fluxing alloys with low fusion temperature, such as NiCrB and NiWCrB. As reported in several publications, the traditional S&F process provides similar microstructures and wear performance to those of modern overlay cladding processes such as laser deposition, while being less controllable [120-122].

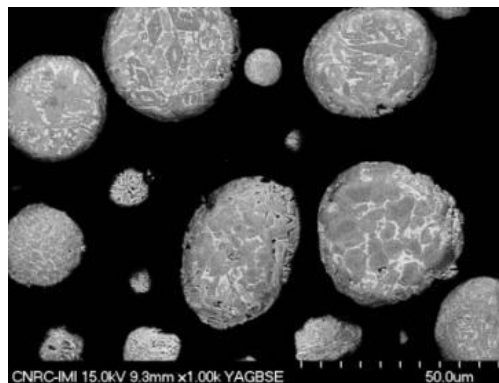


Figure 2-17: Cross section of agglomerated and sintered cermet powder prior to deposition.

Despite their strength and versatility, TS coatings have demonstrated certain limitations in several applications, including fossil power generation, as described in Chapter 5, and in mining, as described in Chapter 6. These limitations have called for the development of alternative coating systems such as PVD and PECVD.

2.2.2.4. Vapor deposition

The vapor deposition methods can be divided into two categories: 1) physical vapor deposition (PVD), which uses a solid or liquid precursor, and 2) chemical vapor deposition (CVD), which uses a chemical vapor precursor. Both methods use vacuum equipment operating under sub-atmospheric pressure to form thin films.

(i) *Physical Vapor Deposition*

PVD involves the formation of vapors from a solid source using thermal energy (evaporation) or momentum transfer (sputtering). It is usually performed at low pressure to allow directional transport of gaseous species from the source to the substrate.

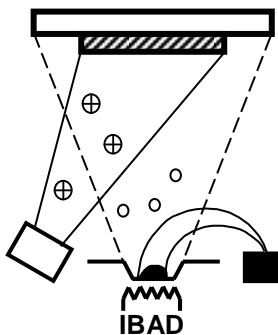


Figure 2-18: A typical physical vapor deposition system [123].

In the evaporation process, the substrate is placed inside a vacuum chamber where the material to be deposited is heated to evaporation point and condensed onto the substrate surfaces. The growing film can be simultaneously bombarded from an independent ion source in order to increase the film density so called ion beam assisted deposition (IBAD) as shown on Figure 2-18.

In the sputtering process, the material is vaporized at lower temperature than for evaporation, using ion bombardment, which causes the atoms of the target material to sputter and condense

onto the substrate surfaces. PVD-produced films have imperfections due to the line-of-sight nature of the PVD deposition process, whereby the flux lands onto only higher parts of the developing film. Consequently, CVD is used when technically and economically feasible as it requires higher temperature and complex (corrosive) chemistry.

(ii) *Chemical Vapor Deposition*

Chemical vapor deposition (CVD) is a chemical thin film deposition process in which the substrate is exposed to one or more volatile precursors that react on the substrate surface to produce the desired coating by thermal activation as illustrated on Figure 2-19. Frequently, this process also produces volatile by-products, which are removed by gas flow through the reaction chamber. When plasma is used to increase the chemical reaction rates of the precursors, the process is referred to as plasma enhanced CVD (PECVD).

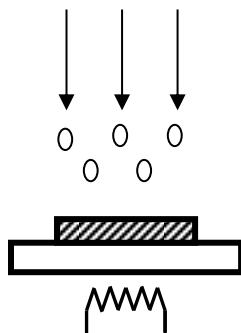


Figure 2-19: Schematic representation of a typical chemical vapor deposition system [123].

PVD and CVD are used to prepare various types of relatively thin (up to several μm) coatings. High controllability makes these processes very attractive for producing nitrides and carbides of transition metals, as well as oxides, borides, and diamond films [100]. Vapor deposition is compatible with a range of substrates, including metals and metal alloys (e.g., steel, titanium, and aluminum), cemented carbides, and ceramics. The operation is generally flexible enough to provide good process control, and hence control of the film structure and composition. It also produces few contaminants and is thus environmentally friendly. Furthermore, because many PVD- and CVD-produced hard films are made with transition metal nitrides and carbides, they have advantageous mechanical and tribological properties due to the possibility of mixing covalent and metallic bonds.

Covalently bonded carbon and boron compounds have emerged as highly suitable materials for CVD. These include polycrystalline or nanocrystalline diamond, diamond-like carbon (DLC), CN_x , BN, BC, and some ternary compounds such as B-N-C or Si-C-N [124]. The excellent mechanical properties, including high hardness, high erosion and corrosion resistance [125], and low surface friction, combined with high density and chemical inertness [126] make these materials particularly appropriate for nuclear, military, space, and valve applications as well as high wear environments.

Using the traditional binary and ternary systems described above, these coatings frequently have limited hardness and toughness due to the formation and propagation of dislocations and cracks. More recently, research has focused on the design and development of thin film systems with a microstructure controlled at the nanometer scale, for example, nanocomposites.

In general, nanocomposite coatings (NC) formed by particles that are several to several tens of nanometers in size have greatly enhanced mechanical, tribological, and other functional properties while exhibiting superhardness (> 40 GPa), high toughness, and high thermal stability [127-130]. They have also shown very high erosion wear and superior corrosion resistance [131, 132]. These features are due to the high packing density of the film, and particularly the introduction of internal interfaces that prevent crack propagation under loading. The critical parameters for producing these structure-controlled phase precipitation materials are the grain size, intergranular distance, and type of interface [133, 134]. Recent advances in the field, including better understanding of deposition and characterization methods, have allowed controlling these parameters as illustrated on Figure 2-20.

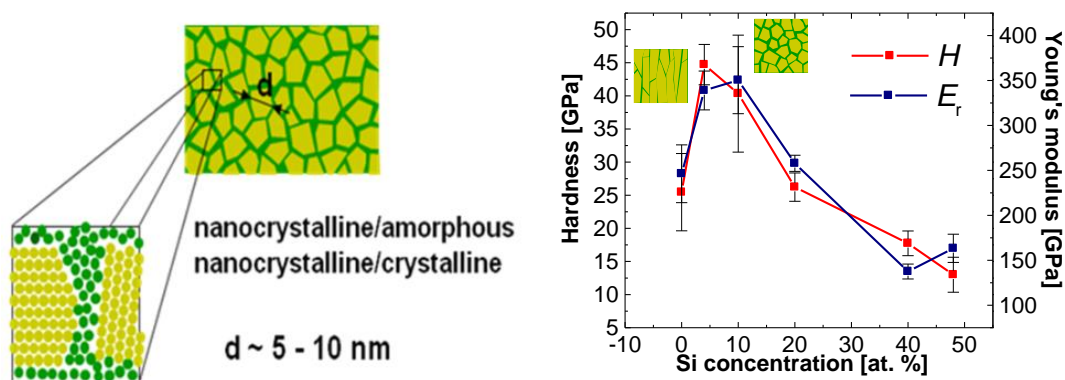


Figure 2-20: nanocrystalline-TiN/aSiN nanocomposite formation and mechanical properties [128].

The nc-TiCN/a-SiCN quaternary NC coating system developed at FCSEL has demonstrated exceptional solid particle erosion resistance, high oxidation resistance, and excellent tribological properties [128]. Although the Ti-Si-C-N system produces excellent mechanical properties, its adhesion and high-temperature oxidation resistance can be improved by adding alloying elements. Elements such as Al, B, and V [135-138] have been shown to diffuse to the surface and form oxides, which lower the friction and protect against oxidation, while the hard structure of the nitride provides good wear resistance. Furthermore, the compatibility of this NC material with application-specific substrates can be greatly improved by reducing its elastic modulus E by adding a more ductile element (e.g., Ni, Cu [138]).

According to the Hall–Petch equation, superhardness can be obtained in hard polycrystalline materials when the grain boundary sliding is inhibited by introducing strong interfaces. This is done by creating a nanocrystalline layer consisting of nanocrystals that are embedded in a matrix. This nanocomposite material deforms only when cracks form and grow in the matrix. In the available theoretical models [134], the crack formation and growth mechanisms are scaled down from traditional fracture mechanics. Both the grain size and the intergranular distance must be controlled and optimized to obtain superhardness.

For use in advanced protective coatings, boron carbide (BC) appears very promising. It is one of the hardest materials known to man, after diamond and cubic boron nitride. Depending on the deposition conditions and the carbon content, various types of BC can be produced, both crystalline (rhombohedral and tetragonal) and amorphous. The rhombohedral phase is the hardest of the boron carbides, with H at up to 50 GPa [139].

2.3. Surface mechanical response

The tribological behavior of a coating system is intimately connected to the intrinsic properties of the composite materials. Among others, hardness, modulus of elasticity, toughness, load-carrying capacity, adhesion, and thermal expansion determine contact wear behavior.

2.3.1. Hardness

The ability of a surface to resist local plastic deformation is called its hardness (H). Hardness has long been considered the main parameter impacting the sliding wear of materials. According to the classical Archard wear equation, the volume loss of a material is directly proportional to the applied normal load (i.e., force) and the sliding distance and inversely proportional to the hardness or yield strength of the softer surface [140].

$$Q = \frac{\text{Constant} * \text{Load} * \text{Sliding Distance}}{H} \quad (1)$$

In 1900, Johan August Brinell proposed the first modern methodology to measure the yield strength of material surfaces. His procedure was the basis for the first standard hardness test, which is now covered by ISO 6506 and ASTM E10-12. According to the Brinell procedure, the material surface is indented at a known load using a hardened steel or carbide ball called an indenter. As the indenter penetrates the surface, the diameter of the contact area increases while the nominal contact pressure (p) decreases until equilibrium is reached. After the test, the surface imprint left by the indenter is measured and the nominal contact pressure at equilibrium is calculated using the following equation:

$$p = \frac{\text{Load}}{\text{Projected Contact Area}} \quad (2)$$

When using this procedure on steel plates, Brinell noticed that p , which was expected to be constant for bulk material, increased with increasing load, most probably due to strain hardening. Based on this observation, he developed the Brinell Hardness Number (BHN), which provides hardness numbers for steel that are almost unaffected by load, as follows:

$$BHN = \frac{\text{Load}}{\text{Surface area of the indentation}} \quad (3)$$

Since then, other indentation tests using different indenter shapes and loads have been developed for specific purposes, including the Vickers and Knoop hardness tests. However, the basic principle of measuring the impression left by the indenter remains the same, with nominal contact pressure as a dimension of H. Tabor (1951) further demonstrated that for bulk material

having a constant yield stress σ_y , only one third of the stress plays a role in plastic flow, and there is a direct correlation between H and the yield strength of the bulk isotropic material [141], as follows:

$$H \sim 3 * \sigma_y \quad (4)$$

The yield strength is the stress at which a material begins to deform plastically, as illustrated in Figure 2-21. Therefore, H can be increased by tailoring the strength of the bulk material to prevent plastic deformation, thereby increasing hardness and reducing wear.

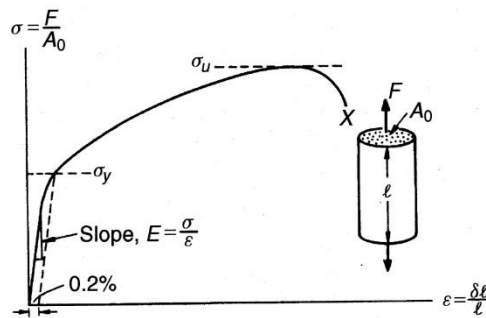


Figure 2-21: Stress-strain curve for a ductile material [142].

More recently, depth-sensing indentation (DSI) methods have been developed to determine hardness at very shallow depths, where H is calculated from the load-displacement curve as well as other elastic-plastic properties of the material. As described in detail in Chapter 3, these methods are particularly suitable for hard elastic materials such as nanostructured materials, where, as demonstrated by Hill (1949), H is also a function of the elastic-plastic properties [143].

As demonstrated unintentionally by Brinell, material strength can be controlled by work hardening, which means increasing the dislocation density in the lattice structure. In other words, materials with fewer imperfections in the lattice structure offer less resistance to plastic deformation compared to materials with high dislocation density. For example, forgings are known to have higher strength than castings for a given material: the forging manufacturing process produces higher dislocation density compared to the casting process, which produces fewer lattice imperfections.

chemical composition, because not only do the two phases affect the material strength, so do the size and shape of the precipitates and their distribution across the alloy.

This leads to the fourth strengthening mechanism, which consists of controlling the grain morphology of a given material. As demonstrated by both Hall [148] and Petch [149], the yield strength of a material is inversely proportional to the square root of the grain size, using the following equation:

$$\sigma_y = \sigma_o + \frac{k}{\sqrt{d}} \quad (5)$$

where σ_y is the yield strength of the hardened material, σ_o is the yield strength of the annealed material, d is the grain size, and k is a constant. Therefore, according to the classical Hall–Petch equation, hardness can be controlled in hard polycrystalline materials when the grain-boundary dislocation is inhibited by a large number of strong interfaces. Stronger interfaces can be produced by a structure consisting of nanocrystals embedded in an amorphous matrix. Both the grain size and the intergranular distance must be controlled to optimize hardness. Chokshi (1989) validated this finding down to a crystallite size of 5 to 50 nm in a study of copper and palladium [150]. Below this limit, certain flaws in the material at the grain boundary tend to produce decreases in strength and hardness, known as the inverse Hall–Petch effect [151].

2.3.2. Modulus of elasticity

Although hardness largely determines the sliding wear resistance of a surface, other mechanical properties exert some influence as well. As Hertz demonstrated in his classic paper *On the contact of elastic solids*, the modulus of elasticity (E) affects the contact pressure between solids [152]. As shown in Figure 2-21 the modulus of elasticity of a material is the slope of its stress–strain curve, and it describes the material’s capacity to deform elastically under load, as defined by Hooke’s law. Thus, less rigid materials have higher E (i.e., smaller deformation), and less elastic materials have lower E (i.e., greater deformation).

For example, the maximum contact pressure P_{\max} between two spheres that are pressed against each other and have the same radius R is equal to:

$$P_{\max} = \frac{1}{\pi} * \left(\frac{6 * Load * E^*{}^2}{R^2} \right)^{1/3} \quad (6)$$

where $\frac{1}{E^*} = \frac{1-\nu_1}{E_1} + \frac{1-\nu_2}{E_2}$, E_1 , and E_2 are the elastic moduli, and ν_1 and ν_2 are the Poisson ratios for each material. Leyland [153] and Musil [135] later discovered that the wear rate is not only proportional to the hardness, but also inversely proportional to the material's modulus of elasticity. This seemingly intuitive result is due to the fact that materials with low E are more elastic, resulting in lower contact pressure for a given load. Consequently, the ratio of the elastic strain to failure (H/E) is a significant indicator of the wear behavior, and should be maximized to reduce wear. Another approach to predicting the wear resistance of a coating material is to calculate the material's resistance to plastic deformation using Johnson's proposed ratio H^3/E^2 , whereby greater resistance to plastic deformation results in a lower wear rate [154].

2.3.3. Toughness

Interestingly, combining high H with low E creates the conditions for greater material toughness. The toughness of a material is determined by its capacity to absorb energy and to plastically deform prior to crack rupture. Toughness is therefore proportional to the maximum strain that a material can withstand prior to fracture. Toughness can be assessed by different methods, including the strain-to-fracture test, which measures the amount of strain required to fracture, and the fracture toughness (K_{Ic}) test, which measures the resistance to crack propagation up to rupture. Strengthening can produce a transition from ductile behavior, as shown in Figure 2-21, to the brittle behavior that is typical of ceramics, where no plastic deformation occurs before fracture, as shown in Figure 2-23.

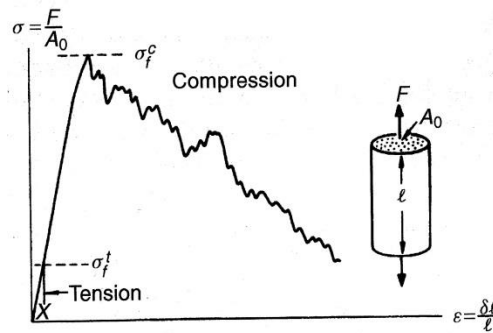


Figure 2-23: Stress–strain curve for brittle material in tension and in compression [142].

Figure 2-24, published by Zum Gahr, shows various types of plastics, ceramics, and metallic alloys as a function of H and K_{Ic} , illustrating how the ductility of the materials decreases with hardening, and highlighting the trade-off between strength and toughness.

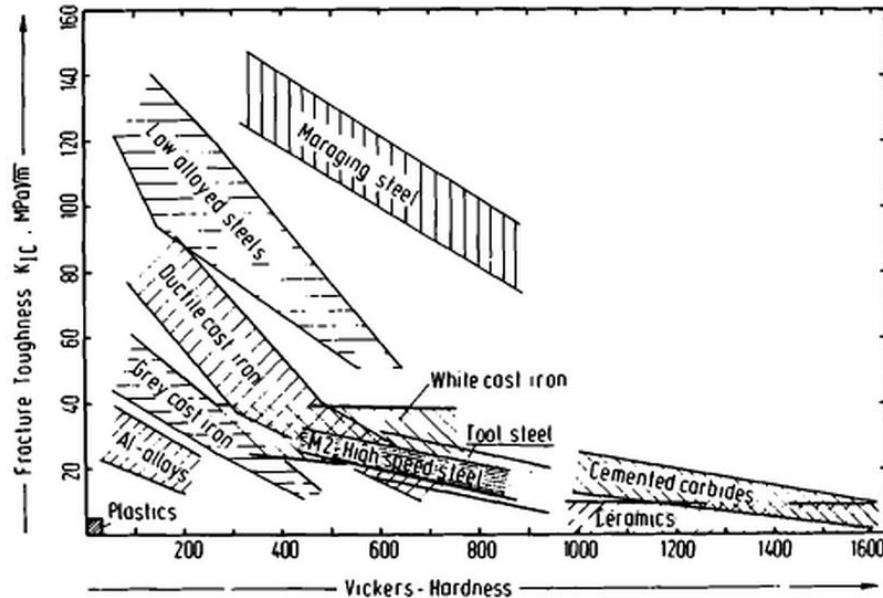


Figure 2-24: Schematic representation of fracture toughness as a function of yield stress [155].

The main explanation for this ductility loss is the very high E that is generally associated with high H [156]. Zhang's theoretical models show that although superhard nanocomposite materials are highly resistant to deformation, they can deform when cracks form and grow in the matrix [134]. Fortunately, hard brittle materials can be toughened by adding a ductile component, as discussed in Appendix A [136].

2.3.4. Load-carrying capacity

Hardness, modulus of elasticity, and toughness are the three classical mechanical properties that determine a material's wear behavior. However, in the case of a coating material, several authors have found that when localized stress fields extend beyond the coating thickness, they can produce permanent deformation at the coating-substrate interface or within the base material without necessarily exceeding the yield strength of the coating itself. The load-carrying capacity is therefore the capacity of a surface to distribute peak stresses generated by localized loading that do not exceed the yield strength of the coating itself without developing permanent

deformation, which includes brinelling (plastic deformation of the substrate without coating fracture), the eggshell effect (strain of the substrate up to coating fracture), and spallation (coating–substrate interface fracture). Although the load-carrying capacity can be controlled by adjusting the mechanical properties of the surface treatment, particularly thickness and modulus of elasticity, as shown in Figure 2-25, the mechanical properties of the submaterials also play a critical role in regulating stresses within the coating, base material, and interface. This also applies to the addition of interlayers, as discussed in Chapter 5: one or more interlayers allow for gradual changes in the mechanical properties, thereby reducing the elasto-plastic gradient and peak stresses and hence preventing both brinelling and the eggshell effect [157, 158].

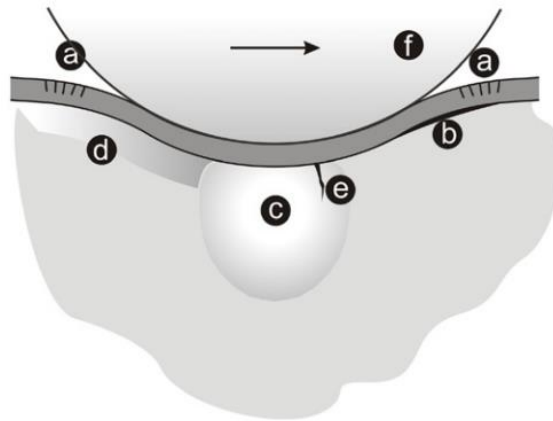


Figure 2-25: Schematic illustration of various limiting factors that determine the load-carrying capacity of a coated surface. Limiting factors: (a) coating fracture, (b) spallation, (c) substrate elastic deformation, (d) substrate plastic deformation, (e) substrate fracture, and (f) plowing friction [159].

2.3.5. Adhesion

Hardness, modulus of elasticity, toughness, and load-carrying capacity are the main mechanical properties, along with microstructure, that determine the behavior of a material when exposed to abrasion, erosion, and sliding contact. However, these properties do not reflect the material's tendency to adhere to a counter body. Adhesion between contacting bodies should be distinguished from coating-to-substrate adhesion. There is no unified theory of adhesion and adhesive wear, and there is considerable controversy in the literature on this topic. Materials show significant differences in properties, and as originally proposed by Roach in 1956, mutually soluble elements tend to adhere and therefore should not be slid against each other

[160]. This theory has been partially invalidated by several counterexamples, such as pure chromium, which slides well on steel despite being soluble into it. The sliding performance of chromium can be explained by the Cr_2O_3 passivation layer that forms naturally over the surface, and by a second theory developed by Buckley in 1981, whereby chemically active materials that are electron donors have a greater tendency to adhere than passive materials such as chromium [161]. Furthermore, as proposed by Buckley and Czichos, the lattice structure appears to have a significant effect on adhesion: close-packed hexagonal materials having fewer slip systems (e.g., graphite, molybdenum disulfide, or boron nitride) show lower adhesion than more ductile face-centered and body-centered materials for a given hardness [18, 162]. Debris generated during wear tests has also been shown to affect adhesion, as it tends to increase the contact pressure between the two bodies by reducing the contact area. Debris is usually produced by the two bodies, and is work hardened, and therefore also capable of scoring them.

In certain cases, adhesive wear is beneficial when it favors the retention of a transfer film that reduces the wear rate and/or the coefficient of friction, as described in Chapter 3. This can be explained by the formation of low-shear-strength films such as a micro-graphite layer (graphitization) over a diamond-like coating, or an oxide layer (passivation) over hard chrome plating and nickel-based superalloys. These layers release a small amount of debris that reduces friction while minimizing wear volume (i.e., a solid lubricant). The tribomechanical properties of the transfer microfilm are influenced by the environment (e.g., chemical composition, temperature) and the contact conditions (e.g., local pressure and flash temperature, which can exceed $1000\text{ }^\circ\text{C}$) [163].

Although there is no commonly accepted theory of adhesion, adhesion does in fact occur, and it can strongly impact the wear rate and the friction coefficient, sometimes up to premature failure (i.e., galling). Therefore, material combinations must be carefully selected and debris and transfer films must be controlled in order to control both adhesion and sliding wear. Given the ongoing theoretical controversy, testing remains the most conservative method to ensure proper materials selection and contact design.

2.3.6. Thermal expansion

Thermal expansion is the tendency of a material to change in volume in response to a change in temperature. The degree of expansion divided by the change in temperature is called the coefficient of thermal expansion (CTE). This property, which is intrinsic to every material, has a critical impact on the internal and interfacial stresses after coating deposition (residual stress) and during contact (thermal stress). As described in Chapter 4, a thermal expansion mismatch between the substrate (CTE_s) and the coating (CTE_c) along with variations in temperature (ΔT) and the modulus of elasticity of the coating (E_c) can produce detrimental thermal stresses. The following equation is commonly used to approximate the thermal stresses generated in a coating with change in temperature [164, 165]:

$$\sigma_{th} = E_c \Delta T (CTE_c - CTE_s) \quad (7)$$

The differences in the coefficient of thermal expansion (CTE) between the coating and the substrate contribute to thermal stresses, which also vary with the temperature gradient and the modulus of elasticity for the coating and substrate.

CHAPTER 3 EXPERIMENTAL METHODOLOGY

This research thesis focuses on the development of innovative protective coatings and deposition processes to advance valve technology. Three specific objectives are targeted, as follows: 1) the development of alternatives to hard chromium electroplating; 2) an investigation of recurrent failures in the field; and 3) the development of new coating architectures. For practical applications, the mechanical and tribological properties and the microstructure of protective coatings are of critical importance [166]. The film has to adhere to the substrate, resist static and dynamic mechanical contact, and withstand the effects of the working environment. This chapter presents an overview of the methods used to assess these properties in the studies covered in this thesis.

3.1. Mechanical characterization

3.1.1. Microhardness

Microhardness (MH) measurements were performed using a micro scratch tester (MST) (CSM, Peseux, Switzerland) equipped with a Vickers indenter under loads from 5 to 30N. Indent sizes were assessed with an optical microscope. Ten indentations were performed on each sample.

3.1.2. Load-carrying capacity

The load-carrying capacity of the coating systems was quantitatively assessed with surface hardness measurements using similar equipment to that used for microhardness, at loads varying from 5 N to 30 N and a dwell time of 30 seconds. Macrohardness measurements were also performed using standard Rockwell equipment at loads varying from 15 Kg to 150 Kg. All indent sizes were assessed using an optical microscope, including indents made by the Rockwell diamond stylus (120 ° cone angle, 200 μ m radius). The corresponding hardness values were then calculated as the ratio between the load and the total contact area, estimated based on the nominal indenter size.

3.1.3. Nanohardness and modulus of elasticity

Nanohardness H_N and the reduced modulus of elasticity E_r were assessed using a triboindenter (Hysitron Inc., Minneapolis, USA) equipped with a Berkovich pyramidal indenter tip. The

maximum load used to assess H_N and E_r was 10 mN. The test procedure involves continuous monitoring of load and indenter position during loading and unloading cycles. An example of a load–displacement (F - h) curve is shown in Figure 3-1. The load–unload curve is measured as a function of penetration depth at 1 nm resolution. H_N and E_r are calculated according to the Oliver–Pharr method [167] and based on 100 measurements per coating. The initial slope of the unload curve at the maximum load is defined as the stiffness S of the material, which is used together with an experimentally derived tip area function to calculate H_N and E_r .

$$H_N = \frac{F_{\max}}{A} \quad (8)$$

$$E_r = \frac{1}{2} \frac{dF}{dh} \left(\frac{\pi}{A} \right)^{1/2} \quad (9)$$

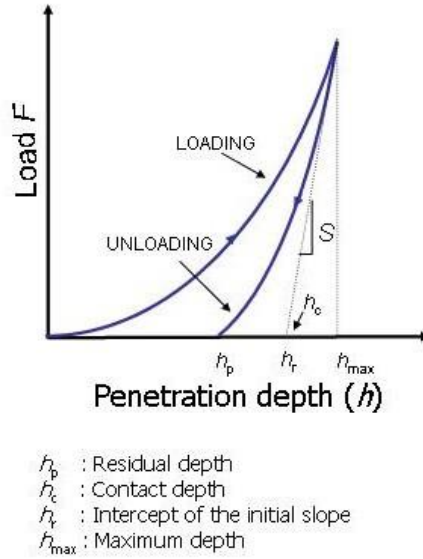


Figure 3-1: Typical load–displacement curve obtained by depth-sensing indentation.

where F_{\max} is the maximum applied load, A is the surface area function, and $S_{\max} = dF/dh$ is the stiffness at the maximum load. In this case, E_r is the reduced Young's modulus:

$$\frac{1}{E_r} = \frac{1-\nu'}{E'} + \frac{1-\nu_i}{E_i} \quad (10)$$

where E' and E_i are the elastic modulus of the film and the indenter, respectively, and ν' and ν_i are the Poisson's ratio of the film and the indenter, respectively. For a diamond indenter, $E_i =$

1140 GPa and $\nu_i = 0.07$. The elastic recovery R can then be calculated from the differences in the maximum and residual depth obtained from the F – h curve (see Figure 3-1):

$$R = \frac{h_{\max} - h_p}{h_{\max}} \quad (11)$$

3.1.4. Scratch hardness

Scratch hardness (H_s) was measured by the MST equipped with a hemispherical diamond Rockwell C stylus (50 μ m tip radius) at a constant 10N load. The scratch length was set at 5 mm and the sliding speed was kept constant at 6 mm/min. Three scratches were performed on each assessed coating. Scratch width was measured at three positions on each scratch track using an optical microscope. H_s was calculated using the formula $H_s = \frac{8 \cdot F}{\pi \cdot w^2}$, as described by Suresh and al. [168], where w is the scratch width (m) and F is the applied load (N).

3.1.5. Sliding wear resistance

The tribological properties of the coatings were assessed with pin-on-disk (CSM, Peseux, Switzerland) and pin-on-flat linear reciprocating tribometers (Tricomat, Montreal, Canada) using different parameters according to the individual studies. After wear testing, wear tracks were inspected using a profilometer to determine the wear volume. The wear coefficient K was calculated using the formula $K = \frac{V}{F \cdot S}$, where V is the worn volume (mm³), S is the sliding distance (m), and F is the load (N). SEM observations were made to assess the wear mechanisms.

3.1.6. Friction coefficients

This test method involved a typical pin-on-disk test apparatus: a ball-shaped upper specimen that slides against a rotating disk as a lower specimen under a prescribed set of conditions (contact load, speed, etc.). The load is applied vertically downward with a motor-driven carriage that uses the force–load sensor for feedback to maintain a constant load. This test allows monitoring the actual dynamic normal load, friction force, and friction coefficient during testing.

3.1.7. Bond strength

The bond strength of the coatings was assessed with an MST (CSM, Peseux, Switzerland). The MST provides four different methods of assessing layer adhesion:

1. Acoustic emission detection
2. Frictional force measurement
3. Penetration depth measurement
4. Optical observation via an attached microscope.

In this test, a hemispherical diamond Rockwell C stylus (50 μm tip radius) is moved along the surface under a linearly increasing load from 0.1 N to 30 N. The critical load L_c is the load when damage to the coating occurs. L_c values are determined by observations with an optical microscope using a calibrated sample positioner.

Coating adhesion was also qualitatively assessed by Rockwell C indentation according to CEN/TS/1071-8 standard using similar equipment to that used to assess the load carrying capacity. This procedure allows ranking the coatings based on image analysis after indentation at an applied load of 150 Kg.

3.1.8. Dry sand abrasion resistance

The dry abrasion resistance of the coatings was tested with the dry sand/rubber wheel abrasion test (ASTM G65 / procedure D-modified, 45 N, 2000 wheel revolutions, Shore 60A rubber wheel). Two samples of each coating type were tested. Prior to testing, sample surfaces were ground with a diamond wheel to produce a surface finish of about 0.2 to 0.3 μm . The sample volume loss due to testing was determined with an optical profilometer.

3.1.9. Wet sand abrasion resistance

The wet abrasion resistance of the coatings was measured with a wet sand/rubber wheel according to modified ASTM G105-02 procedure guidelines using a Falex sand abrasion test machine and controlled slurries. For each coating type, one rectangular shaped specimen (1" x 3" x 0.5") was submitted to a 5,000-cycle run under 22 N normal load and using a 7 foot diameter Shore A60 neoprene rubber wheel at a nominal speed of 245 rpm. The slurry mixture was composed of AFS 50/70 rounded quartz grain sand and deionized water in a ratio of 0.940 kg

water / 1.500 kg sand. Prior to testing, the sample surfaces were ground with a diamond wheel to produce a surface finish of about 0.2 to 0.3 μm . The test allowed ranking the coatings for resistance to penetration into the substrate. The wet abrasion rate was expressed as the mass loss (accuracy ± 0.1 mg) of the specimen.

3.1.10. Variable temperature galling resistance

Galling resistance was measured using a custom-designed, automated galling tester developed by Engineered Valve International Inc. (Glens Falls, USA) in collaboration with Velan (see Figure 3-2). The testing procedure consists in quarter-turn rotating an annular coated specimen (12.7 mm inside diameter x 31.7 mm outside diameter) against a second annular coated fixed specimen under controlled contact pressure, stroke motion, and temperature conditions. Contact load and stroke motion were respectively applied with a pneumatic thrust actuator (Samson 3277) and a quarter-turn actuator (Metso B1CU6/20L), and temperature was adjusted with a radiation furnace (Lindberg/Blue M Tube Furnace, Thermo Fisher Scientific Inc., Waltham, MA, USA) coupled with a Type K thermocouple probe tack welded onto one specimen. All test parameters were controlled from a centralized panel.

The coated surface of each specimen was prepared and inspected before testing. The coated surface preparation consists in manually polishing with several grades of polishing cloths (from P320 to P1200 grit) using a thin buffer solution containing commercial machinery oil. Specimens were selected to have a surface roughness R_a below 10 μin , flatness below 0.005 inch, and a mass of ± 0.5 mg. The test procedure was halted as soon as one coated specimen displayed a significant wear pattern (e.g., micro-welding, scoring). The test procedure was repeated for each coating type to allow ranking the materials in terms of galling resistance and total mass loss over a given period.

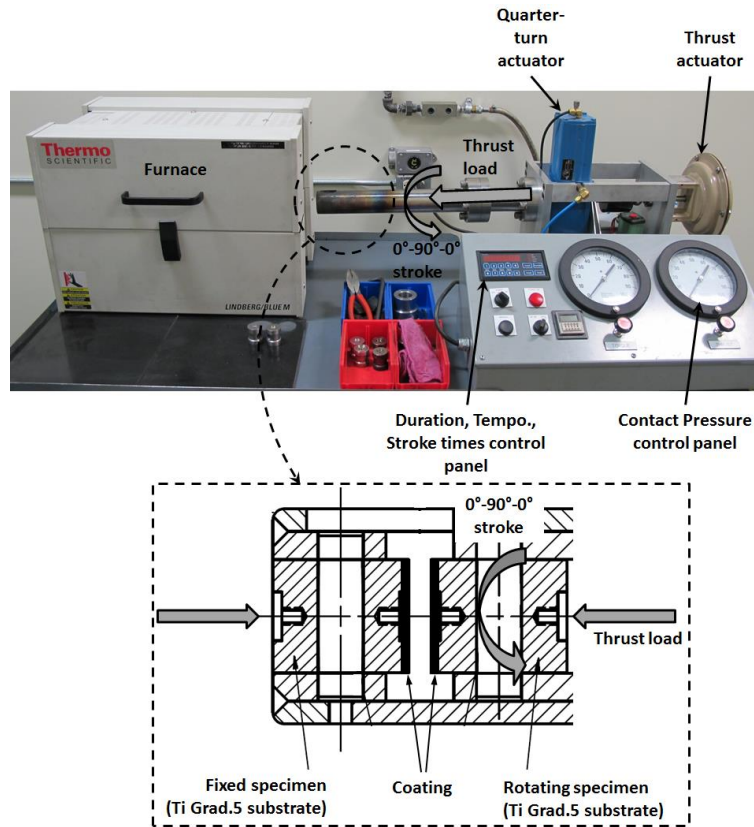


Figure 3-2: Custom-designed, automated variable temperature galling tester.

3.2. Structure and chemical composition

3.2.1. Scanning electron microscopy

Scanning electron microscopy (SEM) is an imaging technique in which the sample is scanned with an electron beam. The electrons that impact the material surfaces generate secondary electrons, back-scattered electrons, and X-rays. The X-rays are characteristic of the scanned materials, thus providing information on the material composition. In this thesis, SEM analyses were performed using JEOL JSM-840 SEM and Hitachi S4700 equipment.

3.2.2. X-ray diffraction

In X-ray diffraction (XRD), the material is exposed to an incident X-ray beam and gradually rotated to detect the diffraction angles θ_d , which are functions of the spacings d_d between the lattice planes, the wave length λ , and the crystal structure, as described by Bragg's law:

$$n_d \lambda = 2d_d \sin(\theta_d) \quad (12)$$

By comparing the XRD pattern of a material to patterns in a materials database, the crystallographic orientation of the material can be identified. The peak widths of the diffraction spectra are correlated with the grain size, which can be calculated using the Debye–Scherrer formula [169].

In this thesis, XRD measurements were performed on a Philips XPert-MPD X-ray diffractometer using Cu-K α radiation ($\lambda=1.54056 \text{ \AA}$) at 50 kV voltage and 40 mA current.

3.2.3. Crystallinity index

XRD was also used to measure powder, and as-sprayed, and aged coatings in order to estimate changes in crystallinity and other phase compositions and to determine amorphous content and the relative crystallinity index (I_c) [170]. XRD measurements were performed at angles ranging from 30° to 55° because peaks and amorphous humps are generally found within this range for Cr₃C₂-based coatings. The crystallinity index was estimated with the following formula:

$$I_c = \frac{\text{Sum of net peak areas}}{\text{Total net area}} * 100 \quad (13)$$

where net peak area = net area of the diffracted peak, and net area = net area of diffracted peaks + background area. Measurements were performed using a D8 Advance XRD diffractometer (Bruker Corp.) operating at CuK α , 40mA, and 40 kV.

3.3.Functional testing

3.3.1. Corrosion

Corrosion tests were performed in 3.5 wt.% NaCl aqueous solution using a three-electrode electrochemical cell with a standard calomel reference electrode and a graphite counter electrode. The coupon served as the working electrode. An Autolab PGSTAT302 potentiostat (Eco Chemie, Netherlands) equipped with a frequency response analyzer was used for the electrochemical measurements. Corrosion testing consists of first stabilizing the sample in the electrolyte for one hour, during which the open circuit potential (OCP) is monitored and recorded. Electrochemical impedance spectroscopy (EIS) is then performed at the determined

OCP with a 10 mV potential perturbation in the frequency range 10^5 Hz to 10^{-2} Hz. Finally, potentiodynamic polarization is performed starting at -200 mV potential (with reference to the OCP) and 1 mV/sec scan rate. The reversal potential is 1,600 mV maximum or when an anodic current density of 1 mA/cm^2 is reached, whichever occurs first.

3.3.2. Endurance cycle testing

Coatings endurance tests were conducted on prototype ball valves. An initial static test under full differential pressure condition (110% maximal working pressure) was performed to demonstrate the coating/substrate mechanical resistance and assess its load-carrying capacity. In a second step, prototype valves were overheated using superheated steam at either the maximum capacity of the steam generator or the maximum working temperature of the tested unit. Valves were then cycled under this severe tribo-corrosion condition. During the cycle test, valve torque and tightness levels were monitored over a number of cycles. The steam cycle test is considered to be highly abusive for coatings. High temperature removes lubrication films and generates thermal stress due to difference in thermal expansion rate; high differential pressure maximizes coating stress.

3.3.3. Aging test

Carbide reprecipitation (aging) process being suspected to take place on components exposed to temperature during service, an aging test was performed on as-sprayed coating coupons at a higher temperature in order to exacerbate the phenomena and to grow visible carbides. Several HVOF coated coupons were heated and maintained to 704°C (1300°F) using an electrical furnace. Samples were then removed from the furnace at different intervals (4 hours, 120 hours and 5,040 hours) and evaluated using SEM and XRD.

3.3.4. Thermal shock test

For the thermal shock test, coated samples were heated to 675°C during 30 minutes using a conventional electrical furnace. Samples were then quenched into room temperature water (20°C). Samples were visually inspected after each thermal cycle for defect using standard dye penetrant inspection methodology. The test procedure was stopped when one coated specimen

displayed significant a failure pattern (ex.: cracks or spallation). Repeating this test procedure for each coating type allows material ranking based on thermal shock resistance.

CHAPTER 4 ARTICLE 1: ALTERNATIVES FOR HARD CHROMIUM PLATING: NANOSTRUCTURED COATINGS FOR SEVERE-SERVICE VALVES

Article 1: Alternatives for hard chromium plating: Nanostructured coatings for severe-service valves

L. Vernhes^{a,b}, M. Azzi^{a,c}, J.E. Klemberg-Sapieha^{a,1}

^a *Department of Engineering Physics, Ecole Polytechnique, C.P. 6079, Succ. Centre Ville, Montreal, Quebec, Canada, H3C 3A7*

^b *Velan Inc., 7007 Côte de Liesse, Montreal, Quebec, Canada, H4T 1X8*

^c *Department of Mechanical Engineering, Notre Dame University, Zouk Mosbeh, Lebanon*

Abstract:

In this paper, a variety of chromium-free protective coatings were evaluated as alternatives for hard chromium (HC) electroplating for valve applications, such as nanostructured cobalt-phosphor (NCP) deposited by electroplating and tungsten/tungsten carbide (W/WC) prepared by chemical vapor deposition. A series of laboratory tests including hardness, micro scratch, pin-on-disk and electrochemical polarization measurements were performed in order to compare the performance of the different coatings. In addition, mechanical resistance and fatigue resistance were evaluated using prototype valves with coated ball under severe tribo-corrosion conditions. It was shown that W/WC coating exhibits superior resistance to wear and corrosion due to high hardness and high resistance to pitting, respectively while NCP exhibits better wear resistance than HC with alumina ball and low corrosion potential which allow to use it as protective (sacrificial) coating. Both nano-structured coatings exhibited attractive tribo-mechanical and functional characteristics compared to hard chromium.

4.1.Introduction

Hard chromium (HC) electroplating has been the most widely used technique for corrosion and wear protection applications for almost a century. It consists of depositing a layer of Cr onto

¹ Corresponding author. Tel.: +1 514 340 5747; fax: +1 514 340 3218; E-mail address: jsapieha@polymtl.ca (J.E. Klemberg-Sapieha).

metal components, using an electrolytic bath containing hexavalent chromium Cr^{6+} , which is known to be a human carcinogen. In 2007, the Restriction of Hazardous Substances Directive (RoHS) was issued, banning several toxic substances including Cr^{6+} , and HC electroplating has been classified by the U.S. Environmental Protection Agency (EPA) as an environmentally unfriendly process [71]. Those classifications have stimulated search for a cleaner alternative.

One of the primary applications of HC is to extend life of heavy equipment such as actuators and valves. In valve applications, materials can be exposed to high stresses in highly hostile environments. For example, in mining, large critical valves control a flow of slurry containing up to 80% solid particles mixed with sulphuric acid (H_2SO_4) at 300°C and 60 bars in order to recover metals from ore [85, 171]. In petroleum refineries, isolation valves work at 800°C in highly abrasive environment to crack long hydrocarbon molecules and produce valuable gasoline [172]. In power plants, automated valves modulate supercritical steam at 700°C and 300 bars in order to efficiently generate electricity [9]. These extreme conditions results in surface deterioration which is one of the main causes of possible valve failure.

HC is a well-established and economical solution to protect critical valves, thus rendering its replacement difficult. Fortunately, on a number of harsh services, Original Equipment Manufacturers (OEMs) have already switched to alternative coatings in order to endure severe conditions. Today, the three most popular alternatives to HC in the valve industry are: (i) weld overlay of Co#6 alloy (UNS R30006 – Stellite 6 ®) [173], (ii) thermally sprayed Cr_3C_2 -NiCr [174-178], and (iii) diffusion processes (ion-nitriding, boriding) [74, 179]. Those costly alternatives have found niches, but do not show a potential to fully replace HC across this field, mainly for economic reasons [66].

In this context, nanostructured vacuum-based coating techniques and Cr^{6+} -free plating have received considerable attention as environmentally-friendly cost-effective approaches to the replacement of HC [74]. Among coating materials that have been investigated are metals and alloys (Co, Ni, Cr) [39], nitrides (CrN , TiN , SiCN) [129, 180], carbides (WC , Cr_3C_2) [181], and nanocomposites (TiSiN , TiSiCN) [128, 130].

This study represents a comparative analysis of two nanostructured coatings as HC alternative, namely the electrodeposited nanostructured cobalt phosphor (NCP), and the chemical vapor deposited tungsten/tungsten carbide (W/WC). The former one is prepared by electroplating process using pulse current and the latter one is prepared by chemical vapor deposition using hexafluoride (WF_6) precursor. Based on data published by their respective suppliers (thickness, hardness and coefficient of friction), those two cost-effective off-the-shelf coatings have the potential to fully replace HC.

4.2.Experimental

4.2.1. Material

20mm x 20mm x 5mm square blocks of and 80 mm balls of AISI 316 Stainless Steel (SS) were used as substrate. NCP were deposited from a plating solution containing Co^{2+} and P^+ . Pulse current was used to control grain growth and grain size, as described by McRea & *al.* [108, 182, 183]. W/WC coatings were deposited by exposing the substrates to hot and pressurized tungsten hexafluoride (WF_6) gas combined with a small amount of carbon, which condensate on the substrate surface to produce nanostructured W/WC coatings based on standard thermal CVD process elaborated by Zhuk & *al.* [147, 184].

All coatings were about $50 \mu\text{m} \pm 5$ thick as requested by *Velan Inc.* company. Samples were prepared by individual coating suppliers in their own facility. HC were prepared by Les Placages Dumoulin, Terrebonne, Canada, NCP samples were provided by a North-American company who wants to remain anonymous, and W/WC coatings were deposited by Hardide, Oxfordshire, United Kingdom.

4.2.2. Characterization techniques

4.2.2.1. Microstructure

X-ray diffraction (XRD) measurements were carried out by a Philips XPert-MPD X-ray diffractometer using Cu-K α radiation ($\lambda=1.54056 \text{ \AA}$) under 50 kV voltage, and 40 mA current. EDS and SEM analyses were performed using JEOL JSM-840 SEM. Grain sizes were calculated using the Debye–Scherrer formula [169].

4.2.2.2. Tribo-mechanical properties

Nano-hardness, H_N , and reduced Young's modulus, E_r , were assessed using a triboindenter (Hysitron Inc.) equipped with a Berkovich pyramidal indenter tip. The maximum load used for evaluation of H_N and E_r was 10 mN. This apparatus is able to measure the load – unload curve vs. penetration depth with a 1 nm resolution. The H_N and E_r values are calculated according to the Oliver-Pharr method [167] and based on 100 measurements for each coating.

Micro-hardness (H_M) measurements were performed using a micro scratch tester (MST) from CSM equipped with a Vickers indenter using loads from 5 to 30N. The indent sizes were evaluated using an optical microscope. Ten indentations were performed on each sample.

Scratch hardness (H_S) was measured by the MST apparatus equipped with a hemispherical diamond Rockwell C stylus (50 μ m tip radius) with a constant 10N load. The scratch length in each case was 5 mm, and the sliding speed was kept constant at 6 mm/min. Three scratches were performed on each coating. The scratch widths have been measured at three positions on each scratch track using an optical microscope. H_S was calculated using the formula $H_S = \frac{8*F}{\pi *w^2}$ as described by Suresh and al. [168] where w is the scratch width (m) and F is the applied load (N).

Tribological properties of the coatings were evaluated using pin-on-disk instrument from CSM. Coatings were tested against three different counterparts, namely 6 mm-diameter alumina and Co#6 balls, and Co#6 1 mm diameter flat cylindrical indenter. The load of 6N was used for Pin-on-disc test leading to a significant wear volume without influencing the substrate. The sliding speed was 50 mm/s and the wear track radius was 5 mm. The sliding distance was adjusted to each test in order to reach a significant wear volume. For each of the coating type, a minimum of three measurements were performed. The Co#6 counterparts material were used to simulate the seat materials used in the valves.

After the wear test, wear tracks were inspected by a profilometer to determine the wear volume. The wear coefficient K was calculated using the formula $= \frac{V}{F*S}$, where V is the worn volume

(mm³), S is the sliding distance (m), and F is the load (N). SEM observations were performed to assess the wear mechanisms.

4.2.2.3. Corrosion properties

Corrosion tests were performed in 3.5 wt.% NaCl aqueous solution using a three-electrode-type cell. A Standard Calomel Electrode (SCE) and a graphite rod were used as reference and counter electrodes, respectively. A potentiostat Autolab PGSTAT302 (Echochemie) equipped with a frequency response analyzer was used for electrochemical measurements. The corrosion test consisted of stabilizing the electrodes in the electrolyte for one hour, during which the free corrosion potential (FCP) was monitored. Then, potentiodynamic polarization was performed, starting from 200 mV below the open circuit potential (OCP), in the cathodic zone, to a potential at which an anodic current density of 1 mA/cm² was reached, i.e. after pitting had been initiated. The corrosion current density, i_o , was found using the Tafel interpolation technique. The breakdown potential, E_b , was identified on the polarization curve as the potential at which an irreversible increase in the current took places, as a result of the breakdown of the passive layer.

4.2.2.4. Functional properties

Three prototype ball valves with 80 mm nominal diameter and 50 bar nominal pressure rating were assembled with three different coated SS316 balls. All prototypes were equipped with SS316 seats coated with a 1mm Co#6 overlayer. Prototypes were tested as per the following protocol:

Mechanical resistance test

Prototype valves (with an inside coated ball) were fully assembled, filled with water, and submitted to full differential pressure in close position during 10 min (110% maximal working pressure – 60 bars). Seat leakage was monitored at the beginning and at the end of the 10 min pressure test. Prototypes were then dismantled and visually inspected. Visible seat leakage or visible damage of coated surfaces (Scoring) were identified as unsuccessful test.

Steam cycle test

Prototype valves were connected to a 100 kW electrical boiler supplying superheated steam at 315°C and 40 bars. The steam cycle consists of opening and closing the valve using an automated pneumatic actuator, while continuously recording the resistive torque and monitoring seat leakage (in closed position). Control and data acquisition were realized via Labview®. Test bench was able to operate 24h a day, 7 days a week. Valves were cycled every 5 min (Open-to-Close and Close-to-Open) under the steam atmosphere. Six torque values were recorded for each cycle: the peak torque to start valve opening (break-to-open, BTO), the constant torque to move the valve from close to open (run-to-open, RTO), the peak torque to finalize valve opening (end-to-open, ETO), the peak torque to start valve closing (break-to-close, BTC), the constant torque to move the valve from open to close (run-to-close, RTC), and the peak torque to finalize valve closing (end-to-close, ETC).

The test was stopped when a seat leakage was observed. Based on *Velan's* experience, the steam cycle test is highly abusive for coatings, and it is more severe than conventional wear tests. High temperature removes lubrication films from the surfaces and generates stress due to a difference in the coefficients of thermal expansion between the coating and the substrate; high differential pressure maximizes stress in the coating and at the interface.

4.3. Results and discussion

In this section, we first present the microstructural and mechanical characteristics of the coatings, then we discuss their functional properties.

4.3.1. Microstructure

XRD patterns acquired from the three different coatings are shown in Figure 4-1. HC and W/WC coatings mainly consist of b.c.c. chromium and b.c.c tungsten, respectively, and NCP mainly consists of h.c.p cobalt. WC crystals are not visible in the W/WC patterns, probably because carbide crystals are too small to diffract and they are dispersed in the W matrix. As calculated

using the Debye–Scherrer formula [169] , the grain size of HC, NCP and W/WC are 10, 5 and 17 nm respectively.

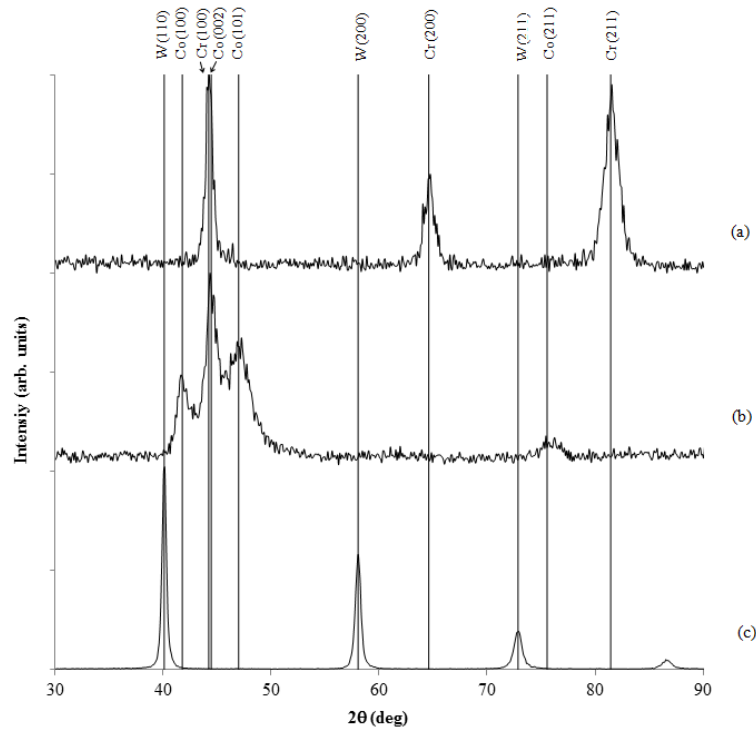


Figure 4-1: XRD patterns of (a) HC, (b) NCP, and (c) W/WC materials.

EDS spectra acquired from the three different coatings are shown in Figure 4-2. The chemical composition of each coating is confirmed. Carbon peak was detected on the W/WC EDS spectrum.

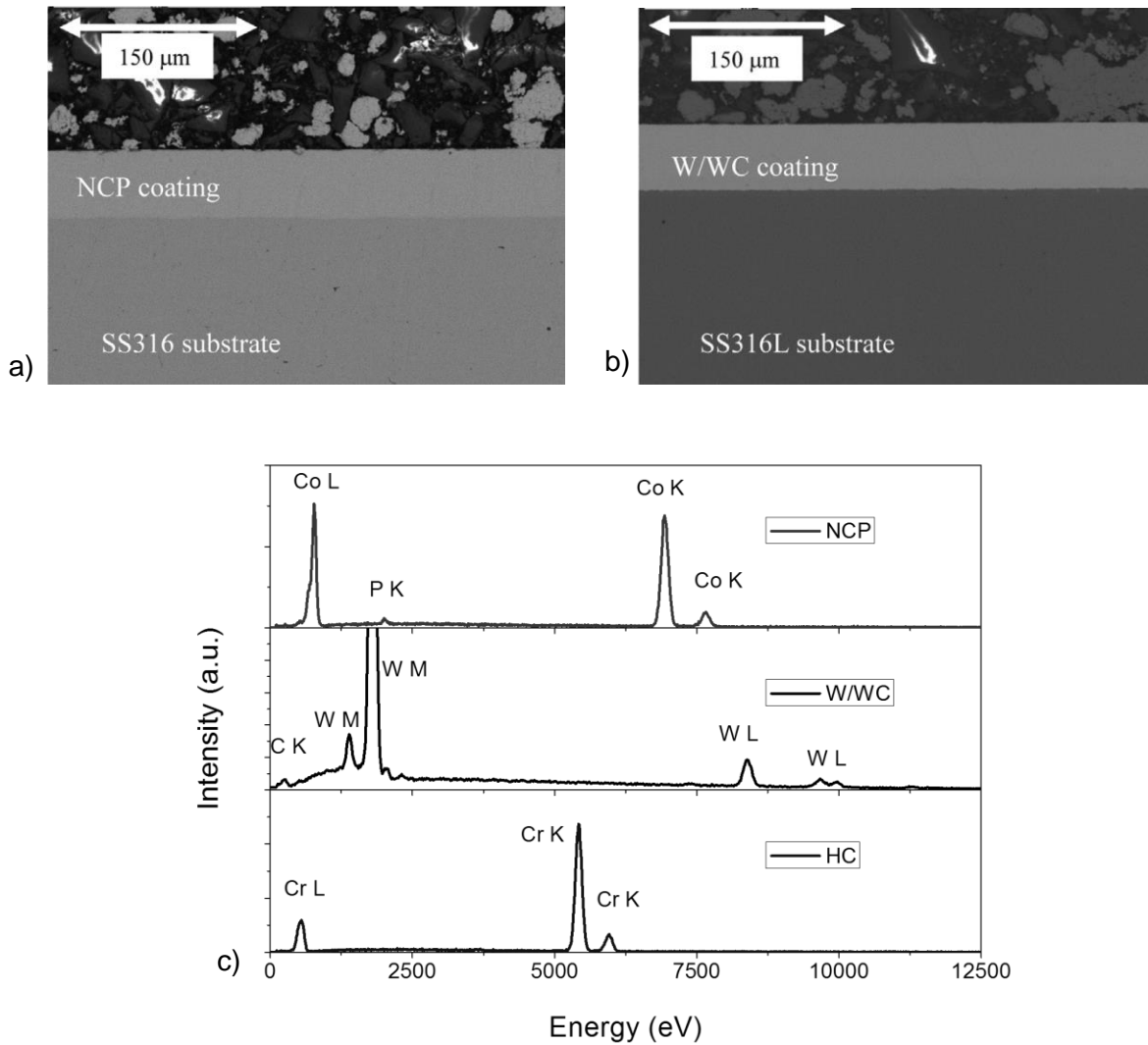


Figure 4-2: a) SEM images of NCP and W/WC cross section, b) EDS spectra of NCP, W/WC and HC materials.

4.3.2. Tribo-mechanical properties

Figure 4-3 (a) shows the results of the nanoindentation measurements. The W/WC coating possesses a H_N value of ~ 16.3 GPa and a $E_r \sim 280$ GPa while the NCP exhibits a lower H_N value of ~ 7.5 GPa and a $E_r \sim 160$ GPa. HC is in between with $H_N \sim 13$ GPa and $E_r \sim 230$ GPa. The H_M values obtained under several loads (5N, 10N, 15N and 30N) and H_S values for 10 N are presented in Figure (b).

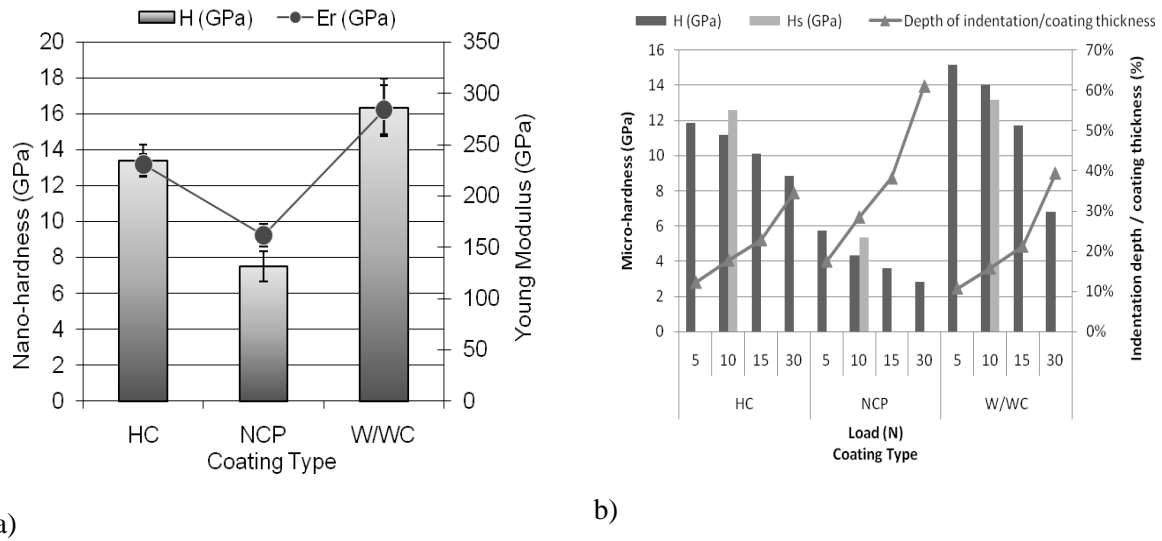


Figure 4-3: Nano-hardness and Young's modulus (a), Micro-hardness, Scratch-hardness at 10 N, and indentation depth/coating thickness as a function of load (b) for different coating types.

The hardness values for all coatings decreases with increasing the load. This correlates well with the increasing indentation depth/coating thickness ratio as shown in the same figure. This is attributed to an increased contribution from the substrate in the measurement with increasing load. It is clearly seen, that at ratio values as low as 10%, a good agreement between H_N and H_M values is obtained.

We can also observe a good agreement between H_S and H_M values for the different coatings. Delamination was not observed during the scratch testing, therefore results were not affected by adhesion failures. However, HC scratch mark exhibits regular cracks (See Figure 4-4 (a)). NCP & W/WC scratch marks are crack-free (Figure 4-4 (b)), which suggests a more ductile behavior than HC.

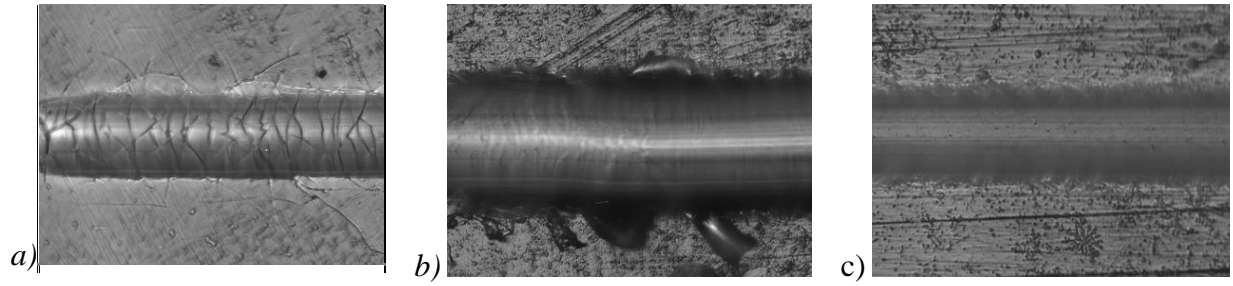


Figure 4-4: Scratch track at a 10N load for (a) HC, (b) NCP, (c) W/WC coatings.

Figure 4-5 shows the wear rate and friction coefficient for the different coating types using different counterfaces. A strong correlation between friction coefficients and wear rates was observed. Such relationship has been frequently documented in the literature [168].

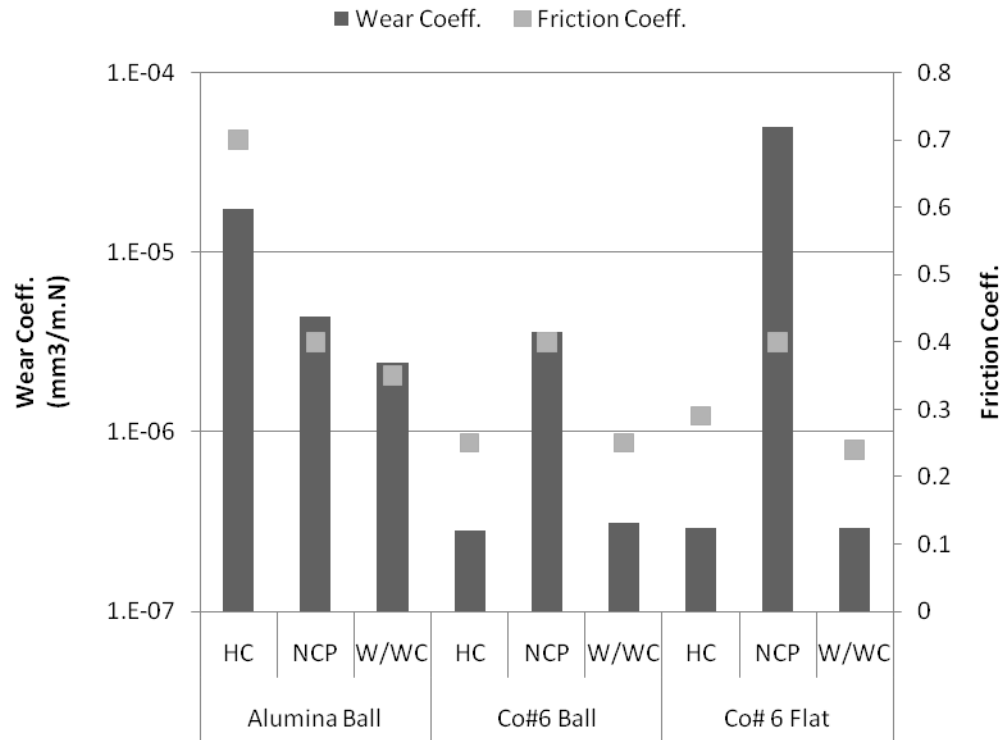


Figure 4-5: Wear rate and friction coefficient for different counterparts and different coating types.

HC wear mechanism

The HC coating exhibited the highest wear rate with alumina ball and the lowest when using Co#6 ball and flat indenters. With the Co#6 ball and Co#6 flat indenters the width of the wear track is smaller and the wear rate is reduced by a factor of 100. This difference is attributed to the hardness of the counterface; for a harder counterface (such as in the case of an alumina ball) brittle cracking mechanism takes place and high wear rate is observed. Figure 4-6 (a) shows the HC wear track after alumina ball wear testing. A limited number of sharp debris and cracks measuring around 30 μm are visible across the wear track. Based on SEM examinations, debris are the results of micro-crack propagation into HC.

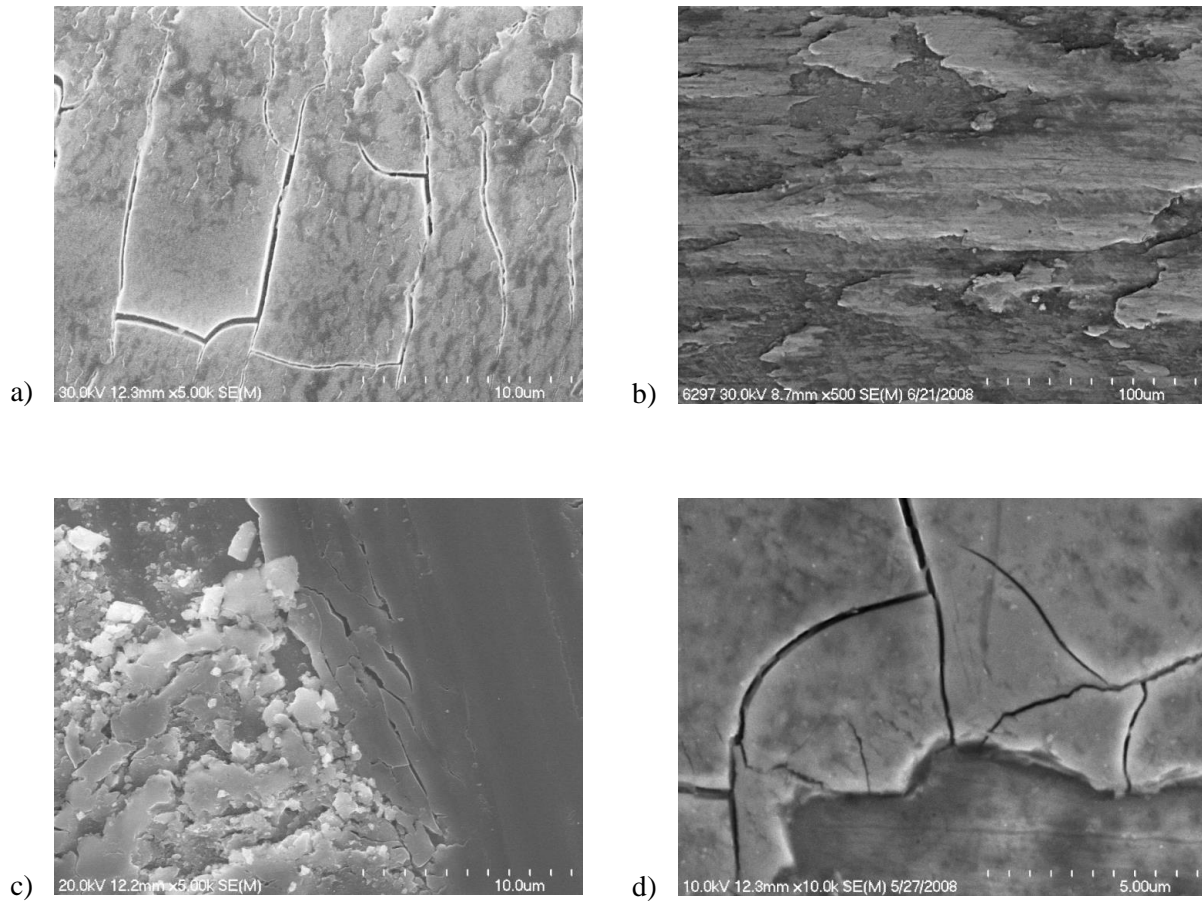


Figure 4-6: Micrographs of the wear track on a) HC with Al_2O_3 ball – 5kx, b) HC with Co # 6 ball – 500x, c) NCP with Al_2O_3 ball – 5kx, and d) W/WC with Al_2O_3 ball – 10kx.

HC wear track after Co#6 ball wear testing is shown on Figure 4-6 (b). Wear track shows the evidence of material transfer from the Co#6 indenter (tribolayer). SEM confirms HC coating integrity. A similar adhesive wear mechanism was observed with the Co#6 flat indenter, leading to low HC wear rate.

NCP wear mechanism

NCP exhibited similar wear rates when using alumina and Co#6 ball counterfaces. However a significant increase in the wear rate was observed when flat Co#6 counterface was used indicating higher susceptibility for edges (low resistance to scuffing). Figure 4-6 (c) shows a typical NCP wear track, with a large quantity of small debris (around 3 μm diameter round shaped) originating from NCP across the wear track. Similar to HC, near-surface cracking / delamination wear mechanisms were observed on NCP with all different indenters.

W/WC wear mechanism

W/WC shows 8 times lower wear rate and 4 times lower friction coefficient than HC when using alumina counterpart. With alumina ball, W/WC wear track exhibits micro-cracks but no formation of debris were observed (Figure 4-6 (c)). Micro-cracks around 10 μm long exhibit sharp edges. With Co#6 indenters, an adhesive wear mechanism similar to the one observed with HC, was visible. Material transfer from the indenter to the W/WC coating has been confirmed.

4.3.3. Corrosion properties

Figure 4-7 shows the polarization curves of the different coatings. Corrosion current (I_o), corrosion potential (E_{corr}), and breakdown potential (E_b), derived from these curves are summarized in Table 1.

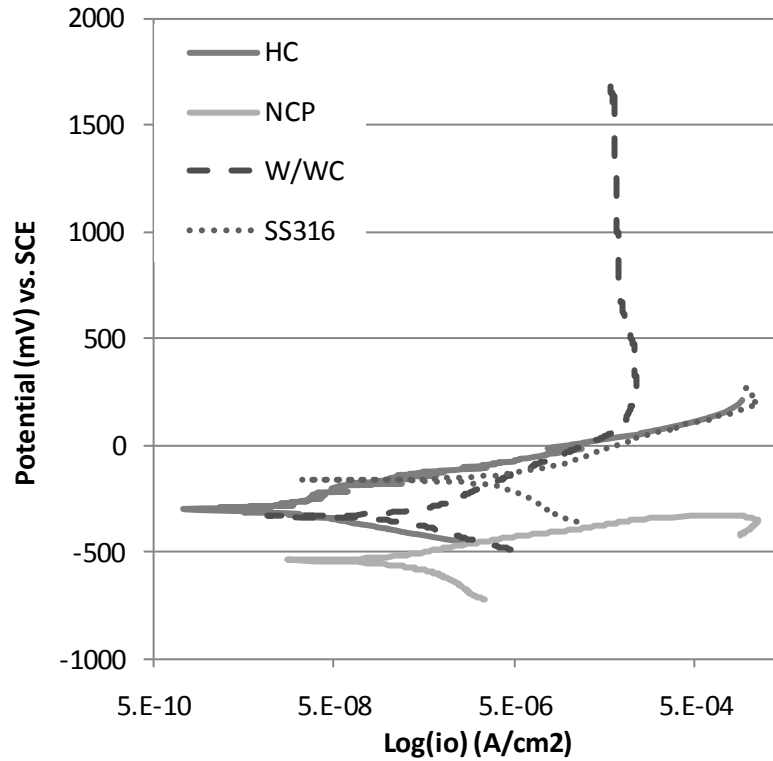


Figure 4-7: Potentiodynamic polarization curves of HC, NCP, W/WC and bare SS316 materials. NCP exhibited very low E_{corr} value compared to the other materials and has very low resistance to polarization due to the absence of a passivation layer.

Table 4.1: Corrosion parameters

Sample	Corrosion current, i_o (A/cm ²)	Corrosion potential, E_{corr} (mV)	Breakdown potential, E_b (mV)
HC	3×10^{-8}	-267	~80
NCP	3×10^{-7}	-530	< 0
W/WC	3.6×10^{-7}	-342	> 1750
SS316	1.0×10^{-7}	-224	~80

This coating acts as a sacrificial anode for the stainless steel substrate as confirmed by SEM observations of the surface after corrosion testing (see Figure 4-8 (a)).

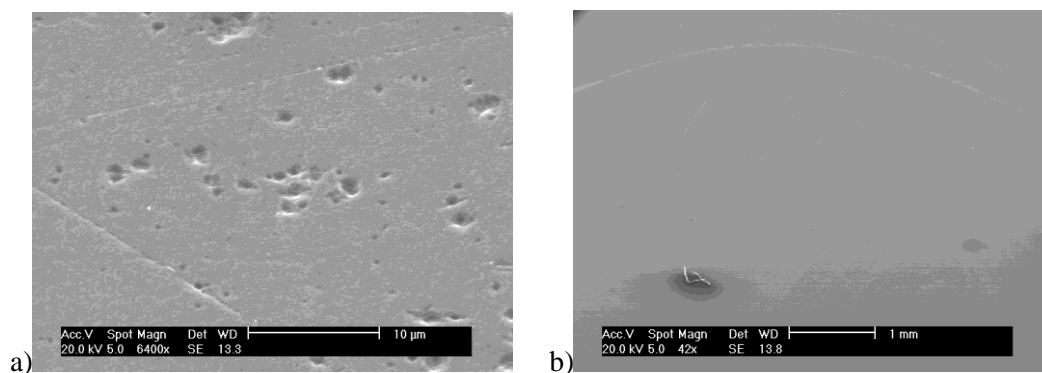


Figure 4-8: SEM images of (a) NCP and (b) W/WC coatings after corrosion testing.

The HC coating possesses similar properties as the bare substrate since both surfaces are passivated by chromium oxide containing layer. The W/WC coating exhibited a very high resistance to pitting with the passive zone extending to very high potential values. An SEM image of the W/WC surface after corrosion testing is shown in Figure 4-8 (b) confirming the absence of pits.

4.3.4. Functional properties

All coatings were tested in prototype valves having 80 mm nominal diameter and 50 bar nominal pressure rating. The coatings were tested under full differential pressure condition (110% maximal working pressure using water). This initial high pressure static test demonstrated sufficient load-carrying capacity for all 3 coatings with no damage observed after the test.

Prototype valves were then tested for fatigue resistance using superheated steam at 315 °C and maximum working pressure. During the test, valve torque and tightness were monitored over the cycles. After 3,000 mechanical cycles, the valve with HC coated ball started leaking. Visual inspection confirmed that the HC coating was damaged (Figure 4-9 (a)). An additional 7,000 cycles were performed with the NCP and W/WC coated valves with no leakage observed.

Figure 4-9 shows valve components after cycle test. In the case of HC, after 3,000 cycles, most of the damages were located on the ball cheek, whereas the NCP and the W/WC balls were in like-new condition. However, the matching Co #6 seats were significantly worn out for all three coatings.

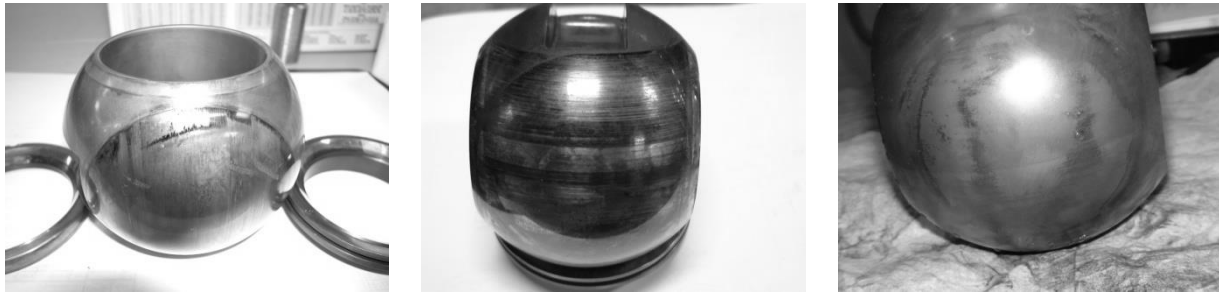


Figure 4-9: Images of valve components after the steam cycle test: (a) HC after 3,000 cycles, (b) NCP after 10,000 cycles, (c) W/WC coatings after 10,000 cycles.

Figure 4-10 shows torque evolution over cycles for HC. Similar torque evolution behavior was recorded for each coating. It is interesting to note that BTO increases from 250 N.m to 400 N.m for all the coating during the test when other torque values such as RTO or BTC remain almost constant. BTO increase is correlated with surface degradation of the Co # 6 seats.

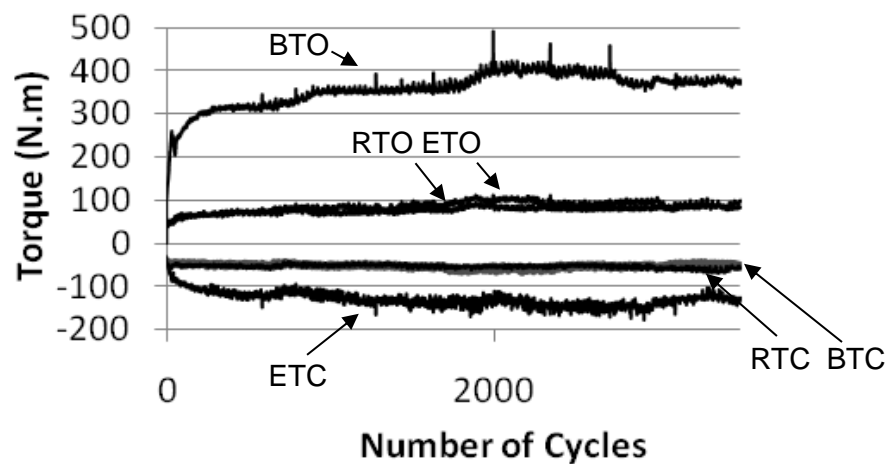


Figure 4-10: Steam cycle test results: Valve torque as a function of the number of cycles for HC coating.

4.4. Conclusions

In this paper, tungsten carbide deposited by CVD and cobalt phosphor deposited by pulsed electroplating nanostructured coatings have been characterized and systematically compared with hard chromium electroplating.

Both nanostructured coatings have exhibited attractive tribo-mechanical and functional characteristics compared to hard chromium. NCP offers a 4 times lower wear rate and a 3 times lower friction coefficient than standard HC plating when using alumina counterbody. However, NCP has shown to be more prone to corrosion with a break down potential < 0 volt and a limited resistance to scuffing. NCP should be used primarily for low stress contact in a relatively clean and non-corrosive service.

The W/WC offers a 8 times lower wear rate and a 4 times lower friction coefficient than hard chromium when using alumina counterbody. W/WC has also demonstrated a robust corrosion behavior with a break down potential > 1 volt. W/WC should provide good performance in slurry and corrosive service with various counter bodies.

4.5. Acknowledgements

The authors wish to thank Dr. Duanjie Li and Mr. Subhash Saini for their technical support and Professor Ludvik Martinu for useful discussion. We would also like to acknowledge Hardide for a fruitful technical exchange. Finally, we greatly appreciate *Velan's* interest and support of this research.

CHAPTER 5 ARTICLE 2: HVOF COATING CASE STUDY FOR POWER PLANT PROCESS CONTROL BALL VALVE APPLICATION.

Article 2: HVOF Coating Case Study for Power Plant Process Control Ball Valve Application

Luc Vernhes*
Velan, Montreal, Quebec, Canada
*E-mail: luc.vernhes@velan.com

David A. Lee
Kennametal Stellite™, Goshen, Indiana, USA

Dominique Poirier
National Research Council of Canada, Boucherville, Quebec, Canada

Duanjie Li, Jolanta E. Klemberg-Sapieha
Department of Engineering Physics, Polytechnique Montreal, Montreal, Quebec, Canada

Abstract

This case study is the result of an investigation on HVOF 80/20 Cr₃C₂-NiCr coating failure of on-off metal-seated ball valve (MSBV) used in supercritical steam lines in a power plant and solution. HVOF 80/20 Cr₃C₂-NiCr coating is used to protect thousands of MSBVs without incident. However, in this case the valves are challenged with exposure to rapid high pressure and temperature variation resulting in a unique situation where the coating experiences cracking and cohesive failure. It was found that carbide precipitation is a major factor causing embrittlement of the coating. Once the coating toughness and ductility is reduced, thermal, mechanical and residual stresses can initiate and propagate cracks more easily, causing coating failure when exposed to thermal shock. To alleviate those issues, possible coating alternatives were then evaluated.

5.1.Introduction

Valves are being used on drain and vent lines to extract large quantity of condensate during power station start-up in order to get dry superheated steam rapidly. During normal operation, drain and vent valves must remain steam-tight to prevent energy loss and maximize plant efficiency. For the last decade, metal-seated ball valves (MSBVs) have been the industry standard for this application, providing maintenance-free, tight, reliable shut-off. MSBVs in question are of a floating ball design with a fixed seat. Ball and seat are manufactured from forged Inconel® 718 PH and coated with a HVOF 80/20 Cr₃C₂-NiCr coating. The primary function of the HVOF coating is to increase the load-carrying capacity of the Inconel 718 surface². Indeed, it has been demonstrated that the deposition of such thick coating will not only reduce the wear rate but also distribute the peak stresses generated by localized loading from the surface to the base material and increase the galling threshold resistance (resistance to adhesive wear and material transfer) [166, 185]. 80/20 Cr₃C₂-NiCr coating composition is also specially adapted to resist to the high temperature, oxidizing conditions experienced by the valve [186, 187].

A major US-based power company had new challenges with their supercritical steam drain and vent lines in one of their plants. This particular fossil-fuel power station runs continuously from May to October due to high power demand to run air-conditioning systems. For the balance of the year, the plant only runs when the demand called for more power during peak usage times. Consequently the operation of the plant changed from base-load to peaking. Every time the plant shuts down or start-up, MSBVs are frequently operated and exposed to supercritical steam, going up to 15 MPa (2,200 psi) and 675 °C (1,250 °F) [9].

HVOF 80/20 Cr₃C₂-NiCr coating has failed after 1 year and less than 500 mechanical cycles in service on balls exposed to supercritical steam, with deterioration extending to regions where there is no contact between ball and seats. Coating was applied with a Diamond Jet® HVOF

² In this paper, load-carrying capacity refers to localized load as discussed by Holmberg *et al.* (Ref 2). This has to be distinguished from structural load-carrying capacity.

system using propylene as fuel. Visual examination of damaged components revealed minor frictional wear and typical stress/fatigue pattern (Figure 5-1).

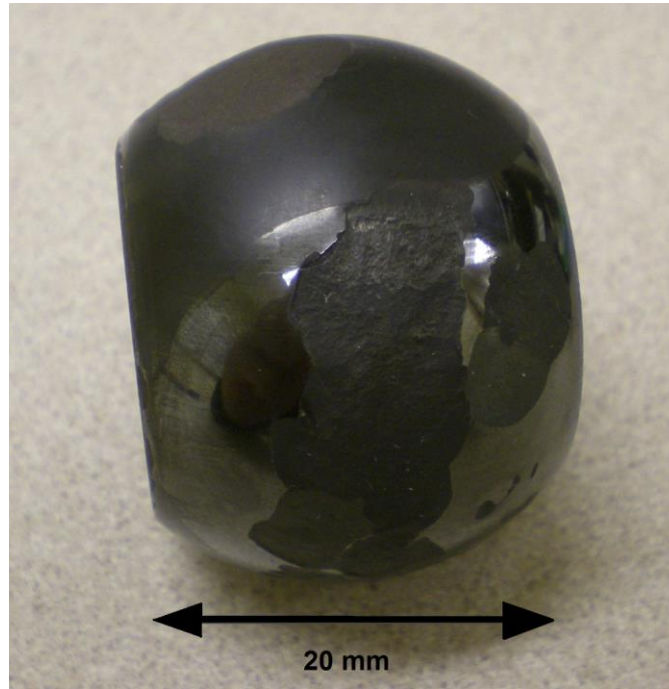


Figure 5-1: HVOF 80/20 Cr₃C₂-NiCr coating exhibiting cohesive failure after 1 year in service.

The intent of this failure analysis is to provide valuable information to understand failure mechanism and to help preventing this type of failure. The second objective of this study is to evaluate alternative coatings to alleviate those issues.

Section 2 describes the failure analysis, including experimental techniques, results and discussion. Section 3 presents test results of potential solutions. Section 4 concludes.

5.2.Failure analysis

The failure analysis was conducted by elimination. A list of potential failure mechanisms was established based on literature review and experience. Each potential failure mechanisms was investigated and eliminated as it was found not to apply:

1) Coating quality:

- High porosity level, allowing high pressure steam penetration
- Lack of bonding between coating and substrate,
- Lack of bonding between splats,
- Embedded grit,
- Residual stress (increase with thickness).

2) Design:

- Mechanical stresses during operation (excessive load),
- Thermal stresses due to thermal cycles or thermal shock.

3) Phase changes:

- Corrosion,
- Reaction at interface,
- Oxidation,
- Carbide precipitation.

The failure mechanisms have been attributed to either poor coating quality, improper ball valve design or coating phase changes. Regarding coating quality, grit embedded at the interface is known to substantially lower coating adhesion. Embedded grit can also result in corrosion problems [188]. Lack of bonding between coating and substrate results in a poor coating adhesion that can lead to premature coating spalling. Lack of bonding between splats results in a poor coating cohesive strength. Poor cohesion can lead to premature coating cracking and delamination [188]. The structure of thermal sprayed coatings, made of the piling up of splats, can produce significant interlamellar porosity. This porosity is usually associated with poorly melted particles that are trapped in the coatings. Porosity will not only decrease coating cohesive strength but can, if interconnected, acts as a path enabling corroding or oxidizing elements to penetrate within the coating, and eventually reach the base material [188]. Residual stresses are composed of quenching, cooling and peening stresses. They can limit coating adhesion and cohesion [188].

Failure mechanisms related to ball valve design were identified as mechanical stresses during operation (excessive load applied on the ball valve) or thermal stresses due to thermal cycles or

thermal shock. Thermal stresses are caused by restricting thermal expansion. They are primarily a function of the coefficient of thermal expansion (CTE) mismatch, the variation in temperature (ΔT) and the Young modulus of the coating (E_c). The following equation is often used to get an approximation of the thermal stresses generated in a coating upon change in temperature [164, 165]:

$$\sigma_{th} = E_c \Delta T (CTE_c - CTE_s) \quad (14)$$

It was also proposed that a chemical reaction at the coating/substrate interface could occur upon heating of the system. The species generated during such chemical reaction could be highly detrimental to coating performance and even lead to spallation. Oxidation of the Cr present in 80/20 Cr_3C_2 -NiCr coatings at high temperature is well documented as a coating degradation mechanism [189]. Carbide precipitation can occur due to the metastable nature of the thermal sprayed 80/20 Cr_3C_2 -NiCr coatings. During spraying, carbon is dissolved into the matrix. Carbon could come from two sources: I- chrome carbides are getting partially dissolved, creating a range of Cr composition in matrix from carbon-rich to the original Ni alloy (the higher the spraying temperature, the more dissolution occurring); II- carbon comes also from the carbon-rich propylene fuel. The high cooling rate “freezes” the carbon-rich matrix in a supersaturated state, with amorphous or nanocrystalline zones – a metastable system that can change if heated [190].

A series of experiments were performed in order to find the most dominant failure mechanism.

5.2.1. Experimental methodology

5.2.1.1. Coating quality characterization

SEM observation was used to compare a set of failed and new ball/seat. The interface between coating/substrate was qualitatively inspected by SEM observation. Coating thicknesses, porosity and oxidation levels were measured. Coating microstructures were observed using field emission SEM (S4700, Hitachi Instruments Inc., Tokyo, Japan) while porosity levels were evaluated from image analysis on ten images obtained with the backscattered mode of an SEM equipment (JSM-6100, JEOL, Tokyo, Japan). Coating hardness values were measured using a Vickers microhardness tester (Micromet II, Buehler, Lake Bluff, IL, USA) operating under a 300 gf load.

Nanohardness of coatings and of selected phases were evaluated using the Nano G200 from MTS/Nano Instruments (Oak Ridge, USA) with a Berkovitch tip under a load of 0.5 gf. The average micro and nano hardness values were obtained from ten and twenty indentations, respectively, performed on the cross section of the coatings. Objective lenses were used with the nano indenter when targeting specific phases. Otherwise, nano indentations were performed randomly to get the overall coating nano hardness (average of all phases).

5.2.1.2. Valve design

The second step was to perform two validation tests to confirm that valve design and materials were able to sustain localized load, wear and thermal shock. For the load-carrying capacity of the surface and wear resistance test, one prototype valve was assembled with brand new coated components and connected to a 100 kW electrical boiler supplying superheated steam at 426°C (800 °F) and 12.5 MPa (1,821 psig). The prototype valve was mechanically cycled using an automated pneumatic actuator, while monitoring seat leakage (in closed position). Valve was cycled every 2 minutes (open-to-close and close-to-open) under the steam atmosphere.

For the thermal shock test, new coated balls were heated to 675°C (1247°F) during 30 minutes using a conventional electrical furnace. Balls were then quenched into room temperature water (20°C – 68°F).

5.2.1.3. Phase changes

XRD measurements were performed on powder and on “as sprayed” and “aged” coatings in order to estimate the change in crystalline and other phase composition, amorphous content and to determine the relative Crystallinity index (I_c) [170]. I_c provides relative proportions of crystalline and amorphous phases. XRD measurements were performed between 30° deg and 55° deg range because peaks and amorphous hump are found within those values for Cr_3C_2 based coatings. Crystallinity index is estimated with the following formula:

$$I_c = \frac{\text{Sum of peak net areas}}{\text{Total Net Area}} * 100 \quad (15)$$

Measurements were performed using a D8 Advance Bruker AXS diffractometer (CuK α , 40mA and 40 kV). Spectrum areas were measured with Eva software.

5.2.1.4. Aging test

Carbide reprecipitation (aging) process being suspected to take place on components exposed to temperature during service, an aging test was performed on as-sprayed coating coupons at a higher temperature in order to exacerbate the phenomena and to grow visible carbides. Several HVOF coated coupons were heated and maintained to 704°C (1300°F) using an electrical furnace. Samples were then removed from the furnace at different intervals (4 hours, 120 hours and 5,040 hours) and evaluated using SEM and XRD.

5.2.2. Results

5.2.2.1. Coating quality characterization

SEM observations and hardness measurements on failed and new coatings were compared with the original equipment manufacturer (OEM) purchasing specification (See Table 5.1).

Table 5.1: Comparison of failed versus new HVOF 80/20 Cr₃C₂ + [80Ni-20Cr] coating and OEM specification.

	Failed Component	New component	OEM specification
Thickness (μm)	215	155 ± 35	200
Porosity	2%	2%	<3%
Oxide	<2%	<2%	N/A
Bond (MPa)	No failure	>70	>70
Microhardness (Vickers tip, 300 gf)	1092 ± 44	897 ± 69	>700

One of the observations of the failed coating was the significant increase in microhardness values from nominal 900 HV (300 gf) up to 1400 HV (300 gf). This led to evaluation of the phase changes that were thought responsible for coating microhardness increase [191, 192].

Grit used to roughen the surface prior to coating was observed at the coating interface with the substrate, but was not excessive and spallation of the coating was not contributed by this contamination as coating had remained bonded. The coating that had spalled had delaminated above the bond line within the coating. Cracks observed in the remaining coating did not appear to originate at the coating/substrate interface nor due to excess porosity. SEM also shows the presence of oxides (appears in dark gray on backscattered electron images – See Figure 5-2).

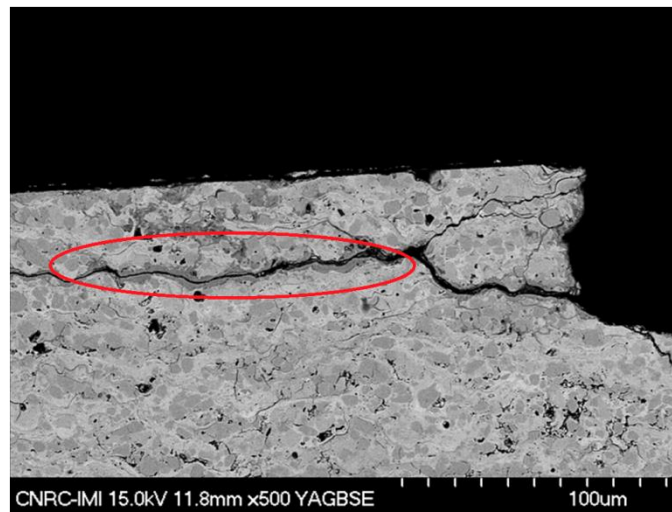


Figure 5-2: HVOF 80/20 Cr₃C₂-NiCr coating, sprayed with C₃H₆ after 1 year in the field.

Cracks formed and propagated across the coating matrix or at the carbide/matrix interface, delaminating layer by layer the coating (See Figure 5-3). Nanoindentation was used to measure the nanohardness of the oxide phase compared to the Cr₃C₂ phase and the overall coating nanohardness (See Table 5.2).

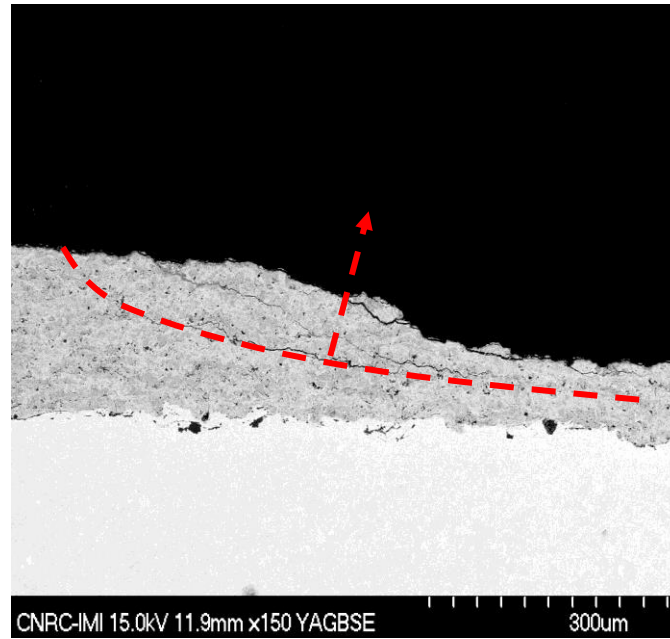


Figure 5-3: HVOF 80/20 Cr_3C_2 -NiCr coating, sprayed with C_3H_6 after 1 year in the field.

Table 5.2: Nanohardness of the oxide phase compared to the Cr_3C_2 phase and the overall coating nanohardness.

	<i>Nanohardness (GPa)</i>
New ball	15 ± 5
Damaged ball	18 ± 7
$\text{H}_{\text{Cr}_2\text{O}_3}$ - Damaged ball	12 ± 1
$\text{H}_{\text{Cr}_3\text{C}_2}$ - Damaged ball	~ 20

Only an approximated value was found for Cr_3C_2 due to the difficulty to target this specific phase during indentation. Among the different measurements, it appears that the oxide phase present in the coating shows the lowest hardness.

5.2.2.2. Valve design

The prototype valve was able to perform over 2,000 mechanical cycles with 0 seat leakages. After disassembly and visual inspection, neither indentation nor excessive wear were observed

on ball and seat surfaces confirming the load-carrying capacity of the surface and the acceptable wear resistance of the coating respectively.

On the other hand, after 30 consecutive thermal shocks going from 675°C to ambient temperatures, HVOF 80/20 Cr₃C₂-NiCr exhibited a crack network highlighting that the thermal shock resistance of the coated ball was not adequate (See Fig. Figure 5-4).



Figure 5-4: HVOF 80/20 Cr₃C₂-NiCr coating, sprayed with C₃H₆, after 30 thermal shocks going from ambient temperatures to 675°C.

5.2.2.3. Phase changes

Table 5.3 summarizes results and Figure 5-5 shows both XRD spectra. The crystallinity index has reduced by more than 35% after coating deposition, indicating the formation of amorphous phase and significant crystalline phase dissolution during spraying.

Table 5.3: Crystallinity Indices of powder, “as sprayed” and aged coating of the original HVOF coating

Powder composition	Fuel	Step	Crystallinity index
80% Cr ₃ C ₂ - 20% [80Ni20Cr]	C ₃ H ₆	Powder	77 %
		As sprayed	49 %
		4 hrs	67 %
		120 hrs	63 %
		5040 hrs	71 %

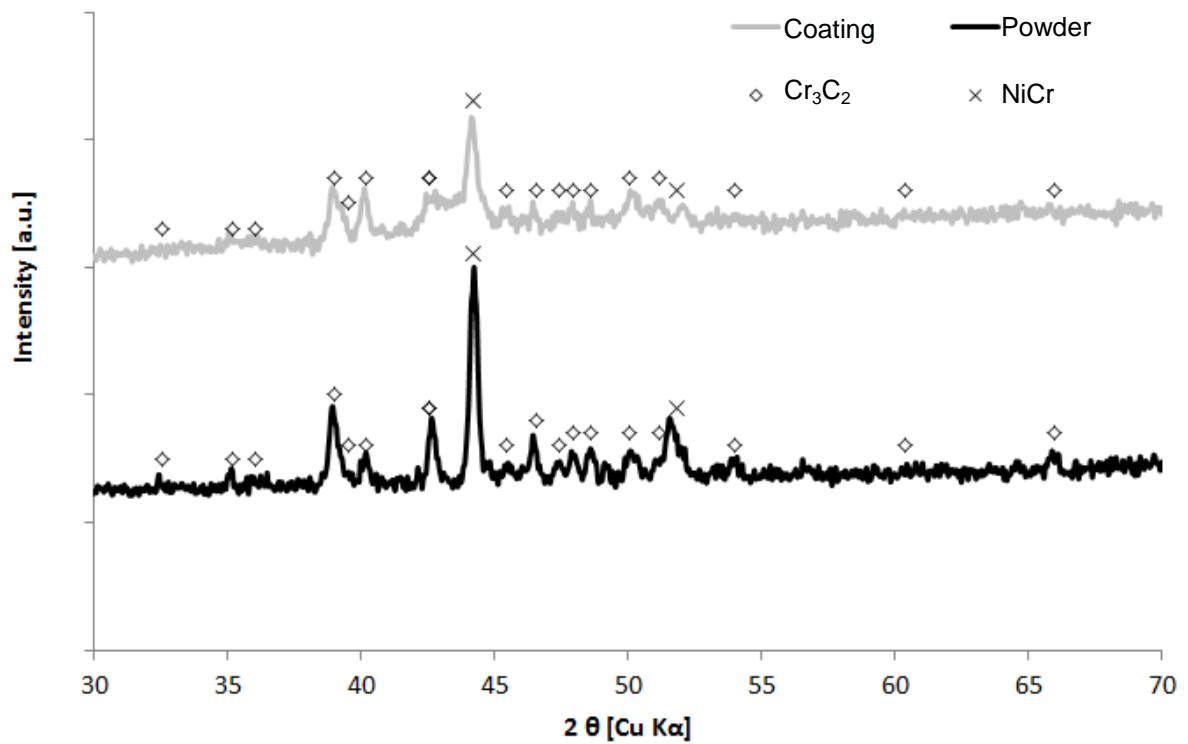


Figure 5-5: XRD spectrums of HVOF 80/20 Cr₃C₂-NiCr powder and coating, sprayed with C₃H₆. Cr₇C₃ and Cr₂₃C₆ phases, even though not shown on the graph, could also be present. Peaks overlapping has impeded their identification on all XRD spectrums presented in the paper.

5.2.2.4. Aging test

As shown on Figure 5-6, carbide precipitation was observed under SEM after 4 hour exposure to 704°C (1300°F). Coarsening of the carbide precipitates together with growth of the initial carbides occurs after 120 hour ageing.

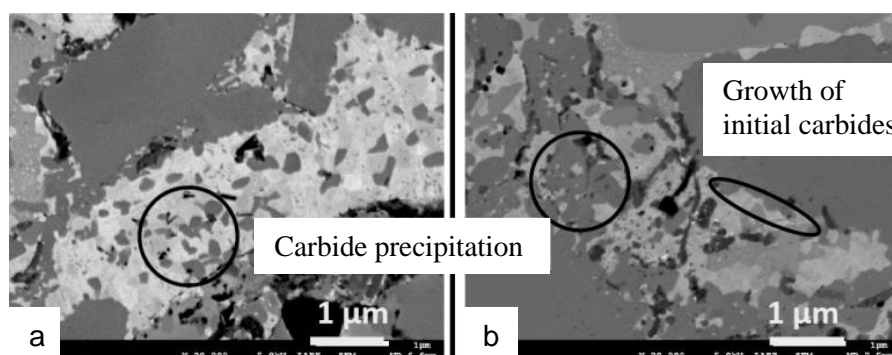


Figure 5-6: Microstructure evolution during aging test at 704°C (1300°F) after (a) 4 hour exposure; (b) 120 hour exposure.

XRD measurements were also performed on aged samples to estimate crystalline phase evolution during aging (See Figure 5-7). The following Table 5.2 summarizes results. Carbide precipitation and growth was detected using the XRD method. The coating crystallinity indices increase after 4 hours at 704 °C, reaching levels close to the initial powders (XRD peak sharpening due to recrystallisation and carbide precipitation). The indices plateau for longer ageing time.

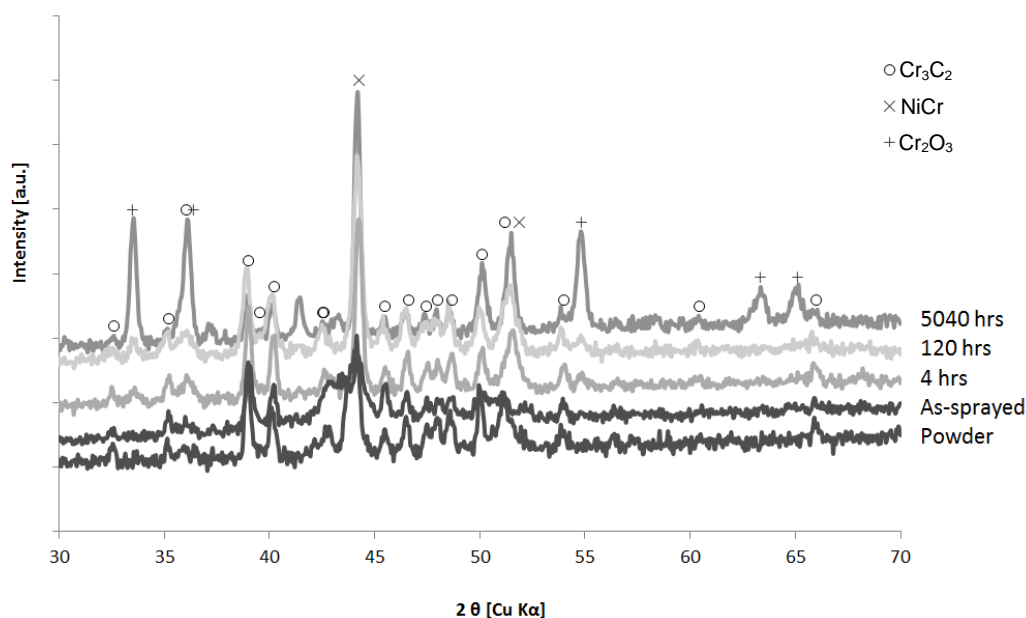


Figure 5-7: XRD spectrums of HVOF 80/20 Cr_3C_2 -NiCr powder, “as sprayed” and aged coatings, after 4 hour and 120 hour exposure to 704°C (1300°F) respectively.

5.2.3. Discussion

The main difference observed between failed versus new “as sprayed” coating is a 25% hardness increase, leading to measurements up to 1,400 HV and a decrease in thermal shock resistance. It was proposed that either carbide precipitation and / or oxidation could theoretically increase the hardness of the coatings and reduce its thermal shock resistance (aging). Thermal shock test results indicate that the CTE mismatch between HVOF 80/20 Cr_3C_2 -NiCr ($\sim 10 \times 10^{-6} / ^\circ\text{C}$) and the Inconel 718 base material ($\sim 15.5 \times 10^{-6} / ^\circ\text{C}$) leads to high thermal stresses [164]. After aging, thermal stresses generate cracks leading to coating failure. Therefore, the following two-step failure mechanism is suspected:

1) *Carbon dissolution into 80% Ni - 20% Cr binder during spraying :*

Carbide dissolution occurring during spraying has a significant influence on the properties of 80/20 Cr_3C_2 -NiCr coatings. For instance, plasma sprayed coatings typically present extensive carbide dissolution and formation of brittle carbides and oxy-carbides over HVOF or detonation gun spray processes due to the higher particle in-flight temperature and residence time [193]. This together with the higher porosity levels result in coatings with lower hardness displaying poorer performance in impact [194] and abrasion wear [195]. The nature of the feedstock

powder will also affect carbide degradation, and thus, performance of the coating [189]. Carbide dissolution has a key role in changing the binder hardness as well as the phases in presence. It also appears that the resulting supersaturation of the NiCr matrix makes this phase prone to brittle cracking.

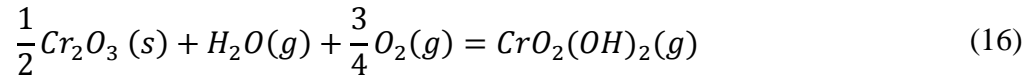
2.a) Chrome carbide precipitation:

In high temperature service, matrix recrystallisation can occur. The nucleation and growth of the carbide precipitates will depend on the heat treatment temperature and time but also on the spraying parameters. For instance, an extensive dissolution during spraying will favor precipitation in the form of agglomeration of nucleated carbides while with minimal dissolution, some growth around the retained carbides will preferentially occur [192]. While those microstructural changes would happen in service for the 80/20 Cr_3C_2 -NiCr coatings intended for high temperature applications, most of the studies replicate this condition by heat treating the coatings prior testing. It has been shown that carbide precipitation can improve coating wear resistance, adhesion and hardness [192, 196, 197]. Hardness increase could be observed with values exceeding the coating initial hardness due to carbide precipitation and to a “sintering” effect (decrease in porosity and improved adhesion between splats). The hardness increase could keep increasing due to the formation of a fine carbide network [192, 198].

2.b) Chrome Oxidation:

When sufficient Cr_3C_2 dissolution occurs during spraying to get at least 27.5% Cr in the matrix (either due to spraying conditions or the type of powder used), only Cr_2O_3 is formed in a continuous layer [196]. Cr_2O_3 can be adherent to the surface or eventually buckled if carbides are large. If there is not enough Cr in solution in the matrix, a NiO scale forms below which a continuous Cr_2O_3 scale develops. NiO can further be consumed to form NiCr_2O_4 [199].

Water vapor containing atmospheres cause more rapid oxidation of chromia-forming alloys than do dry oxygen or air, according to the equation shown below [200]:



In summary, two reactions involving Cr are competing: Cr can form carbides or can oxidize. At the temperatures of interest in this study, i.e. 675°C or below, Cr and C diffusion is slow and it is most probable that the Cr in contact with the oxidizing atmosphere will preferentially form oxides [196]. However, the Cr present deeper in the coating and not in contact with O₂ would form carbides.

In this specific case, oxides region displaying low hardness have been observed, possibly due to presence of pores and cracks, and perhaps the formation of non-stable oxides. Furthermore, no significant trend in hardness from coating top to bottom, where a gradient in oxide concentration is expected, was measured. Cr₂O₃ hardness being around 12 GPa and Cr₃C₂ hardness around 20 GPa, the precipitation of extra carbides seems a reasonable explanation for the increase in overall coating hardness.

No fine chrome carbides have been detected under SEM into the NiCr binder presumably due to very small crystals .

5.3.Solution

The next step was to test and qualify potential coating solutions, better suited to carry high load at elevated temperature and to withstand thermal shock.

Based on our analysis, the dominant failure mechanism is coating embrittlement due to chrome carbide precipitation in-service across coating binder which reduces coating thermal shock resistance. Three potential coating formulations were selected to overcome this issue.

The first candidate, coating #1, was a 75/25 Cr₃C₂-NiCr coating having a higher binder / carbide ratio compare to the standard in order to provide a slightly softer but tougher coating [164]. The second candidate, coating #2, was a coating with a chrome free binder in order to minimize the risk of carbide precipitation. To compensate for hardness reduction due to the lack of chromium, tungsten carbides were added to the chrome carbides. The third solution, coating #3, was a Ni

based fused and sintered coating having chemical composition closer to the base material and being fused at 1,000 °C to sinter, stress relieve and precipitate carbon. The CTE of Ni based fused and sintered coating ($\sim 16 \times 10^{-6} / ^\circ\text{C}$ vs $\sim 10 \times 10^{-6} / ^\circ\text{C}$ for 80/20 Cr_3C_2 -NiCr coatings) more closely matches that of Inconel ($\sim 15.5 \times 10^{-6} / ^\circ\text{C}$) [201]. Consequently, the Ni based fused and sintered coating induces less thermal stresses due to CTE mismatch than HVOF 80/20 Cr_3C_2 -NiCr when applied on Inconel.

To minimize carbon dissolution during spraying, hydrogen was used instead of propylene (carbon-free fuel) and Jet-Kote® HVOF system was used instead of Diamond Jet® (lower in-flight temperature). Table 5.4 summarizes the selected potential solutions.

Table 5.4: List of potential solutions

#	Chemical composition		Process	Nominal Thickness (μm)	Remark
	Powder	Fuel			
0	80% Cr_3C_2 20% [80Ni20Cr]	C_3H_6	HVOF	200	Original (Failed)
1	75% Cr_3C_2 25% [80Ni20Cr]	H_2		200	25% matrix to increase ductility
2	65-70% WC 22-25% Cr_3C_2 7% [Ni/NiCr]	H_2		200	Almost chrome-free binder to minimize Cr_3C_2 and Cr_3O_2 formation
3	55% Ni, 17% W, 15% Cr, 4% Si 3.5% Fe 3% B <1% C	H_2	Spray and Fuse	300	55% Ni to provide ductility. Fusing at 1,000 °C to sinter, stress relieve and precipitate carbon.

Brand new samples were produced with those three new coatings. A battery of tests was performed to assess their behavior for this specific application.

Valve Design: Load-carrying capacity of the surface and wear resistance of the three coatings were evaluated using the cycle test previously described. Coating #1 and #3 exhibited similar mechanical resistance than the original HVOF coating, as expected based on literature review [202]. Coating #2 demonstrated an exceptional mechanical resistance by performing 5 times

more mechanical cycles than the original coating without any leakage. The excellent wear behavior of HVOF (W,Cr)C-Ni in dry sliding condition is attributable to the presence of two hard phases: WC and (W,Cr)₂C. As studied by Berger et al., such a material combination results in an hardness over 1,200 HV (300 gf) [203] providing superior tribological performance at high temperature [204, 205].

Thermal stress resistance was evaluated using the thermal shock test previously described. Coating #1 exhibited a crack network relatively similar to the one observed on the failed valves after 60 thermal shock cycles. Coating #2 exhibited cracking and delamination after exposure to 675°C during 30 minutes As described by Hou et al., HVOF (W,Cr)C-Ni coating is able to well retained hard WC phase at higher temperature than WC but not as high as 80/20 Cr₃C₂-NiCr coatings and exhibits excellent oxidation resistance [206]. However, the relatively low CTE of WC compare to nickel-iron base superalloys substrate engenders high interfacial stresses at elevated temperature leading to delamination and crack formation as documented by Miller and Lowell [207] when on the other hand, the CTE of Cr₃C₂ is close to the one of nickel and iron [208]. Coating #3 successfully passed the thermal shock test (No crack indication after 60 thermal cycles – See Figure 5-8).



Figure 5-8: Coating #1 and #3 were repeatedly subjected to thermal shocks going from ambient temperatures to 675 °C. Then they were put through liquid penetrant tests to check for any cracking.

Phase changes: The third test was to perform XRD measurements on powder and “as sprayed” for the HVOF coatings in order to estimate crystalline phases dissolution during deposition. The fusing process allowing stress relieving and carbon precipitation, the Ic of coating #3 was not evaluated. The following Table 5.5 summarizes results.

Table 5.5: Crystallinity Indices of powder and “as sprayed” HVOF coating

Coating ID	Crystallinity index	
	Powder	Coating
0	77 %	49 %
1	80 %	51 %
2	83 %	82 %

While coating #1 displays similar degradation level than the original coating, coating #2 crystallinity index remains much higher, indicating less amorphisation (See Figure 5-9). However, for coating #2, a partial phase transformation ($WC \rightarrow W_2C$) was observed on the XRD spectra after deposition. Therefore, amorphisation is not the only degradation mechanism for this composition material.

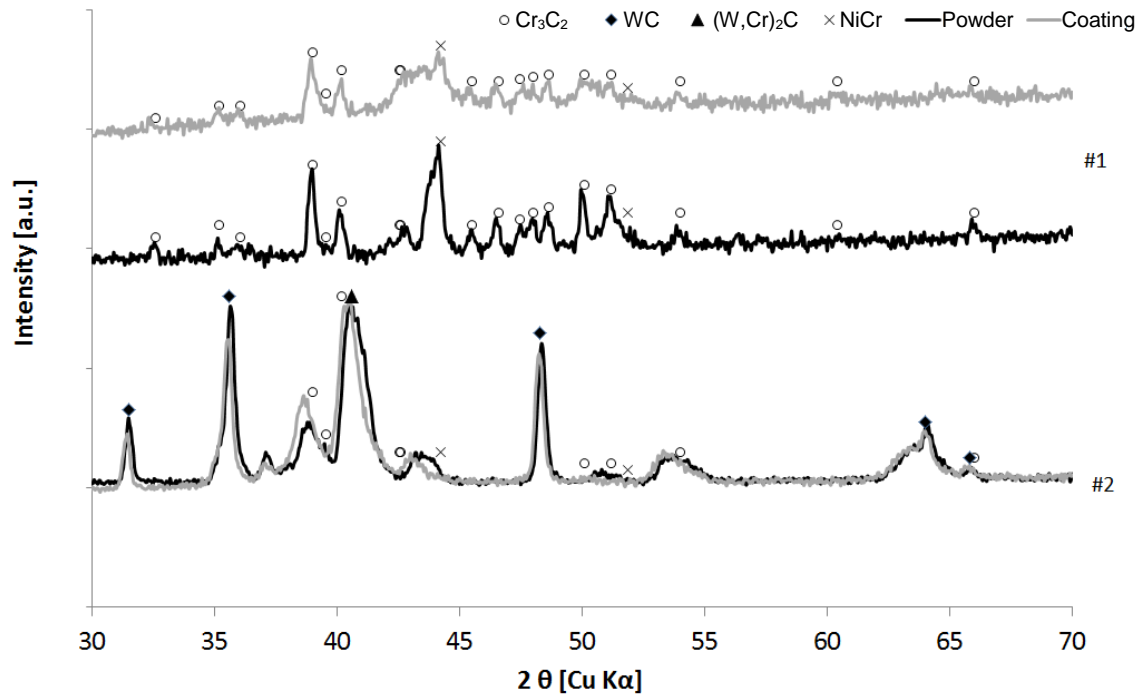


Figure 5-9: XRD spectrums of HVOF material #1 and #2; powder and “as sprayed” coating.

Based on those data, coating #3 appears well suited to withstand high bearing load and thermal shock. The coating #3 seems also the least sensitive to aging at high temperatures and therefore more durable under these very specific conditions.

Coating #2 is not suitable for temperature over 540 °C (1,000 °F). However, it has demonstrated the best overall performance at lower temperature.

5.4. Conclusion

In this study, the failure of a HVOF 80/20 Cr₃C₂-NiCr coating applied on a metal-seated ball valve (MSBV) used in supercritical steam line was investigated. While oxidation definitely contributes to coating degradation, it is believed that carbide precipitation is the major factor causing embrittlement of the coating. Once the coating toughness and ductility is reduced, thermal, mechanical and residual stresses can initiate and propagate cracks more easily, causing coating failure when exposed to thermal shock.

A spray-and-fuse NiWCrBSi coating more suitable to support high bearing load when facing thermal shock was qualified. This coating is less sensitive to aging at high temperatures and therefore more durable under these very specific conditions.

Using this technology, new valves were installed in the plant and have worked successfully for the past two years.

5.5. Acknowledgements

The authors wish to thank Mr. Subhash Saini (Velan), Michel Thibodeau (NRC) and Jimmy Sykes (NRC) for their technical support as well as Dr. Rogerio Lima (NRC) for useful discussion. We greatly appreciate Velan's interest and support of this research.

CHAPTER 6 ARTICLE 3: HYBRID Co-Cr / W-WC AND Ni-W-Cr-B / W-WC COATING SYSTEMS

Article 3: Hybrid Co-Cr/W-WC and Ni-W-Cr-B/W-WC Coating Systems

L. Vernhes^{a,b}, M. Azzi^{b,c}, E. Bousser^b, J.E. Klemberg-Sapieha^{b,3}

^a*Velan Inc., 7007 Côte de Liesse, Montreal, Canada*

^b*Department of Engineering Physics, Polytechnique Montreal, Montreal, Canada*

^c*Faculty of Engineering, Lebanese University, Roumieh, Lebanon*

Abstract:

The mechanical, tribological, and corrosion properties of two hybrid coating systems were assessed: 1) a tungsten–tungsten carbide (W-WC) top layer and a laser cladded cobalt–chromium (Co-Cr) interlayer (Stellite® 6 superalloy) applied to a 316 stainless steel substrate; and 2) the same W-WC top layer and an HVOF spray-and-fused Ni-W-Cr-B interlayer (Colmonoy® 88 superalloy) applied to an Inconel® 718 substrate. X-ray diffraction, energy dispersive spectroscopy, and scanning electron microscopy were used to analyze the microstructure of the coating layers. Microindentation was used to measure surface hardness and the hardness profile of the coating systems. Rockwell indentation was used to assess coating adhesion according to CEN/TS 1071-8. Surface load-carrying capacity was also assessed by measuring micro- and macrohardness at high loads. Tribological properties were assessed with a linear reciprocating ball-on-flat sliding wear test, and corrosion resistance was measured by potentiodynamic polarization and electrochemical impedance spectroscopy.

W-WC layers showed class I adhesion to both the SS 316 and Inconel 718 substrates, with and without an interlayer. Hardness profile measurements on cross section showed hardness of 13.6 GPa and 7.0 GPa for W-WC and Co-Cr, respectively, with average hardness of 9.7 GPa for Ni-W-Cr-B. Furthermore, hardness measurements at different high loads revealed that the addition of an interlayer increases surface hardness by up to 200% compared to the same coating system provided without an interlayer, quantifying the additional load-carrying capacity provided by the supplementary interlayer. The tribological measurements show that, except for the Inconel 718 / Ni-W-Cr-B / W-WC system, the hardest interlayer or substrate leads to the highest wear rates. In

³Corresponding author. Tel.: +1 514 340 5747; fax: +1 514 340 3218; E-mail address: jsapieha@polymtl.ca (J.E. Klemberg-Sapieha).

addition, the W-WC layer showed excellent corrosion protection, with no pitting observed after potentiodynamic polarization testing.

Keywords: *tribo-mechanical properties, load-carrying capacity, hybrid coating systems, corrosion resistance*

6.1. Introduction

Valves are vital equipment components that are used in the power, mining, and oil and gas industries, among others, to control the flow of materials, including liquids, gases, and slurries. Because valves are used in a wide variety of applications, surface solicitation and degradation mechanisms vary accordingly. Sealing surface degradation is a major cause of valve failure, and can result in two different failure modes: 1) the valve fails to cycle on demand due to excessive friction between the sealing surfaces; and 2) the valve performs a cycle on demand but fails to seal in closed position due to imperfections in the sealing surfaces. To extend in-service-life, valve sealing surfaces are typically hardfaced with wear-resistant superalloys such as Co-Cr (Stellite® 6) or Ni-W-Cr-B (Colmonoy® 88), which can withstand high pressures and temperatures.

Hardfacing is a technique whereby a wear- and corrosion-resistant alloy is welded onto a base metal to extend the life of components that are exposed to a harsh environment. Conventional hardfacings are applied by fusion welding to create metallurgically bonded pore-free coatings, which also provide the toughness required to withstand impacts and the rapid thermal cycling inherent in valve operation [209]. In addition to improving wear resistance, the elasto-plastic properties and thickness of fused hardfacings generally increase the strength and load-carrying capacity of the surface by acting as a solid bulk material and hence distributing stresses generated by high point load to the substrate [166]. Various processes have been developed to deposit metallurgically bonded hardfacings: low-heat-input processes such as diode laser cladding and spray-and-fuse are the leading techniques to produce pore-free overlays, as they minimize dilution with the base metal, which preserves grain structures while forming a metallurgical bond [210]. However, even when state-of-the-art deposition techniques are used, the tribological properties of hardfaced deposits remain inferior to those of hard thin films, and do not meet current valve industry needs [2].

CVD-deposited W-WC hard films have demonstrated excellent tribological properties by mitigating tribological phenomena such as adhesion and abrasion induced by wear debris [211]. However, as reported by several authors, thin film elasto-plastic properties, including modulus of elasticity, hardness, and strain to fracture, differ from those of conventional base materials used in the valve industry such as AISI 316 stainless steel (316) and Inconel® 718 (718) [212]. Mechanical property differences combined with limited thickness (typically in the range of a few micrometers) and a mismatch in the coefficient of thermal expansion produce peak stresses at the interface or within the substrate when subjected to high point load. This leads to permanent surface deformation and crack propagation [213]. For example, as described by Michler et al., a hard TiC:H thin film does not prevent high point-load indentation into stainless steel because the base material yields locally, which leads to permanent surface deformation, sometimes without thin-film fracture [214].

This failure mode is typically called brinelling for plastic indentation or eggshell effect when cracks and/or spallation occur, whereas the capacity of the surface to distribute stresses generated by high point loads to the substrate is called the surface load-carrying capacity [215]. The load-carrying capacity is therefore the capacity of a surface to distribute peak stresses generated by localized loading that do not exceed the yield strength of the thin film itself without developing permanent deformation, which includes brinelling (plastic deformation of the substrate without coating fracture), the eggshell effect (strain of the substrate up to coating fracture), and delamination (coating–substrate interface fracture) [159]. Although the load-carrying capacity can be controlled by adjusting the mechanical properties of the surface treatment, particularly thickness and modulus of elasticity, the mechanical properties of the subsurface materials also play a critical role in regulating stresses within the coating, base material, and interface. This also applies to the addition of interlayers that allow for gradual changes in the mechanical properties, thereby reducing the elasto-plastic gradient and peak stresses and hence preventing both brinelling and the eggshell effect [157]. Bemporad et al. used analytical modeling and experimental assessments to demonstrate the higher load-carrying capacity of PVD TiN thin film applied on Ti6Al4V substrates when provided with a HVOF WC-Co interlayer [213]. Bolleli et al. also reported the increased load-carrying capacity of DLC films deposited on aluminum and steel substrates when applied with a HVOF WC-CoCr interlayer [158, 216, 217].

The aim of this study was to characterize two coating systems composed of 1) a hard thin film top layer, which provides superior tribological properties, and 2) a hardfaced interlayer, which increases the load-carrying capacity by reducing the elasto-plastic gradient and peak stresses at the interface or within the substrate. The first coating system consists of a tungsten–tungsten carbide thin film (W-WC) deposited by chemical vapor deposition (CVD) onto a laser cladded Co-Cr hardfaced interlayer applied to 316 stainless steel substrate, and the second consists of the same W-WC top layer and a high velocity oxygen fuel (HVOF) sprayed and fused Ni-W-Cr-B hardfaced interlayer applied to a 718 substrate.

Section 2 describes the experimental procedures, including materials and characterization techniques. In section 3 presents the research findings and their analysis. In particular we will show that the addition of an interlayer increases the load-carrying capacity and that, except for the Inconel 718 / Ni-W-Cr-B / W-WC system, the hardest interlayer or substrate leads to the highest wear rates. Section 4 presents the conclusion.

6.2. Experimental

6.2.1. Materials

20mm x 20mm x 5mm square blocks of 316 and 718 annealed plates were used as substrates. Half the 316 samples were hardfaced with 2.5 mm thick Co-Cr alloy using a 4kW direct diode laser system (Coherent Inc.), and half the 718 samples were grit-blasted and HVOF coated (JP-5000) with 200 μm thick Ni-W-Cr-B alloy. The coated 718 samples were subsequently fused with an oxy-acetylene torch, providing a metallurgical bond (also called a diffusion bond) between the Ni-W-Cr-B splats and substrate while sintering the HVOF-deposited superalloy. All 718 samples were then age hardened at 790 °C for 8 hours and air cooled to increase the hardness, tensile strength, and yield strength of the 718 base material to a minimum of 4 GPa, 1,040 MPa, and 860 MPa, respectively. Prior to CVD, all samples were mechanically polished with 200, 600, and 1,200 grit SiC papers. After polishing, a 50 ± 5 μm thick nanostructured W-WC coating was deposited on all coupons the substrates were exposed to hot pressurized tungsten hexafluoride (WF₆) gas combined with a small amount of carbon, which condensed onto the substrate surface to produce a nanostructured W-WC coating, according to the standard thermal CVD process developed by Zhuk et al. [218]. Before mechanical, tribological, and corrosion testing, all samples were mechanically polished using 1,200 grit SiC papers to obtain a

smooth surface finish similar to valve sealing surfaces as well as measurement repeatability. Hardfacings were deposited by FW Gartner Thermal Spraying (Houston, TX, USA) and W-WC thin films were deposited by Hardide (Oxfordshire, United Kingdom). Figure 6-1 shows the schematics of the coupon configurations and Table 6.1 shows the nominal chemical composition and mechanical properties for all materials used.

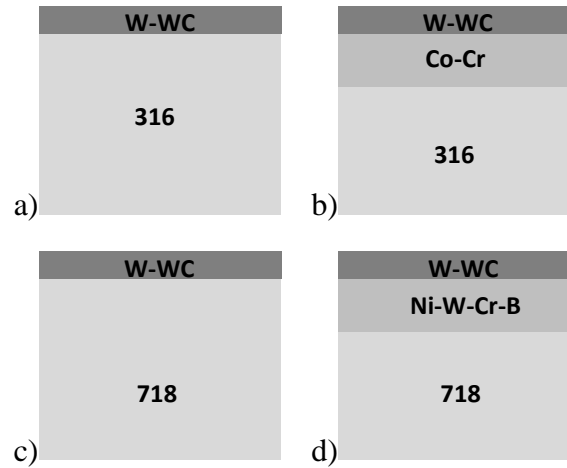


Figure 6-1: Schematic of sample configurations (a) 316 / W-WC, (b) 316 / Co-C / W-WC, (c) 718 / W-WC, and (d) 718 / Ni-W-Cr-B / W-WC.

Table 6.1: Chemical composition and physical properties.

Material	Thickness	E (GPa)	H (GPa)	Chemical Composition (% mass)
316	5 mm	156	2.25	18 Cr, 8 Ni, 2 Mo, Fe bal.
718	5 mm	175	4	18 Cr, 18 Fe, 5 Nb, Ni bal
Co-Cr	2.5 mm	209	5.5	30 Cr, 5 W, 1 C, Co bal.
Ni-W-Cr-B	200 μ m	208	8.5	17 W, 15 Cr, 4 Si, Ni bal
W-WC	50 μ m	280	15	< 1 WC, W bal.

6.2.2. Characterization methods

6.2.3. Microstructure

X-ray diffraction (XRD) measurements were performed with a Philips XPert-MPD X-ray diffractometer using Cu-K α radiation ($\lambda=1.54056 \text{ \AA}$) at 50 kV voltage and 40mA current in the standard Bragg–Brentano configuration to determine which crystalline phases are present in the sample. Scanning electron microscopy (SEM) and Energy-dispersive X-ray spectroscopy (EDS) analyses were performed using JEOL JSM-840 SEM to perform a visual inspection of the coating system, including porosity level, interlayer bonding, phase distribution, and coating system configuration as well as to confirm the chemical composition of the phases composing the microstructure of the material.

6.2.4. Tribo-mechanical properties

The adhesion of each coating system was qualitatively assessed by Rockwell C indentation according to CEN/TS/1071-8 standard. This procedure allows ranking the coatings based on image analysis of the fracture behavior of the coating after indentation at an applied load of 150 Kg.

Samples were sectioned with a coolant-assisted diamond wheel. Cross sections were then ground and polished using standard metallographic preparation procedures. Microhardness values of the constituent layers were measured on cross sections using a Micro-Combi Tester (CSM Instruments, Switzerland) with a Vickers indenter at 5 N load, a dwell time of 10 seconds, loading and unloading times of 30 seconds and calculated according to the Oliver and Pharr method [167].

The load-carrying capacity of each coating system was quantitatively assessed with visual surface hardness measurements using similar equipment at loads varying from 5 N to 30 N, dwell time of 30 seconds, and loading and unloading times of 30 seconds each. Macrohardness measurements were also performed using standard Rockwell equipment (manufacturer) at loads varying from 15 Kg to 150 Kg. All indent sizes were assessed using an optical microscope, including indents made by the Rockwell diamond stylus (120° cone angle, 200 μm radius). The corresponding hardness values were then calculated as the ratio between the load and the contact area estimated from the residual traces and the nominal indenter sizes. Eq. (17) was used for

Vickers indentations, Eq. (18) for Rockwell indentations showing a residual trace smaller than the projected area of the spherical tip (200 μm), and Eq. (19) for larger Rockwell indentations.

$$H = 2\cos(22^\circ) \frac{L}{d^2} \quad (17)$$

$$H = \frac{2L}{\pi D(D - \sqrt{D^2 - d^2})} \quad (18)$$

$$H = \frac{2L}{\pi(D^2 \left(1 - \frac{\sqrt{3}}{2}\right) + \frac{4d^2 - D^2}{2\sqrt{3}})} \quad (19)$$

where d is the average diameter of the residual traces (mm), L is the indentation load (N), and D is the nominal diameter of the Rockwell diamond indenter tip (400 μm).

Tribological properties of the coatings were measured using a ball-on-flat linear reciprocating tribometer (Tricomat, Montreal, Canada). Coating systems were tested for dry sliding wear resistance against 4.75 mm diameter Al_2O_3 balls using a sliding frequency of 2 Hz and stroke length of 10 mm. The load was set at 15 N to maximize stress within the coating systems without reaching delamination, and the total sliding distance was adjusted to 50 m to obtain a significant wear volume without piercing the top coating. After the ball-on-flat sliding test, the cross-sectional areas of wear tracks were measured with a Dektak 3030ST stylus profilometer (Veeco, Plainview, USA). The wear volume was calculated by multiplying the measured area by the track length. The wear coefficient K was calculated using the formula $K = \frac{V}{F \cdot S}$, where V is the worn volume (mm^3), S is the sliding distance (m), and F is the load (N). SEM observations were performed to assess the wear mechanisms.

6.2.5. Corrosion properties

Corrosion tests were performed in 3.5 wt.% NaCl aqueous solution using a three-electrode electrochemical cell with a standard calomel reference electrode and a graphite counter electrode. The coupon served as the working electrode. An Autolab PGSTAT302 potentiostat (EcoChemie, Netherlands) equipped with a frequency response analyzer was used for the electrochemical measurements. Corrosion testing consists of first stabilizing the sample in the electrolyte for one hour, during which the open circuit potential (OCP) is monitored and recorded. Electrochemical impedance spectroscopy (EIS) is then performed at the determined OCP with a 10 mV potential perturbation in the frequency range 105 Hz to 10^{-2} Hz. Finally,

potentiodynamic polarization is performed starting at -200 mV potential (with reference to the OCP) and 1 mV/sec scan rate. The reversal potential is 1,600 mV maximum, or when an anodic current density of 1 mA/cm² is reached, whichever occurs first.

6.3. Results and discussion

In this Section, we first present the microstructural and tribo-mechanical characteristics of the two coating systems, followed by their corrosion properties.

6.3.1. Microstructure

Figure 6-2 shows cross-sectional images of each sample arrangement. Figure 6-2b and Figure 6-2c show higher magnification of the Co-Cr and W-WC layers, respectively. Images of the two coating systems confirmed the thickness of each layer and their arrangement. All layers showed fairly dense structure and tight bonding with their respective substrate. The grains in the Co-Cr superalloy hardfacing have the typical dendritic shape that is formed during solidification and element segregation in the interdendritic region, whereas the Ni-W-Cr-B hardfacing showed a matrix containing 5 to 10 μm fine precipitated crystals.

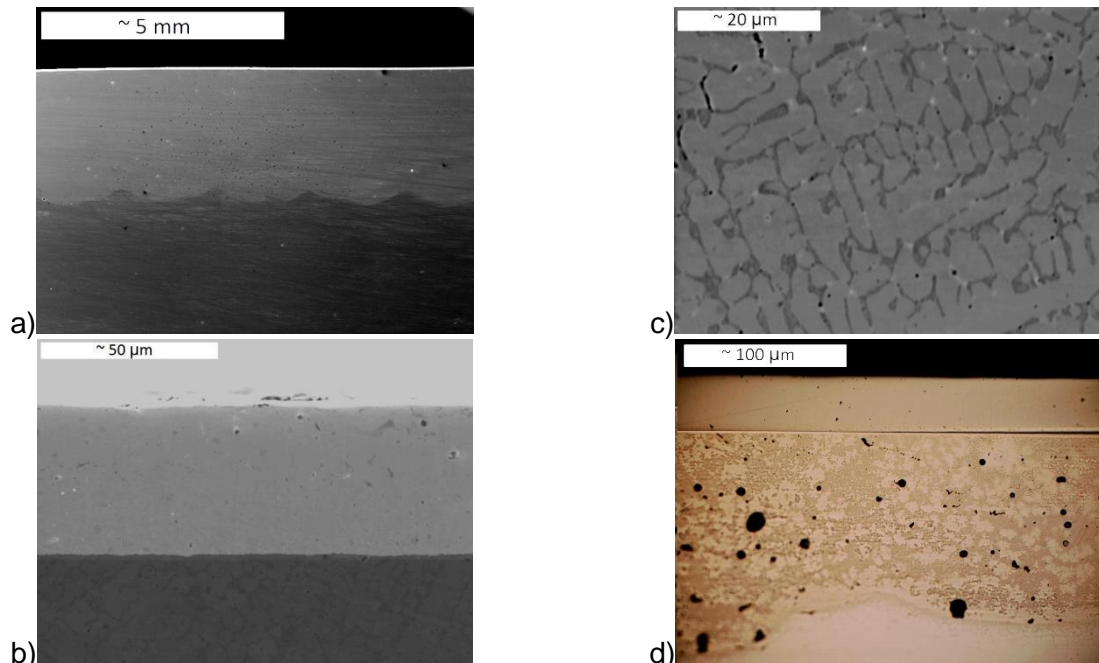


Figure 6-2: Cross section views of the coating systems a) 316 / Co-Cr / W-WC, b) Co-Cr / W-WC high magnification, c) Co-Cr high magnification, and d) 718 / Ni-W-Cr-B / W-WC.

Figure 6-3 shows XRD patterns acquired from the thin film and the two hardfacing materials. W-WC coatings consist primarily of bcc tungsten and WC crystals, which are not visible, probably because the carbide crystals are too small to diffract. XRD spectra revealed the presence of chromium and tungsten carbides in the composition of both superalloy hardfacings and the presence of tungsten and chromium borides in the Ni-W-Cr-B alloy.

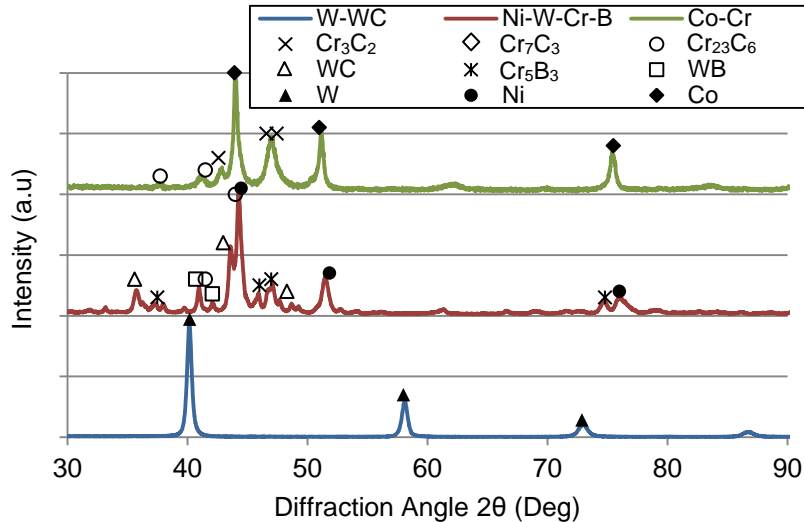


Figure 6-3: XRD spectra of the thin film and the two hardfacing materials.

Figure 6-4 shows the EDS spectra acquired from the three different coatings. EDS line scans performed on the Ni-W-Cr-B hardfacing revealed a Ni-Cr rich matrix containing W-rich and Cr-rich precipitates (Figure 6-4b). This concurs with the findings in the literature that precipitates also contain carbon and boron. These precipitates typically segregate during the solidification of Ni-W-Cr-B alloys and form the borides and carbides that are visible on the XRD spectrum [219]. Additional EDS line scans performed on Co-Cr showed that the dendrites are Co-rich and the interdendritic regions are Cr- and W-rich. As indicated in the literature, carbon segregates during the solidification of Co-Cr alloys and forms carbides in the interdendritic region. Therefore, although undetectable with EDS line scans, the chromium and tungsten carbides detected with XRD were assumed to be present in the interdendritic region [220].

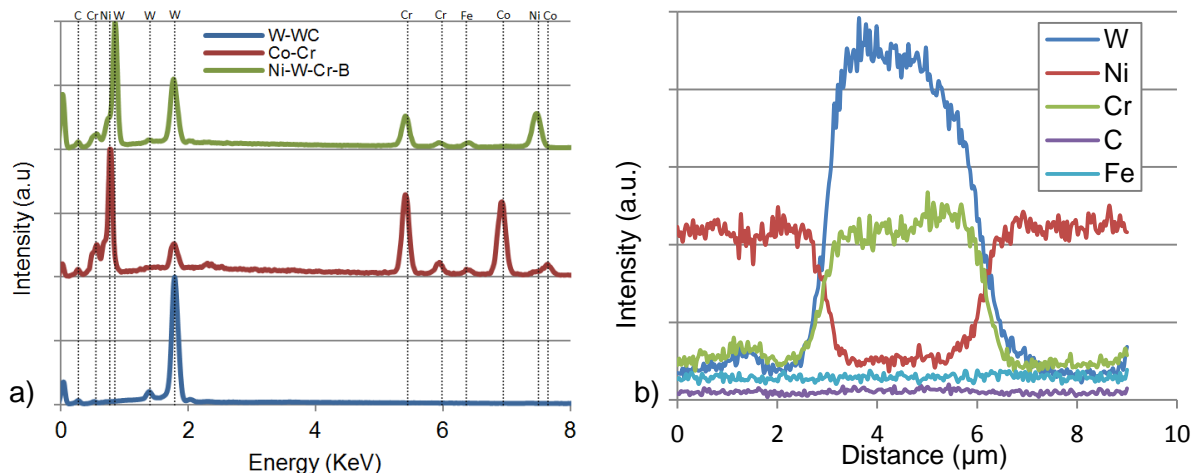


Figure 6-4: a) EDS spectra of the thin film and the two hardfacing materials, b) line scan across a precipitated crystal in the Ni-W-Cr-B interlayer.

6.3.2. Tribo-mechanical properties

Figure 6-5 shows the adhesion test results according to CEN/TS/1071-8 for the W-WC coating with and without an interlayer. None of the tested coupons showed spallation, indicating good bonding of the W-WC layer. According to standard classification, the W-WC adhesion is therefore considered Class 1 onto bare materials and with the use of an interlayer, even though cracks are more visible on the bare substrates than with the use of an interlayer.

Table 6.2 summarizes the cross-sectional microhardness values of the Co-Cr/W-WC and Ni-W-Cr-B/W-WC coating systems. Figure 6-6 illustrates the various indentations performed on the Ni-W-Cr-B alloy, the Ni-based matrix having a microhardness value around 6.5 GPa and the tungsten and chromium boride particles exhibiting a microhardness value around 13 GPa.

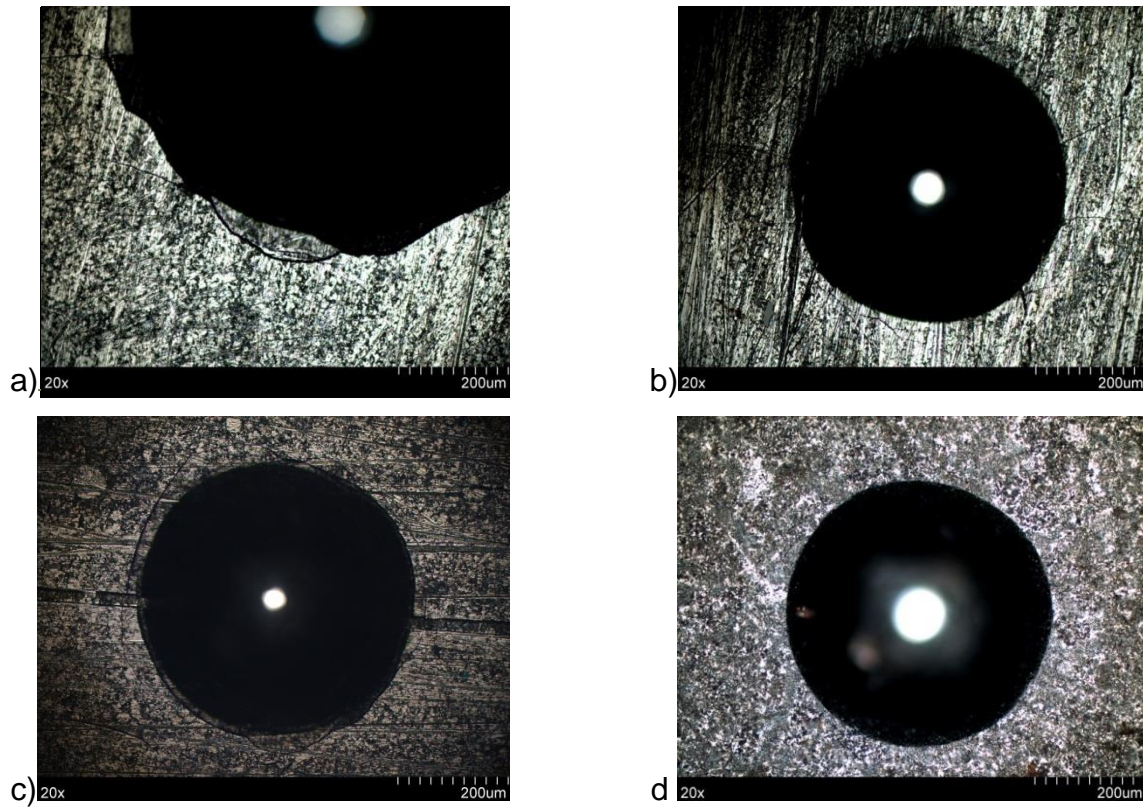


Figure 6-5: Adhesion using Rockwell C indentation according to CEN/TS/1071-8 standard for (a) 316 / W-WC, (b) 316 / Co-Cr / W-WC, (c) 718 / W-WC, and (d) 718 / Ni-W-Cr-B / W-WC coatings.

Table 6.2: Microhardness obtained on cross section.

Sample	H (GPa)	Standard deviation (GPa)	Maximum value (GPa)	Minimum value (GPa)
W-WC	13.6	0.6	14.5	13.1
Ni-W-Cr-B	9.7	2.3	13.3	6.7
Co-Cr	7.0	0.4	7.5	6.2
718	5.3	0.4	4.8	5.7
316	2.4	0.1	2.6	2.2

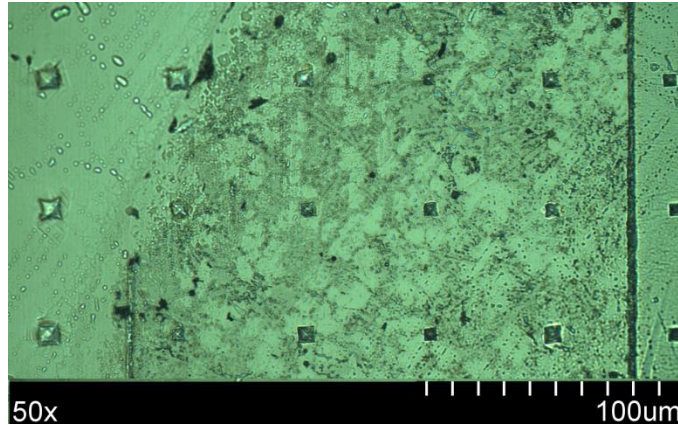


Figure 6-6: Cross section view of the microhardness measurements on 718 / Ni-W-Cr-B / W-WC.

Figure 6-7 shows the surface hardness measurements at loads varying from 5 N to 1471 N, indentations up to 30 N were performed using a Vickers indenter whereas indentations over 30 N were performed with standard Rockwell equipment. At low load, all hardness measurements are around 14 GPa, indicating no effect of the base material. At higher loads, the coating provided with an interlayer shows higher hardness than the coating without one, indicating higher load-carrying capacity. The addition of the Co-Cr interlayer increases the hardness of the coating system by 30%, from 7 GPa to 9 GPa when measured at 30 N, and the Ni-W-Cr-B interlayer applied on to 718 increases the hardness of the coating system by 15%, from 11.5 GPa to 13 GPa at the same high load when compared to the coating system without an interlayer. At the higher loads, the interlayer increases hardness by approximately 200% for the 316 / Co-Cr / W-WC and by 25% for the 718 / Ni-W-Cr-B / W-WC coating systems when compared to the coating system without an interlayer.

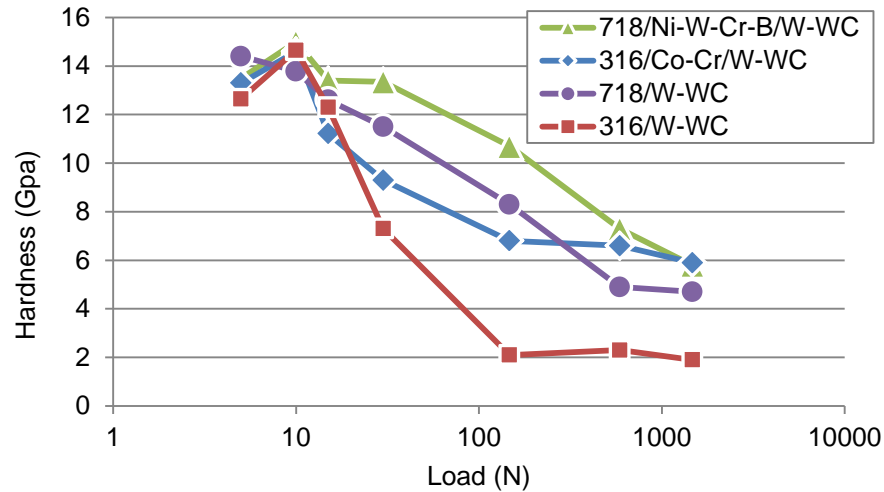


Figure 6-7: Hardness with load for the different coating systems.

Table 6.3 summarizes the results of the macrohardness readings obtained by the Rockwell equipment at different loads. Again, the W-WC coating applied with an interlayer shows systematically higher hardness, indicating higher load-carrying capacity. For example, at 15 Kg, the additional Co-Cr interlayer increases the hardness by 46%, from 58.7 HR15N to 85.9 HR15N, and the Ni-W-Cr-B interlayer applied to 718 increases the hardness by 7%, from 84.0HR15N to 89.9 HR15N. Because HR is proportional to indentation depth, the effect of the interlayer differs when expressed as contact pressure.

Table 6.3: Surface hardness measurements.

Sample	HRC (150 Kg)	HRA (60 Kg)	HR15N (15 Kg)	Vickers (2.5 Kg)
316 / W-WC	9.5	53.2	58.7	810
316 / Co-Cr / W-WC	49.9	76.0	85.9	1043
718 / W-WC	41.4	71.6	84.0	1027
718 / Ni-W-Cr-B / W-WC	45.8	77.1	89.9	1143

Figure 6-8 shows the wear rate and coefficient of friction for the different coating systems, illustrating the effect of the base material and the interlayers. The wear track profiles used to calculate the wear rates are shown in Figure 6-9.

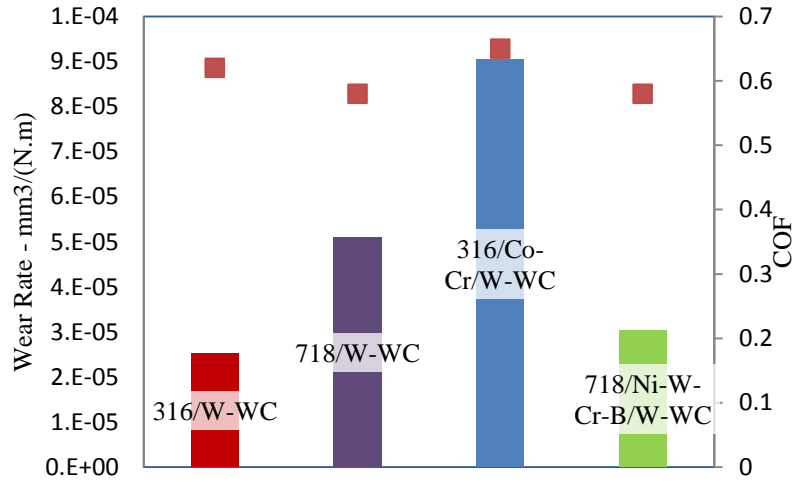


Figure 6-8: Wear rate (bars) and COF (dots) for each coating system.

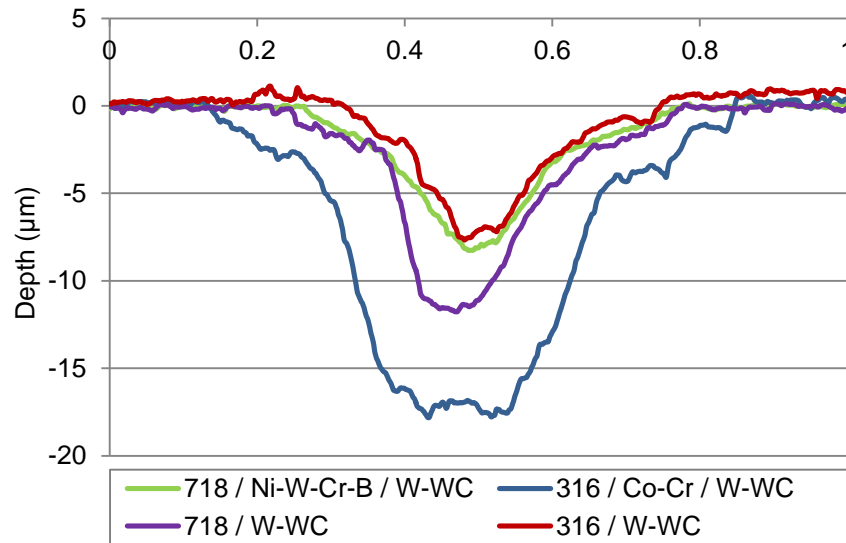


Figure 6-9: Wear track profile for each coating system.

All wear tracks show a relatively similar pattern, with 10 μm long micro-cracks but no formation of large flaking debris, as seen in Figure 6-10, indicating a mild steady-state abrasive wear mechanism.

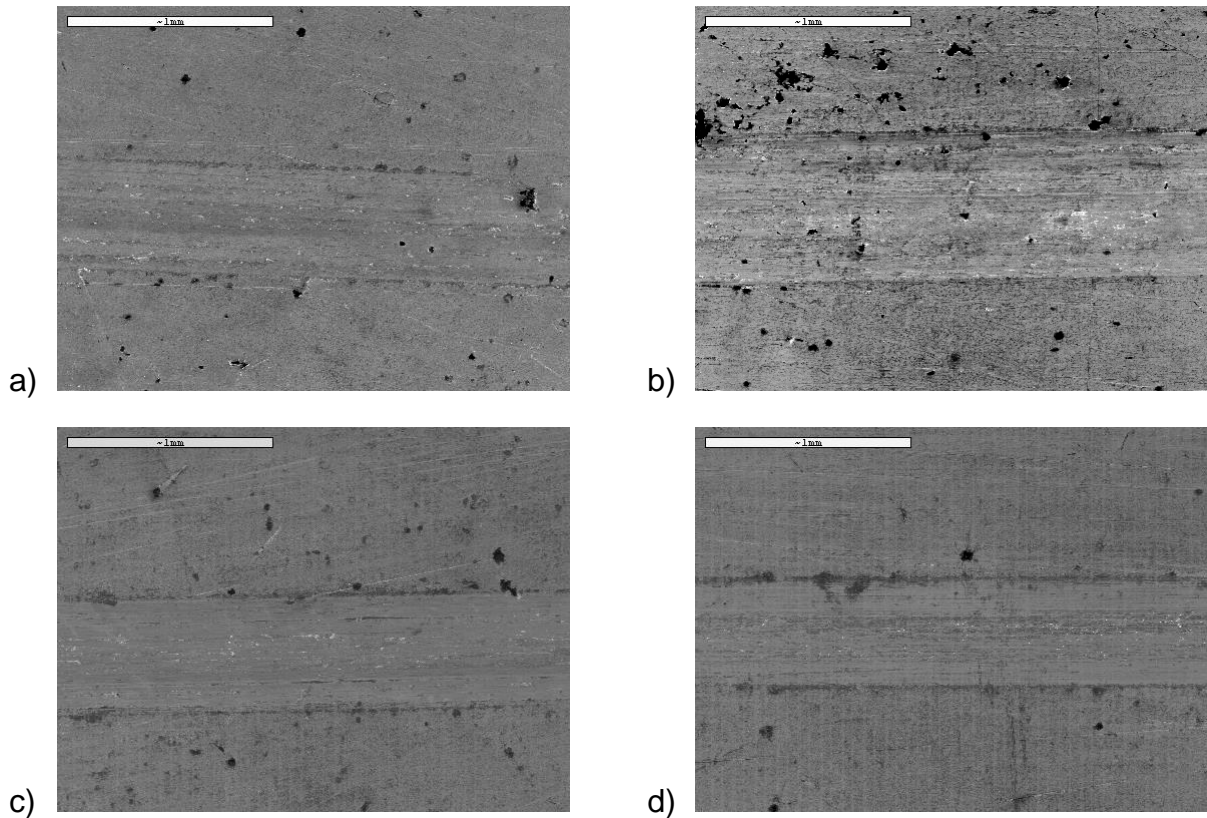


Figure 6-10: SEM images of wear tracks for (a) 316 / W-WC, (b) 316 / Co-Cr / W-WC, (c) 718 / W-WC, and (d) 718 / Ni-W-Cr-B / W-WC coatings.

This, combined with a similar coefficient of friction for all measurements, confirms that the results were not affected by adhesion failures. Insignificant traces of aluminum and oxygen were detected with EDS, indicating no significant material transfer from the Al_2O_3 counter body. The additional Co-Cr interlayer applied to 316 increases the wear rate by a factor of four, whereas the Ni-W-Cr-B interlayer applied to 718 reduces the wear rate by a factor of two. Thus, except for the 718 / Ni-W-Cr-B / W-WC system, wear rates are inversely proportional to the hardness of the substrate material carrying the thin film. Counterintuitively, the hardest interlayer or substrate leads to the highest wear rates, probably due to higher contact pressure for a given load. Results

suggest that the difference in wear rate is most probably due to a more uniform stress distribution under the Al_2O_3 ball rather than to a different wear mechanism. Because the modulus of elasticity of the base materials and interlayers are of the same order of magnitude, the authors suspect that the accommodation mechanism, that yields to a lower contact pressure, result from plastic deformations of the base and/or interlayer materials, which were insufficient to crack or delaminate the W-WC thin film.

The inconsistent behavior of the 718 / Ni-W-Cr-B / W-WC system may be attributed to the relatively low thickness of the Ni-W-Cr-B layer, which reduces its effect, as well as the composite nature of this interlayer. Despite the high average microhardness, the standard deviation of microhardness for this multiphase material indicates the presence of low hardness zones, which are the first to deform plastically, and which may enable an accommodation mechanism that is not directly proportional to hardness, as indicated by the low wear rate of this coating system.

It should be noted that when determining the maximum acceptable load for the ball-on-flat sliding test, it was observed that the 316 / Co-Cr / W-WC coupons delaminated systematically first. This premature delamination was most likely caused by a local phase transformation within the interlayer from face-centered cubic (fcc) to hexagonal close-packed (hcp). This stress-induced phase transformation occurs on Co-Cr superalloy hardfacing when subjected to high contact pressure, and forms a superficial nanoscale layer that acts as a solid lubricant and prevents galling [19]. When used as an interlayer, the stress-induced phase transformation most probably occurred beneath the W-WC thin film, dramatically reducing the interface shear strength and causing premature delamination of the thin film.

6.3.3. Corrosion properties

Figure 6-11 shows the OCP measurements of the substrates, overlays, and W-WC coating. All samples acquired a stable potential after 1 hour of immersion. Co-Cr shifted the potential of 316 to a more noble potential, whereas Ni-W-Cr-B shifted the potential of 718 to a more active potential. The W-WC coating showed lower OCP compared to the substrates and overlays, which is very important for corrosion protection because the substrates and overlays are

sacrificially protected by the coating in case of coating detachment or scratching and galvanic coupling between the W-WC coating and the substrate and overlay.

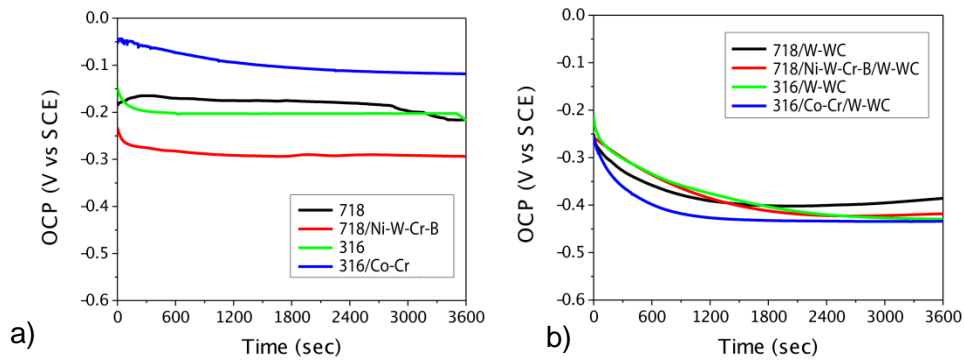


Figure 6-11: OCP measurements for a) substrate and hardfacings, and b) the four coating systems.

Figure 6-12 shows the EIS spectra of the substrates, overlays, and coating. EIS results are presented in Nyquist plots and are interpreted using the basic Randles electrical circuit, shown in the inset of Figure 6-12 a. The circuit consists of a resistor R_s in series with a constant phase element Q in parallel with a resistor R_p . R_s corresponds to the resistance of the test electrolyte between the working electrode and the reference electrode, and R_p is the polarization resistance, which represents the resistance to general corrosion. Q is a constant phase element (CPE), which is often used to replace a capacitor. Its impedance is expressed as:

$$Z_Q = 1/[Y_o(jw)^n]$$

where Y_o is the parameter of Q ($\text{F} \cdot \text{sec}^{n-1} \cdot \text{cm}^{-2}$), w is the angular frequency (Hz), and n is an empirical exponent, which is always situated between 0.5 and 1 [18]. When $n = 1$, the CPE describes an ideal capacitor with capacitance Y_o . For $0.5 < n < 1$, Q describes a non-ideal capacitor, and when $n = 0.5$, Q represents a Warburg impedance referred to as anomalous diffusion.

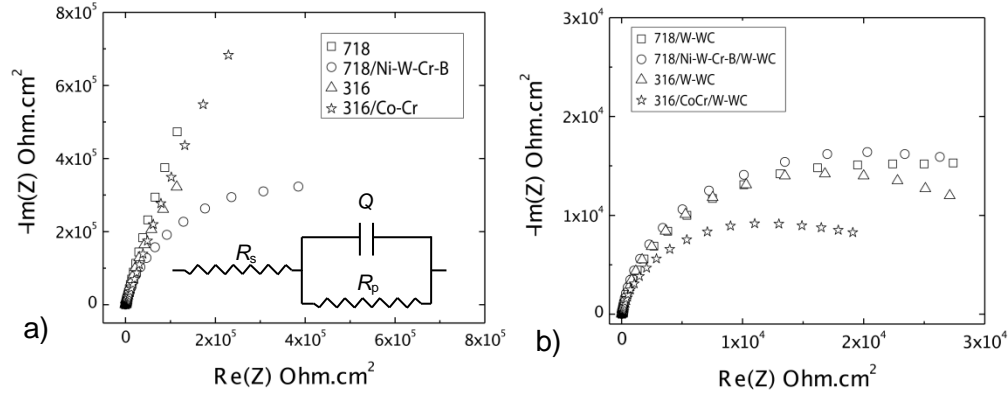


Figure 6-12: EIS spectra for a) substrate and hardfacings, and b) the four coating systems.

Co-Cr shows the highest impedance, with capacitive behavior at low frequencies as the phase angle approaches 90 degrees. Ni-W-Cr-B shows lower impedance, with a tendency towards more resistive behavior. W-WC significantly reduces the impedance of the substrates and overlays. All EIS spectra simulation data are shown Table 6.4.

Table 6.4: EIS spectra simulation results.

Sample	R_s ($\Omega \cdot \text{cm}^2$)	Q (Y_o) (F/cm^2)	Q (n)	R_p ($\Omega \cdot \text{cm}^2$)
316	29	0.33×10^{-4}	0.89	1.95×10^6
316/Co-Cr	28	0.13×10^{-4}	0.85	6.56×10^6
718	33	0.23×10^{-4}	0.90	4.21×10^6
718/Ni-W-Cr-B	32	0.15×10^{-4}	0.89	0.75×10^6
316/W-WC	35	0.14×10^{-3}	0.92	3.3×10^4
316/Co-Cr/W-WC	37	0.15×10^{-3}	0.89	2.2×10^4
718/W-WC	28	0.14×10^{-3}	0.90	3.5×10^4
718/Ni-W-Cr-B/W-WC	31	0.15×10^{-3}	0.90	0.8×10^4

R_s values are similar because the same solution was used for all tests. Co-Cr showed the highest R_p , indicating the highest resistance to general corrosion among the tested substrates and overlays. Co-Cr improved the corrosion resistance of the 316 substrate by almost three times. However, Ni-W-Cr-B decreased the corrosion resistance of the 718 substrate by almost five times.

The results obtained on all W-WC samples were almost identical, indicating no effect of the underlying layers on the corrosion performance of W-WC. The results show that R_p values were approximately two orders of magnitude lower compared to the substrates and overlays,

indicating lower resistance to general corrosion. Figure 6-13 shows the potentiodynamic polarization curves of the substrates, overlays, and W-WC coating. The corrosion current i_o and the breakdown potential E_b derived from these curves are presented in Table 6.5.

Table 6.5: Corrosion current i_o and breakdown potential E_b for each coating system

Sample	i_o (A/cm ²)	E_b (mV)
316 / W-WC	2.1×10^{-6}	N/A
316 / Co-Cr / W-WC	2.4×10^{-6}	N/A
718 / W-WC	2.6×10^{-6}	N/A
718 / Ni-W-Cr-B / W-WC	2.2×10^{-6}	N/A

718 shows high E_b and low i_o , indicating high resistance to general and localized corrosion while the Ni-W-Cr-B overlay significantly reduced the corrosion resistance of 718. In contrast, the Co-Cr overlay improved the corrosion resistance of the 316 substrate by decreasing i_o and increasing E_b .

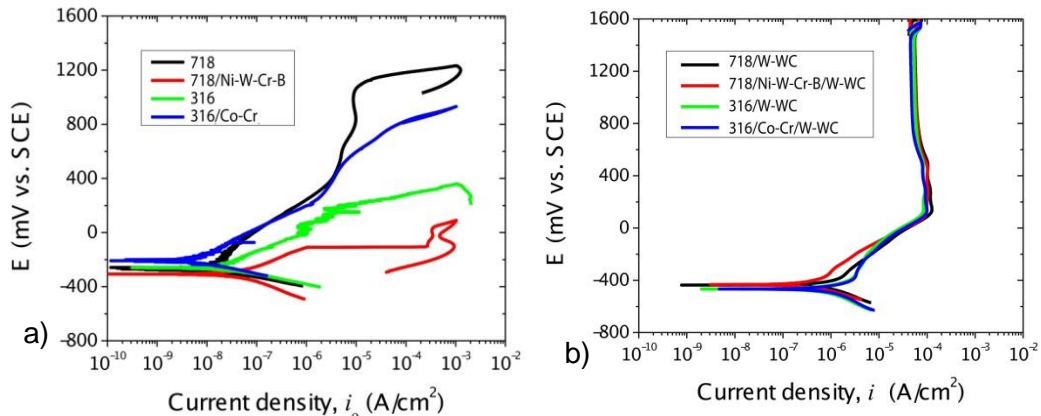


Figure 6-13: Potentiodynamic polarization curves for a) substrate and hardfacings and b) the four coating systems.

The polarization curves for all samples with the W-WC coating are similar, confirming the masking effect of the W-WC layer. In addition, the passive zone extends to 1600 mV with no

signs of pitting. This was confirmed by optical microscopy after polarization, as no pits were observed on the exposed area.

6.4. Conclusions

Two coating systems were investigated: a W-WC thin film deposited onto a laser cladded Co-Cr interlayer applied to an 316 substrate, and a W-WC top layer deposited onto an HVOF sprayed and fused Ni-W-Cr-B interlayer applied to an 718 substrate. X-ray diffraction, energy dispersive spectroscopy, and scanning electron microscopy were used to analyze the microstructure of the coating layers. Adhesion, hardness, and load-carrying capacity were assessed using Vickers and Rockwell indentation. Wear resistance was also assessed with linear reciprocating ball-on-flat sliding wear tests, and corrosion resistance was measured by potentiodynamic polarization and electrochemical impedance spectroscopy.

The interlayers showed no negative impact on W-WC adhesion, as all coating systems applied to the 316 and 718 substrates were considered Class 1 according to CEN/TS 1071-8, with and without an interlayer. The addition of an interlayer increased the micro- and macrohardness of W-WC under high loads, providing the surface with higher load-carrying capacity. However, the sliding wear results were counterintuitive: except for the 718 / Ni-W-Cr-B system, the hardest interlayer or substrate leads to the highest wear rates probably because of a higher contact pressure for a given load. The contrary behavior of the 718 / Ni-W-Cr-B system is most probably due to the composite nature of this interlayer that, despite an overall high hardness, offers zones that can be easily plastically deformed, lowering the contact pressure, as indicated by the low wear rate. Systematic premature delamination of the 316 / Co-Cr / W-WC compared to other coating systems was observed and attributed to the stress-induced fcc \rightarrow hcp phase transformation of the Co-Cr interlayer that occurs at high load and reduces dramatically the interface shear strength. In terms of corrosion, the polarization curves for all samples were similar, confirming that the interlayers did not lower the corrosion resistance of the coating systems.

In summary, superalloy hardfacing used as an interlayer substantially increased the mechanical properties of both studied coating systems, and particularly the load-carrying capacity, without significantly altering corrosion properties of the thin film. Therefore, a hardfaced interlayer is a

promising solution to increase the load-carrying capacity of thin films, and an effective way to adjust the performance of a substrate–coating system.

6.5.Acknowledgements

The authors wish to thank Francis Turcot for his technical support. We would also like to acknowledge Hardide for a fruitful technical exchange. Finally, we greatly appreciate Velan's interest in and support of this study.

CHAPTER 7 GENERAL DISCUSSION, CONCLUSION AND PERSPECTIVES

Valves are critical pieces of equipment for today's industries. They ensure safe, efficient production and flow of the energy and materials required for a myriad of demanding applications. As illustrated by this thesis, material selection is a key factor for minimizing valve wear while maximizing in-service life. Because valves are used in such a vast variety of operations, surface solicitation and degradation mechanisms vary as well, making materials selection a challenge for both valve manufacturers and end users.

Since World War II, three wear-resistant materials, Stellite 6, hard chrome plating, and Teflon, have been predominantly used to mitigate friction and extend the in-service life of these vital machine components. Continuous advances in industrial processes have called for the development of new corrosion- and wear-resistant surface treatments. These include 1) Cr_3C_2 -NiCr applied by High Velocity Oxy-fuel (HVOF) deposition for valves operating in high-temperature high-pressure steam environments (fossil power generation); 2) iron-based galling-resistant hardfacing (Norem 02) applied by plasma transfer arc (PTA) to minimize the presence of cobalt in the primary circuit of pressurized water reactors (nuclear power plants); 3) WC-CoCr applied by HVOF for erosive applications at the moderate temperatures encountered in the upstream oil sector (exploration and production) and for high-pressure slurry pipelines; 4) self-fluxing nickel-based hardfacing (NiCrB); and 5) boriding for abrasive applications in the sour environments encountered in the downstream oil sector (refining and petrochemical industries); and 6) pure ceramics (TiO_2 and/or Cr_2O_3) applied by air plasma spray (APS) for the abrasive conditions encountered in corrosive processes (i.e., hydrometallurgy). However, the optimized tribological solutions that have been developed over the last decade have already reached their limit, and the evidence shows that a substantial number of surface treatment challenges remain to be overcome.

General Discussion

This work has contributed to develop a better understanding of the fundamental physico-chemical phenomena that govern the surface degradation mechanisms occurring during valve life, in conformity with the main objective of the thesis. This was achieved by the completion of four detailed mechanical and tribological studies covering the main wear-resistant materials protecting severe-service valves. Those studies enabled the comprehension of the surface degradation mechanisms, and once the mechanisms were fully understood, more suitable surface treatments were then selected to precisely inhibit these specific degradation mechanisms and ultimately extend valve life.

We established that the comprehension of the degradation mechanism at the micro- and nano-structure levels is essential to understand both the mechanical and tribological response of surfaces; and how they interact with each other to ultimately yield to surface degradation. We found that both adhesion and sliding wear can be controlled by applying tailored thin films possessing high hardness (H) and excellent sliding wear properties. Special care must be given to contact design, because debris and transfer films have an impact on stress distribution, adhesion and sliding wear.

We also established that thin surface treatments with enhanced tribological properties typically exhibit mechanical behaviors that differ from conventional base materials used in the valve industry. This mismatch, combined with limited thickness, might create a high amount of stress at the interface and within the substrate material when subjected to a high concentrated load. This results in high stress levels that can evolve up to permanent surface indentation, crack formation, and / or spallation. The response of the surface is also significantly influenced by the material carrying the top coating; and the system should be optimized as a whole, with respect to tribological performance, mechanical responses, and environmental stability. There is increasing evidence that the optimum solution to erosive, corrosive, and adhesive wear problems lies in multilayered and/or graded coating systems that combine controlled hardness elastic modulus, toughness, and high load-carrying capacity.

This doctoral research project is divided into four parts. The research results are presented in the form of three articles corresponding to three chapters, with the fourth part presented in the Appendix.

Conclusion

The first article (Chapter Four) presents a comprehensive analysis of two nanostructured coatings that are potentially suitable as alternatives to hard chromium (HC). HC, which has been classified by the U.S. Environmental Protection Agency (EPA) as an environmentally unfriendly process, is a widely used surface treatment in the valve industry to protect valves operating at pressures up to 50 bars. The first objective of this research project was therefore to search for a cleaner alternative to HC. Two cost-effective off-the-shelf nanostructured coatings with hard chromium electroplating were identified as candidates and systematically characterized. The two coating systems, tungsten carbide deposited by CVD (W/WC) and cobalt phosphor deposited by pulsed electroplating (NCP), showed attractive tribomechanical and functional characteristics. NCP produces a fourfold lower wear rate and a threefold lower friction coefficient than standard HC plating when using alumina counterbody. However, NCP has proven to be more prone to corrosion, with limited scuffing resistance, whereas W/WC provides a lower wear rate and lower friction coefficient as well as robust corrosion behaviour.

Based on these results Velan Inc. has successfully replaced hard chrome plating with CVD-W/EC for a few projects. These include a petrochemical application, where the cellulose ester sludge containing acetic acid was attacking the interface between the hard chrome plating and SS316, and a nuclear power generator, where hard chrome plating was prohibited by the customer and where a pure Stellite ball had failed.

Chapter Five presents a case study, consisting of a failure analysis of an HVOF 80/20 Cr₃C₂-NiCr coating applied to metal-seated ball valves (MSBVs) used in supercritical power plant steam lines. Although oxidation is known to contribute to coating degradation, carbide precipitation is thought to be the major factor for coating failure. Based on the analysis results, the identified mechanism is that native chrome carbide dissolution due to the high temperatures combined with potential carbon from the fuel enrich the nickel chrome matrix during deposition.

In high-temperature service, chrome carbides reprecipitate across the NiCr matrix, producing a fine network of Cr_3C_2 precipitates that drastically increases the matrix and coating hardness while drastically reducing its toughness. Once the coating toughness and ductility is reduced, thermal, mechanical, and residual stresses can initiate and propagate cracks more easily, causing coating failure when the valve is exposed to thermal shock.

A self-fluxing nickel-based hardfacing that appeared more suitable to support high bearing loads under severe thermal shock was then assessed. This coating is less sensitive to aging at high temperatures, and therefore more durable under these severe conditions. In 2011, based on our failure analysis, Velan modified its material selection, and now offers two coating / substrate combinations for MSBVs used in power plants. Since then, no field service issues have been reported.

Chapter Six presents an investigation of two coating systems: a W-WC thin film deposited onto a laser clad Co-Cr interlayer applied to an SS 316 substrate, and a W-WC top layer deposited onto an HVOF sprayed and fused Ni-W-Cr-B interlayer applied to an Inconel 718 substrate.

The introduction of an interlayer increased the micro- and macrohardness of W-WC under high loads, providing the surface with higher load-carrying capacity. The interlayers showed no negative impact on W-WC adhesion, as all coating systems applied to the SS 316 and Inconel 718 substrates were considered Class 1, with and without an interlayer. However, the results on sliding wear were positive and counterintuitive: except for the 718 / Ni-W-Cr-B system, wear rates were inversely proportional to the yield strength of the material carrying the thin film. This result is most probably due to a more favorable stress distribution under the pin, which may be due to plastic deformation of the substrate and/or interlayer. Another hypothesis in the case of the Stellite interlayer is a local phase transformation. In terms of corrosion, the polarization curves for all samples were similar, confirming that the interlayers did not lower the corrosion resistance of the coating systems. In summary, superalloy hardfacing used as an interlayer substantially increased the mechanical properties of both coating systems, and particularly the load-carrying capacity, without significantly altering the tribological or corrosion properties of the thin film. Therefore, a hardfaced interlayer is a promising solution to increase the load-

carrying capacity of thin films, and an effective way to maximize the performance of a substrate–coating system.

Appendix A provides a report on four recently developed APS ceramic coatings that are potentially suitable for HPAL, namely Cr_2O_3 , n-TiO_2 , $\text{Cr}_2\text{O}_3\text{-TiO}_2$, and $\text{n-TiO}_2\text{-Cr}_2\text{O}_3$. Each coating was subjected to a detailed characterization and an analysis of the wear mechanisms.

The pure Cr_2O_3 blend showed the highest hardness and best sliding wear resistance and COF, whereas the n-TiO_2 showed the lowest hardness, the poorest wear rate, and the highest COF. As expected, the $\text{Cr}_2\text{O}_3\text{-TiO}_2$ and $\text{n-TiO}_2\text{-Cr}_2\text{O}_3$ blends provided hardness and sliding characteristics that were in between those of the pure ceramics. In terms of abrasion, the results were positive and counterintuitive: the $\text{n-TiO}_2\text{-Cr}_2\text{O}_3$ blend showed superior resistance for both dry and wet abrasion tests compared to the pure ceramics. Based on the literature, the high performance of the $\text{n-TiO}_2\text{-Cr}_2\text{O}_3$ can be attributed to the optimized balance between the hard and brittle Cr_2O_3 phases and the soft and ductile TiO_2 phases.

The results of this investigation demonstrate how the synergy between the two pure ceramics provides superior abrasion performance to that for the individual ceramics. Promisingly, the novel $\text{n-TiO}_2\text{-Cr}_2\text{O}_3$ blend produced consistently better tribological performance than the $\text{TiO}_2\text{-Cr}_2\text{O}_3$ blend. Consequently, this novel blend promises to be a significant advance over the current $\text{TiO}_2\text{-Cr}_2\text{O}_3$ blend.

Perspectives

Being the first Ph.D. candidate from FCSEL to devote his research to surface engineering applied to valves, I had to make a fresh start by exploring areas of this multifaceted industry that are underrepresented in the literature. I hope that this doctoral work will accelerate the learning curve for future Ph.D. candidates. In fact, certain high-potential research avenues have emerged, pointing the way to future research directions, along with more general observations on surface engineering principles applied to valves that may inspire further initiatives.

Starting with the specifics, the disaffinity of hard chrome plating for heavy petroleum products and the resulting anti-sticking property have been insufficiently documented. Given that these properties are crucial for downstream applications, more research is needed to quantify the oil-repealing capacity of available surface treatments, including the alternative coatings investigated in this doctoral work. Future studies could consider the different classes of heavy petroleum products, such as bitumen, asphalt, and tar, as well as the different operating conditions, such as pressure and temperature, which could result in diverse solidification and bonding mechanisms.

A second research avenue would be to improve the wear resistance of cobalt-chrome adaptive materials. New manufacturing processes could aim to optimize the grain size (i.e., nanostructured particles) and phase distribution (i.e., homogeneity or controlled inhomogeneity) in order to maximize the material strength without affecting the anti-galling properties. This optimization process will require novel feedstock material (e.g., powder, gas) and deposition processes (e.g., thermal spraying, vapor deposition), and the outcomes should be dramatically increased hardness and abrasion resistance. An optimized microstructure should limit the volume loss over time and enable the use of cobalt-chrome adaptive materials in areas where they are currently not the preferred solution, especially for the nuclear power generation, refining, and petrochemical industries.

For power generation, four particular items merit investigation:

- 1) The mechanical properties of Inconel 718 coated with self-fluxing nickel-based hardfacing needs to be more systematically documented, in particular the impact of post-fusing treatment on

the nickel-based superalloy. In addition, alternative deposition processes such as laser cladding should be assessed.

2) A trim composed of an Inconel 718 ball hardfaced with self-fluxing nickel-based and an Inconel 718 seat coated with HVOF Cr_2C_3 -NiCr should also be analyzed. In fact, the HVOF-coated seat has never failed in service, most likely due to its higher rigidity and thermal inertia. This combination of dissimilar materials should mitigate the risk of galling while improving sliding wear.

3) A significant number of high-temperature applications requiring Inconel 718 hardfaced with a self-fluxing nickel-based alloy are required to operate at temperatures ranging from 540 °C to 590 °C. This performance should be achievable with a novel martensitic stainless steel (UNS S42200 – AISI 616) provided with an HVOF coating.

4) Researchers should continue to develop coatings for use in gamma-prime strengthened nickel-based materials for SC and U-ASC applications up to 760 °C / 500 bar, keeping in mind that thermal stress, aging, and galling are more likely to occur than sliding wear. With their high ductility (i.e., strain to fracture), elevated high-temperature hardness, and a coefficient of thermal expansion close to that for Waspaloy, Inconel 740, and/or Haynes 282, 50/50 Cr_3C_2 -NiCrMoNb (Amperit 595) and Triballoy 800 are promising candidates for protective coatings. In addition, the use of colder deposition processes should be investigated to minimize in-flight decarburization. Post-deposition heat treatment should also be considered for controlling the final microstructure and bond strength (i.e., diffusion).

With respect to thin-on-thick hybrid coatings in particular and protective coatings in general, finite element models would be useful for predicting mechanical and thermal stress and for identifying the need for added interlayers to improve stress control. This would be particularly salient for coating processes that result in an abrupt coating–substrate interface, such as CVD and thermal spraying, as well as laser cladding. These processes are widely used in industries because they minimize impacts on bulk material and limit dilution. In addition, cross-sections of thin-on-thick samples should be analyzed, and particularly the interlayer and the substrate material beneath the wear track. Special attention should be paid to potential Stellite phase

transformation: it may explain high wear rate and delamination, and could be mitigated by pre-treatment.

For the highly corrosive environments encountered in hydrometallurgy, systematic failure analyses are needed to guide the development of n-TiO₂-Cr₂O₃ coating, powder preparation, and spraying parameters in order to inform adjustments to maximize cohesive strength, strain to fracture, and corrosion resistance. Different sealants (epoxy, silicone, and urethane) should also be assessed in corrosion tests, and the development of an HVOF process capable of spraying n-TiO₂-Cr₂O₃ could be considered to minimize quenching. The challenge here would be to ensure that the Cr₂O₃ particles melt in order to avoid particle rebound when impacting the substrate as well as particle erosion of the deposited TiO₂ layer. Thermal spray processes have intrinsic weaknesses, and should be viewed as “local optimums” when applying ceramics for corrosive applications. Finally, new deposition methods (e.g., vapor deposition) that are less prone to spalling would offer innovative directions.

Although I do not pretend to have either the resources or the time to solve all the above challenges, or others to come, I am gratified that my doctoral work has influenced Velan to join the NSERC Multisectorial Industrial Research Chair in Coatings and Surface Engineering (MIC-CSE), launched in 2012 by Ludvik Martinu and Jolanta Ewa Klemberg-Sapieha in collaboration with six industrial partners. By actively participating in this conglomerate, Velan has joined a partnership that will facilitate the definition of mid- and long-term R&D projects, set priorities, and systematically overcome challenges in the field of protective coatings. While efforts are needed to mitigate sliding wear and increase the in-service life of existing valves by optimizing materials selection, special care should be taken to collect quantitative data (e.g., maximum pressure x temperature coefficients for material couples) and to develop methodologies (e.g., finite element analysis) to facilitate the engineering of made-to-order products that are compact and robust, using optimized contact design (e.g., elevated uniform bearing stress distribution combined with debris evacuation features). These highly optimized products will not be prone to premature catastrophic failures caused by surface-degradation mechanisms such as spalling, galling, plastic deformation, egg-shell effect, and corrosion. Furthermore, this effort should

include fundamental research to deepen the understanding of material properties, contact geometry, stress intensity, and sealing capability.

REFERENCES

- [1] G. M. Labs. (2014, 26 June 2014). *Cost of corrosion estimated to exceed \$1 trillion in the United States in 2013*. Available: <http://www.g2mtlabs.com/2011/06/nace-cost-of-corrosion-study-update/>
- [2] M. V. Biezma and J. R. San Cristobal, "Methodology to study cost of corrosion," *Corrosion Engineering Science and Technology*, vol. 40, pp. 344-352, 2005.
- [3] H. P. Jost, *Lubrication: tribology; education and research; report on the present position and industry's needs (submitted to the department of education and science by the lubrication engineering and research working group)*: HM Stationery Office, 1966.
- [4] F. Wayne and P. E. Lorenz, "Ancient roman valves," *Valve magazine*, 2013.
- [5] L. Mays, "A very brief history of hydraulic technology during antiquity," *Environmental Fluid Mechanics*, vol. 8, pp. 471-484, 2008/12/01 2008.
- [6] D. L. Crandall, *et al.*, *Diffusion bonding resistant valve development for sodium service*, 1984.
- [7] G. E. Kim, *et al.*, "Thermal spray coatings for ball valves used in Nickel/Cobalt pressure acid leaching," in *International Spray Show Conference*, Montreal, Canada, 2000, pp. 1149-1153.
- [8] G. Y. Qiao and J. Hill, "MOGAS M7 a performance enhanced nano-structured titanium dioxide coating in HPAL and POx ball valve applications," presented at the ALTA, Perth, Australia, 2014.
- [9] D. Xu, *et al.*, "Mechanical jamming analysis of the reheat-stop-valve mechanism in the supercritical steam turbine," *Jixie Gongcheng Xuebao/Journal of Mechanical Engineering*, vol. 46, pp. 121-127, 2010.
- [10] S. Bhowmick, *et al.*, "Contact damage in TiN coatings on steel," *Thin Solid Films*, vol. 436, pp. 250-258, 2003.
- [11] F. Casadei and M. Tului, "Combining thermal spraying and PVD technologies: A new approach of duplex surface engineering for Ti alloys," *Surface and Coatings Technology*, vol. 237, pp. 415-420, 2013.
- [12] K. M. Retzlaff and W. A. Ruegger, "Steam turbines for ultrasupercritical power plants," presented at the Power-Gen Europe, Budapest, 1996.
- [13] G. Johnson, "A history made in metal," *Valve magazine*, 2013.

- [14] W. C. Madden, *Haynes-Apperson and America's first practical automobile: a history*. Jefferson, NC: McFarland, 2003.
- [15] E. Haynes, "Alloys of cobalt with chromium and other metals," *Industrial & Engineering Chemistry*, vol. 5, pp. 189-191, 1913.
- [16] J. Vikström, "Galling resistance of hardfacing alloys replacing Stellite," *Wear*, vol. 179, pp. 143-146, 1994.
- [17] J. S. Hansen, *et al.*, "Erosion testing of potential valve materials for coal gasification systems," Bureau of Mines, Albany, OR (USA). Albany Metallurgy Research Center 1979.
- [18] D. Buckley and R. Johnson, "The influence of crystal structure and some properties of hexagonal metals on friction and adhesion," *Wear*, vol. 11, pp. 405-419, 1968.
- [19] D. H. Persson, "On the mechanisms behind the tribological performance of Stellites," PhD Thesis, Materials Science, Universitatis Upsaliensis, Sweden, 2005.
- [20] Worcester. (2014, 14 Aug 2014). *Worcester's industrial heritage*. Available: <http://www.worcesterhistory.org/enterprise-4b-freeman.html>
- [21] G. Johnson, "From a humble beginning, an industry rises," *Valve magazine*, 2012.
- [22] W. Zmudzinski and M. Ezekiel, "Coating and overlays for critical valve applications," in *Materials Forum*, 2006, pp. 333-338.
- [23] M. A. Rosen, "Energy- and exergy-based comparison of coal-fired and nuclear steam power plants," *Exergy, An International Journal*, vol. 1, pp. 180-192, 2001.
- [24] R. P. Pecoskie and D. W. Parker, "Coatings protect severe-service ball valves," *Advanced Materials and Processes*, vol. 144, pp. 22-25, 1993.
- [25] S. Kjær, *et al.*, "The advanced supercritical 700 C pulverised coal-fired power plant," *VGB powertech*, vol. 82, pp. 46-49, 2002.
- [26] R. Kehlhofer, *et al.*, *Combined-cycle gas & steam turbine power plants*. Tulsa, OK: Pennwell Books, 2009.
- [27] N. Kumar, *et al.*, "Power plant cycling costs," *Contract*, vol. 303, pp. 275-3000, 2012.
- [28] T. Lolla, *et al.*, "Delamination failures of Stellite hardfacing in power plants: a microstructural characterisation study," *Science and Technology of Welding and Joining*, 2014.

- [29] A. Fernandes, *et al.*, "Study on the fatigue failure of a cobalt hardfaced steel shaft," in *European Conference on Fracture*, Lisbon, 1984.
- [30] B. S. Mann and B. Prakash, "High temperature friction and wear characteristics of various coating materials for steam valve spindle application," *Wear*, vol. 240, pp. 223-230, 2000.
- [31] R. C. Howard, "Installation of Valvtechnologies ball valves in severe service applications within the advanced test reactor," in *14th International Conference on Nuclear Engineering*, Miami FL, USA, 2006, pp. 641-644.
- [32] L. Berger, "Tribological behavior of HVOF-sprayed Cr₃C₂-NiCr and TiC-based coatings under high-temperature dry sliding conditions," presented at the Thermal Spray 2004: Advances in Technology and Application, Osaka, Japan, 2004.
- [33] W. Wang, "Application of a high temperature self-lubricating composite coating on steam turbine components," *Surface and Coatings Technology*, vol. 177, pp. 12-17, 2004.
- [34] P. S. Weitzel, "Steam generator for advanced ultra supercritical power plants 700C to 760C," in *ASME 2011 Power Conference collocated with JSME ICOPE 2011*, 2011, pp. 281-291.
- [35] M. Fukuda, *et al.*, "Advanced USC technology development in Japan," in *Proceedings of 6th Int. Conference Advances in Materials Technology for Fossil Power Plants*, 2011, pp. 325-341.
- [36] H. Ocken, "Reducing the cobalt inventory in light water reactors," *Nuclear technology*, vol. 68, pp. 18-28, 1985.
- [37] H. Ocken, "The galling wear resistance of new iron-base hardfacing alloys: A comparison with established cobalt- and nickel-base alloys," *Surface & Coatings Technology*, vol. 76-77, pp. 456-461, Dec 1995.
- [38] L. Cachon, *et al.*, "Tribological qualification of cobalt-free coatings for pressurized water reactor primary-circuit gate valve applications," *Surface & Coatings Technology*, vol. 85, pp. 163-169, Nov 15 1996.
- [39] J. K. Kim and S. J. Kim, "The temperature dependence of the wear resistance of iron-base NOREM 02 hardfacing alloy," *Wear*, vol. 237, pp. 217-22, 2000.
- [40] B. V. Cockeram, *et al.*, "Laboratory galling tests of several commercial cobalt-free weld hardfacing alloys," *Surface & Coatings Technology*, vol. 94-5, pp. 495-500, Oct 1997.

- [41] D. H. Persson, *et al.*, "Effect of temperature on friction and galling of laser processed Norem 02 and Stellite 21," *Wear*, vol. 255, pp. 498-503, 2003.
- [42] T. Yoshioka, *et al.*, "Ceramic coating for valve seats and stems by plasma chemical vapor deposition," *Surface and Coatings Technology*, vol. 49, pp. 97-102, 1991.
- [43] A. Kawana, *et al.*, "Development of PVD ceramic coatings for valve seats," *Surface and Coatings Technology*, vol. 86, pp. 212-217, 1996.
- [44] Y. Kiyotoki and M. Chigasaki, "HHC (Hitachi Hyper Valve): corrosion resistant, withstands erosion and low Co release," in *ASME/JSME 2004 Pressure Vessels and Piping Conference*, 2004, pp. 83-87.
- [45] T. Allen, *et al.*, "Materials challenges for nuclear systems," *Materials today*, vol. 13, pp. 14-23, 2010.
- [46] W. D. Manly, "Construction materials for molten-salt reactors," presented at the Fluid-Fueled Reactors, Oak Ridge, TN, USA, 1958.
- [47] D. C. Smith, *et al.*, "Operation of large-scale pumps and valves in molten salt," *Journal of Solar Energy Engineering, Transactions of the ASME*, vol. 116, pp. 137-141, 1994.
- [48] D. Wheeler and R. Wood, "Erosion of hard surface coatings for use in offshore gate valves," *Wear*, vol. 258, pp. 526-536, 2005.
- [49] R. Wood, *et al.*, "Upstream swirl-induction for reduction of erosion damage from slurries in pipeline bends," *Wear*, vol. 250, pp. 770-778, 2001.
- [50] R. Wood and D. Wheeler, "Design and performance of a high velocity air-sand jet impingement erosion facility," *Wear*, vol. 220, pp. 95-112, 1998.
- [51] J. A. Wesmann, *et al.*, "Friction evolution of WC-CoCr thermally sprayed coatings during dry sliding in different environment," in *International Thermal Spray Conference and Exposition: Innovative Coating Solutions for the Global Economy, ITSC 2013, May 13, 2013 - May 15, 2013*, Busan, Korea, Republic of, 2013, pp. 457-459.
- [52] R. Wood, *et al.*, "Sand erosion performance of detonation gun applied tungsten carbide/cobalt-chromium coatings," *Wear*, vol. 211, pp. 70-83, 1997.
- [53] K. Haugen, *et al.*, "Sand erosion of wear-resistant materials: erosion in choke valves," *Wear*, vol. 186-187, Part 1, pp. 179-188, 1995.

- [54] B. Mann, *et al.*, "Corrosion and erosion performance of HVOF/TiAlN PVD coatings and candidate materials for high pressure gate valve application," *Wear*, vol. 260, pp. 75-82, 2006.
- [55] D. Wheeler, *et al.*, "Application of diamond to enhance choke valve life in erosive duties," *Wear*, vol. 261, pp. 1087-1094, 2006.
- [56] D. J. Tillack and J. E. Guthrie, "Select the right alloys for refineries and petrochemical plants," *Chemical Engineering Progress*, vol. 95, pp. 59-66, 1999.
- [57] R. Sadeghbeigi, *Fluid catalytic cracking handbook: An expert guide to the practical operation, design, and optimization of FCC units*. Waltham MA: Elsevier, 2012.
- [58] D. Cooper, *et al.*, "Selection of wear resistant materials for the petrochemical industry," *Journal of Physics D: Applied Physics*, vol. 25, p. A195, 1992.
- [59] H. S. Sidhu, *et al.*, "Hot corrosion behavior of HVOF sprayed coatings on ASTM SA213-T11 steel," *Journal of Thermal Spray Technology*, vol. 16, pp. 349-354, 2007/09/01 2007.
- [60] J. Cataldo, *et al.*, "Boride surface treatments," *Advanced Materials and Processes*, vol. 157, pp. 35-38, 2000.
- [61] E. K. Isakaev and V. Mordynskii, "Corrosion cracking resistance of deposited self-fluxing alloys in hydrogen sulphide-containing media," *Welding International*, vol. 23, pp. 939-943, 2009.
- [62] E. Lugscheider, *et al.*, "Advances in PTA surfacing," *Thermal Spray Coatings: Properties, Processes and Applications*, pp. 529-535, 1991.
- [63] F. Stott, *et al.*, "The structure and mechanism of formation of the 'glaze' oxide layers produced on nickel-based alloys during wear at high temperatures," *Corrosion Science*, vol. 13, pp. 449-469, 1973.
- [64] K. Gurumoorthy, *et al.*, "Microstructural aspects of plasma transferred arc surfaced Ni-based hardfacing alloy," *Materials Science and Engineering: A*, vol. 456, pp. 11-19, 2007.
- [65] X. Wang, *et al.*, "CVD diamond films as wear-resistant coatings for relief valve components in the coal liquefaction equipment," in *4th Conference on Application of Diamond and Related Materials in China, CADRM2010 and the 1st International*

- Symposium on Advances in Brazed Superabrasive Tools, ISABS2010, August 19, 2010 - August 23, 2010, Xiamen, China, 2011, pp. 219-225.*
- [66] J. Williams, "Field performance review of autoclave valves," presented at the Alta conference, Perth, Australia, 2009.
 - [67] P. Fauchais and A. Vardelle, "Thermal sprayed coatings used against corrosion and corrosive wear," *Advanced Plasma Spray Applications*, pp. 3-38, 2012.
 - [68] B. Hood, "Hardening reactive and refractory metal valves," *ChemInfo*, 2010 2010.
 - [69] A. Scrivani, *et al.*, "A contribution to the surface analysis and characterisation of HVOF coatings for petrochemical application," *Wear*, vol. 250, pp. 107-113, 2001.
 - [70] M. Cartier and T. Polak, *Handbook of surface treatments and coatings*: Amer Society of Mechanical, 2003.
 - [71] "Guidance for the use of alternatives to hexavalent chromium for the protective coating of defence equipment," ed: Ministry of Defence, 2007.
 - [72] C. Forsich, *et al.*, "Potential of thick aC: H: Si films as substitute for chromium plating," *Surface and Coatings Technology*, vol. 241, pp. 86-92, 2014.
 - [73] A. Burkov and S. Pyachin, "Investigation of WC-Co electrospark coatings with various carbon contents," *Journal of Materials Engineering and Performance*, vol. 23, pp. 2034-2042, 2014.
 - [74] J. Vetter, *et al.*, "Hard coatings on thermochemically pretreated soft steels: application potential for ball valves," *Surface and Coatings Technology*, vol. 111, pp. 210-219, 1999.
 - [75] D. R. Kaushal, *et al.*, "Concentration at the pipe bottom at deposition velocity for transportation of commercial slurries through pipeline," *Powder Technology*, vol. 125, pp. 89-101, 2002.
 - [76] E. J. Wasp, *et al.*, "Solid-liquid flow: slurry pipeline transportation.[Pumps, valves, mechanical equipment, economics]," *Ser. Bulk Mater. Handl.:(United States)*, vol. 1, 1977.
 - [77] H. Hocke and H. N. Wilkinson, "Testing abrasion resistance of slurry pipeline materials," *Tribology International*, vol. 11, pp. 289-294, 1978.
 - [78] H. Hawthorne, *et al.*, "Comparison of slurry and dry erosion behaviour of some HVOF thermal sprayed coatings," *Wear*, vol. 225, pp. 825-834, 1999.

- [79] D. K. Goyal, *et al.*, "Slurry erosive wear evaluation of HVOF-spray Cr_2O_3 coating on some turbine steels," *Journal of Thermal Spray Technology*, vol. 21, pp. 838-851, 2012.
- [80] D. K. Goyal, *et al.*, "Erosive wear study of HVOF spray Cr_3C_2 -NiCr coated CA6NM turbine steel," *Journal of Tribology*, vol. 136, p. 041602, 2014.
- [81] D. Kumar Goyal, *et al.*, "Slurry erosion behaviour of HVOF sprayed WC-10Co-4Cr and Al_2O_3 +13TiO₂ coatings on a turbine steel," *Wear*, vol. 289, pp. 46-57, 2012.
- [82] Y. C. Zhu, *et al.*, "Deposition and characterization of nanostructured WC-Co coating," *Ceramics International*, vol. 27, pp. 669-674, 2001.
- [83] M. Harrison, "Severe service ball valve for high pressure slurry pipeline," presented at the Rio Pipeline Conference and Exposition 2009, 2009.
- [84] G. Kim and J. Walker, "Successful application of nanostructured titanium dioxide coating for high-pressure acid-leach application," *Journal of Thermal Spray Technology*, vol. 16, pp. 34-39, 2007.
- [85] R. S. Lima, *et al.*, "Abrasion behaviour of nanostructured and conventional titania coatings thermally sprayed via APS, VPS and HVOF," in *International Thermal Spray 2004 Conference*, Osaka, Japan, 2004.
- [86] L. Leblanc, *et al.*, "High performance coatings for severe service ball valves in HPAL: development and field results," presented at the ALTA, Perth, Australia, 2008.
- [87] R. Rajasekariah and S. Vaidyanathan, "Increasing the wear-resistance of steel components by ball burnishing," *Wear*, vol. 34, pp. 183-188, 1975.
- [88] N. El-Tayeb, *et al.*, "Influence of roller burnishing contact width and burnishing orientation on surface quality and tribological behaviour of Aluminium 6061," *Journal of Materials Processing Technology*, vol. 186, pp. 272-278, 2007.
- [89] M. H. El-Axir, "An investigation into roller burnishing," *International Journal of Machine Tools and Manufacture*, vol. 40, pp. 1603-1617, 2000.
- [90] J. Grum, "Induction hardening," *Handbook of residual stress and deformation of steel*, vol. 1, pp. 220-247, 2002.
- [91] D. Hertz, *et al.*, "Principes et technologies des traitements de nitruration et cémentation à basse température," presented at the Congrès du Traitement Thermique et de l'Ingénierie des Surfaces, Bordeaux, France, 2006.

- [92] V. Jain and G. Sundararajan, "Influence of the pack thickness of the boronizing mixture on the boriding of steel," *Surface and Coatings Technology*, vol. 149, pp. 21-26, 2002.
- [93] D. Vojtěch, *et al.*, "Surface protection of titanium by Ti_5Si_3 silicide layer prepared by combination of vapour phase siliconizing and heat treatment," *Journal of Alloys and Compounds*, vol. 464, pp. 179-184, 2008.
- [94] G. Meier, *et al.*, "Diffusion chromizing of ferrous alloys," *Surface and Coatings Technology*, vol. 39, pp. 53-64, 1989.
- [95] H. Allison and L. Hawkins, "Calorizing metal protecting treatment," *GE rev.*, 17, 947-51, 1914; *Sci. Am. supp.* 78, 341-2, 1914; *condensed, Am. gas light j.*, 101, 309-10, 1014; *Eng. mag.*, 48, 265-7, '914; *Met. chcm. eng.*, 12, vol. 730, 1914.
- [96] L. L. Ornstein, "The tungstenizing of steel," Ohio State University, Columbus, OH, 1943.
- [97] M. Kashaba, *et al.*, "Wear resistant coatings by siliconizing and titanizing of steel," *Metall*, vol. 49, pp. 430-432, 1995.
- [98] K.-H. Habig, "Wear protection of steels by boriding, vanadizing, nitriding, carburising, and hardening," *Materials & Design*, vol. 2, pp. 83-92, 1980.
- [99] M. Ohring, *Materials science of thin films*. London, UK: Academic press, 2001.
- [100] R. F. Bunshah, *Handbook of deposition technologies for films and coatings: science, technology, and applications*. Westwood, NJ: William Andrew, 1994.
- [101] H. O. Pierson, *Handbook of chemical vapor deposition: principles, technology and applications*. Norwich, NY: William Andrew, 1999.
- [102] L. K. Ives, *et al.*, "Galling: mechanism and measurement," in *National Bureau of Standards Report*, ed, 1987, pp. 33-40.
- [103] J. F. Lancaster, "Physics of welding," *Physics in technology*, vol. 15, pp. 73-79, 1984.
- [104] Hayden. (2014, 9 June 2014). *Hayden corporation*. Available: <http://www.haydencorp.com/>
- [105] ASTM, "Standard terminology relating to wear and erosion," ed. West Conshohocken, PA: ASTM International, 2013.
- [106] S. Hadavi, *et al.*, "The effect of thermal fatigue on the hardness of hard chromium electroplatings," *Journal of Materials Processing Technology*, vol. 147, pp. 385-388, 2004.

- [107] J. Tyler, "Automotive applications for chromium," *Metal Finishing*, vol. 93, pp. 11-14, 1995.
- [108] J. L. McRea, *et al.*, "Nanocrystalline Co-P coatings for chrome replacement within the aerospace industry," *Integran*, 2005.
- [109] I. ASM, *Surface engineering* vol. 5: ASM International, 1994.
- [110] G. V. s. GmbH. (2014, 9 June 2014). Available: <http://www.gtv-mbh.com/>
- [111] F. J. Hermanek, *Thermal spray terminology and company origins*: ASM International, 2001.
- [112] R. C. Tucker Jr, "Thermal spray coatings," *ASM International, Member/Customer Service Center, Materials Park, OH 44073-0002, USA, 1994.*, pp. 497-509, 1994.
- [113] S. Hogmark, *et al.*, "Tribological properties of thin hard coatings: demands and evaluation," *Surface and Coatings Technology*, vol. 90, pp. 247-257, 1997.
- [114] C. U. Hardwicke and Y.-C. Lau, "Advances in thermal spray coatings for gas turbines and energy generation: a review," *Journal of Thermal Spray Technology*, vol. 22, pp. 564-576, 2013.
- [115] H. S. Ingham and A. P. Shepard, *Flame spray handbook* vol. II: Metco Inc. , 1967.
- [116] R. D. Koester and D. P. Moak, "Hot hardness of selected borides, oxides, and carbides to 1900°C," *Journal of the American Ceramic Society*, vol. 50, pp. 290-296, 1967.
- [117] A. Wank, *et al.*, "Performance of thermal spray coatings under dry abrasive wear conditions," in *The Coatings, Fourth Int. Conf. Proc*, 2004, pp. 5-7.
- [118] E. Bergonzini, *et al.*, "Wear behaviour of HVOF-sprayed nanostructured WC-CoCr coatings," presented at the ITSC, Hamburg, 2011.
- [119] D. Li and J. E. Klemberg-Sapieha, "Comparison of tribo-mechanical properties of different coatings applied to valves," *Functional Coatings and Surface Engineering Laboratory*, Montréal, 2013.
- [120] R. Gonzalez, *et al.*, "Microstructural study of NiCrBSi coatings obtained by different processes," *Wear*, vol. 263, pp. 619-624, 2007.
- [121] C. Navas, *et al.*, "Abrasive wear behaviour of laser clad and flame sprayed-melted NiCrBSi coatings," *Surface and Coatings Technology*, vol. 200, pp. 6854-6862, 2006.

- [122] M. Planche, *et al.*, "Relationships between NiCrBSi particle characteristics and corresponding coating properties using different thermal spraying processes," *Surface and Coatings Technology*, vol. 200, pp. 2465-2473, 2005.
- [123] L. Martinu and D. Poitras, "Plasma deposition of optical films and coatings: A review," *Journal of Vacuum Science & Technology A*, vol. 18, pp. 2619-2645, 2000.
- [124] Z. He, *et al.*, "Ion-assisted deposition of CN and SiCN films," *Thin Solid Films*, vol. 283, pp. 90-96, 1996.
- [125] K. Kutschej, *et al.*, "Structure, mechanical and tribological properties of sputtered $Ti_{1-x}Al_xN$ coatings with $0.5 \leq x \leq 0.75$," *Surface and Coatings Technology*, vol. 200, pp. 2358-2365, 2005.
- [126] K. Bose and R. Wood, "High velocity solid particle erosion behaviour of CVD boron carbide on tungsten carbide," *Wear*, vol. 258, pp. 366-376, 2005.
- [127] J. Patscheider, "Nanocomposite hard coatings for wear protection," *MRS bulletin*, vol. 28, pp. 180-183, 2003.
- [128] P. Jedrzejowski, *et al.*, "Relationship between the mechanical properties and the microstructure of nanocomposite TiN/SiN_{1.3} coatings prepared by low temperature plasma enhanced chemical vapor deposition," *Thin Solid Films*, vol. 426, pp. 150-159, 2003.
- [129] P. Jedrzejowski, *et al.*, "Mechanical and optical properties of hard SiCN coatings prepared by PECVD," *Thin Solid Films*, vol. 447-448, pp. 201-207, 2004.
- [130] S. Guruvenket, *et al.*, "Mechanical and tribological properties of duplex treated TiN, nc-TiN/a-SiN_x and nc-TiCN/a-SiCN coatings deposited on 410 low alloy stainless steel," *Surface and Coatings Technology*, vol. 203, pp. 2905-2911, 2009.
- [131] S. Hassani, *et al.*, "Design of hard coating architecture for the optimization of erosion resistance," *Wear*, vol. 265, pp. 879-887, 2008.
- [132] D. Li, *et al.*, "Corrosion and tribo-corrosion enhancement of SS301 and Ti-6Al-4V substrates by amorphous hydrogenated SiN/SiC/aC multilayer coating architecture," *Surface and Coatings Technology*, vol. 206, pp. 1893-1898, 2011.
- [133] S. Veprek, *et al.*, "Different approaches to superhard coatings and nanocomposites," *Thin Solid Films*, vol. 476, pp. 1-29, 2005.

- [134] R. F. Zhang, *et al.*, "Mechanical and electronic properties of hard rhenium diboride of low elastic compressibility studied by first-principles calculation," vol. 91, pp. 201914-1, 2007.
- [135] J. Musil, "Hard and superhard nanocomposite coatings," *Surface and Coatings Technology*, vol. 125, pp. 322-330, 2000.
- [136] J. Musil and M. Jirout, "Toughness of hard nanostructured ceramic thin films," *Surface and Coatings Technology*, vol. 201, pp. 5148-5152, 2007.
- [137] A. Leyland and A. Matthews, "Design criteria for wear-resistant nanostructured and glassy-metal coatings," *Surface and Coatings Technology*, vol. 177, pp. 317-324, 2004.
- [138] S. Zhang, *et al.*, "Ni-toughened nc-TiN/a-SiN_x nanocomposite thin films," *Surface and Coatings Technology*, vol. 200, pp. 1530-1534, 2005.
- [139] S. Lee, *et al.*, "Characterization of boron carbide thin films fabricated by plasma enhanced chemical vapor deposition from boranes," *Journal of applied physics*, vol. 72, pp. 4925-4933, 1992.
- [140] I. M. Hutchings, *Tribology: friction and wear of engineering materials*. London, UK: Edward Arnold, 1992.
- [141] D. Tabor, *The hardness of metals*: Clarendon Press, Oxford University Press, 1951.
- [142] M. F. Ashby, "Materials selection in mechanical design," ed: Pergamon Press, Oxford, 2002.
- [143] R. Hill, "General features of plastic-elastic problems as exemplified by some particular solutions," *J. Appl. Mech*, vol. 16, pp. 295-300, 1949.
- [144] H. Holleck and V. Schier, "Multilayer PVD coatings for wear protection," *Surface and Coatings Technology*, vol. 76-77, Part 1, pp. 328-336, 1995.
- [145] W. D. Sproul, "Very high rate reactive sputtering of TiN, ZrN and HfN," *Thin Solid Films*, vol. 107, pp. 141-147, 1983.
- [146] W. D. Sproul and M. H. Richman, "Reactive sputtering of TiC with oxygen," *Thin Solid Films*, vol. 28, pp. 39-40, 1975.
- [147] Y. Zhuk, "Nanostructured pore-free abrasion-resistant coating for valves," *Valve world*, vol. Octobre, pp. 73-76, 2006.
- [148] E. Hall, "The deformation and ageing of mild steel: III discussion of results," *Proceedings of the Physical Society. Section B*, vol. 64, p. 747, 1951.

- [149] N. Petch, "The cleavage strength of polycrystals," *J. Iron Steel Inst.*, vol. 174, pp. 25-28, 1953.
- [150] A. Chokshi, *et al.*, "On the validity of the Hall-Petch relationship in nanocrystalline materials," *Scripta Metallurgica*, vol. 23, pp. 1679-1683, 1989.
- [151] J. Schiøtz, *et al.*, "Softening of nanocrystalline metals at very small grain sizes," *Nature*, vol. 391, pp. 561-563, 1998.
- [152] H. Hertz, "On the contact of elastic solids," *J. reine angew. Math*, vol. 92, pp. 156-171, 1881.
- [153] A. Leyland and A. Matthews, "On the significance of the H/E ratio in wear control: a nanocomposite coating approach to optimised tribological behaviour," *Wear*, vol. 246, pp. 1-11, 2000.
- [154] K. L. Johnson, *Contact mechanics*: Cambridge university press, 1987.
- [155] K.-H. Zum Gahr, *Microstructure and wear of materials* vol. 10. New York: Elsevier, 1987.
- [156] S. Zhang, *et al.*, "Recent advances of superhard nanocomposite coatings: a review," *Surface and Coatings Technology*, vol. 167, pp. 113-119, 2003.
- [157] E. Bemporad, *et al.*, "Tribological studies on PVD/HVOF duplex coatings on Ti6Al4V substrate," *Surface & Coatings Technology*, vol. 203, pp. 566-71, 2008.
- [158] G. Bolelli, *et al.*, "Thermally sprayed coatings as interlayers for DLC-based thin films," *Journal of Thermal Spray Technology*, vol. 18, pp. 231-242, 2009.
- [159] A. Matthews, *et al.*, "Tribological coatings: contact mechanisms and selection," *Journal of Physics D: Applied Physics*, vol. 40, pp. 5463-5468, 2007.
- [160] A. Roach, *et al.*, "Scoring characteristics of thirty-eight different elemental metals in high-speed sliding contact with steel," *Trans. ASME*, vol. 78, pp. 1659-1667, 1956.
- [161] D. H. Buckley, *Surface effects in adhesion, friction, wear, and lubrication* vol. 5. Amsterdam, The Netherland: Elsevier, 1981.
- [162] H. Czichos, "Tribology: a systems approach to the science and technology of friction, lubrication, and wear," ed: Elsevier, Amsterdam, 1978.
- [163] K. Holmberg, *et al.*, "Coatings tribology—contact mechanisms and surface design," *Tribology International*, vol. 31, pp. 107-120, 1998.

- [164] M. Antonov and I. Hussainova, "Thermophysical properties and thermal shock resistance of chromium carbide based cermets," *Proceedings of the Estonian Academy of Sciences (Engineering)*, vol. 12, pp. 358-67, 2006.
- [165] A. Tipton, "The effect of HVOF thermal spray on the elevated temperature high cycle fatigue behavior of a martensitic stainless steel," *Dresser-Rand, New York, NY*, 2002.
- [166] K. Holmberg, *et al.*, "Tribological contact analysis of a rigid ball sliding on a hard coated surface Part II: Material deformations, influence of coating thickness and Young modulus," *Surface and Coatings Technology*, vol. 200, pp. 3810-3823, 2006.
- [167] W. C. Oliver and G. M. Pharr, "Measurement of hardness and elastic modulus by instrumented indentation: Advances in understanding and refinements to methodology," *Journal of Materials Research*, vol. 19, pp. 3-20, 2004.
- [168] S. Suresh, *et al.*, "The frictional sliding response of elasto-plastic materials in contact with a conical indenter," *International Journal of Solids and Structures*, vol. 44, pp. 1970-89, 2007.
- [169] B. D. Cullity, *Elements of X-ray diffraction, 2nd edition*. London, UK: Addison-Wesley, 1978.
- [170] C. Verdon, *et al.*, "A study of high velocity oxy-fuel thermally sprayed tungsten carbide based coatings. Part 1. microstructures," *Mater. Sci. Eng. A, Struct. Mater., Prop. Microstruct. Process.*, vol. A246, pp. 11-24, 1998.
- [171] J. Williams, *et al.*, "Ball valves with nanostructured titanium oxide coatings for high-pressure acid-leach service: development to application," in *Pressure Hydrometallurgy*, Banff, Canada, 2004, pp. 663-681.
- [172] D. F. Shaw and R. E. Walter, "How FCCU trickle valves affect catalyst losses," in *AIChE Spring National Meeting*, Orlando, FL, United states, 2006, p. Paper # 41770.
- [173] D. H. E. Jacobson, *et al.*, "Effect of temperature on friction and galling of laser processed Norem 02 and Stellite 21," *Wear*, vol. 255, pp. 498-503, 2003.
- [174] G. E. Kim, *et al.*, "Thermal spray coatings for ball valves used in Nickel/Cobalt pressure acid leaching," in *International Spray Show 2000 Conference*, Montreal, Canada, 2000, pp. 1149-1153.
- [175] A. Scrivani, *et al.*, "A contribution to the surface analysis and characterisation of HVOF coatings for petrochemical application," *Wear*, vol. 250, pp. 107-113, 2001.

- [176] J. Vetter, *et al.*, "Surface treatment selections for automotive applications," *Surface and Coatings Technology*, vol. 200, pp. 1962-1968, 2005.
- [177] J. A. Picas, *et al.*, "HVOF coatings as an alternative to hard chrome for pistons and valves," *Wear*, vol. 261, pp. 477-484, 2006.
- [178] G. Bolelli, *et al.*, "Mechanical and tribological properties of electrolytic hard chrome and HVOF-sprayed coatings," *Surface and Coatings Technology*, vol. 200, pp. 2995-3009, 2006.
- [179] C. Martini, *et al.*, "Sliding and abrasive wear behaviour of boride coatings," *Wear*, vol. 256, pp. 608-613, 2004.
- [180] E. Bousser, *et al.*, "Effect of microstructure on the erosion resistance of Cr-Si-N coatings," *Surface and Coatings Technology*, vol. 203, pp. 776-780, 2008.
- [181] T. Sahraoui, *et al.*, "Structure and wear behaviour of HVOF sprayed Cr₃C₂-NiCr and WC-Co coatings," *Materials Science and Technology and Design*, vol. 24, pp. 309-313, 2003.
- [182] D. Facchini, *et al.*, "Nanostructured metals and alloys - use of nanostructured cobalt phosphorus as a hard chrome alternative for functional applications," *Galvanotechnik*, vol. 100, pp. 523-34, 2009.
- [183] S. Beskri, "Caractérisation d'un placage de cobalt-phosphore nanocristallin," Master, Engineering Physics, Ecole Polytechnique - Université de Montréal, Montreal, 2008.
- [184] Y. Zhuk, "Thick nano-structured CVD coating Hardide as enabler for engineering systems in extreme wear and erosion conditions," ed, 2007.
- [185] G. Bolelli, *et al.*, "HVOF-sprayed WC-Co as hard interlayer for DLC films," *Surface and Coatings Technology*, vol. 203, pp. 699-703, 2008.
- [186] K. N. Lee, *et al.*, "Upper temperature limit of environmental barrier coatings based on mullite and BSAS," *Journal of the American Ceramic Society*, vol. 86, pp. 1299-306, 2003.
- [187] C. P. Bergmann, *et al.*, "HVOF-coatings against high temperature erosion (~300°C) by coal fly ash in thermoelectric power plant," *Materials & Design*, vol. 27, pp. 236-242, 2006.
- [188] J. R. Davis, *Handbook of thermal spray technology*. Materials Park, OH: ASM International, 2004.

- [189] S. Wirojanupatump, *et al.*, "The influence of HVOF powder feedstock characteristics on the abrasive wear behaviour of $\text{Cr}_x\text{C}_y\text{-NiCr}$ coatings," *Wear*, vol. 249, pp. 829-837, 2001.
- [190] S. Matthews, *et al.*, "Long-term carbide development in High-Velocity Oxygen Fuel/High-Velocity Air Fuel $\text{Cr}_3\text{C}_2\text{-NiCr}$ coatings heat treated at 900 °C," *J. Therm. Spray Technol.*, vol. 13, pp. 526-36, 2004.
- [191] T. A. Taylor, "Phase stability of chrome-carbide Ni-Cr coatings in low-oxygen environments," in *Proceedings of the 2nd Conference on Structure/Property Relationships in Thick Films and Bulk Coatings, 10-12 Feb. 1975, USA, 1975*, pp. 790-4.
- [192] S. Matthews, *et al.*, "Microhardness variation in relation to carbide development in heat treated $\text{Cr}_3\text{C}_2\text{-NiCr}$ thermal spray coatings," *Acta Mater.*, vol. 51, pp. 4267-77, 2003.
- [193] V. N. Shukla, *et al.*, "Comparison of tribological behavior of $\text{Cr}_3\text{C}_2\text{/NiCr}$ coatings deposited by different thermal spray techniques: a review," *Inter. J. Mater. Sci. Eng.*, vol. 2, pp. 1-2, 2011.
- [194] X. M. Li, *et al.*, "Impact wear performances of $\text{Cr}_3\text{C}_2\text{-NiCr}$ coatings by plasma and HVOF spraying," *Wear*, vol. 202, pp. 208-214, 1997.
- [195] G. Barbezat, *et al.*, "Abrasion, erosion and scuffing resistance of carbide and oxide ceramic thermal sprayed coatings for different applications," *Wear*, vol. 162-64, pp. 529-537, 1993.
- [196] S. Matthews, *et al.*, "The role of microstructure in the high temperature oxidation mechanism of $\text{Cr}_3\text{C}_2\text{-NiCr}$ composite coatings," *Corros. Sci.*, vol. 51, pp. 1172-1180, 2009.
- [197] J. M. Guilemany, *et al.*, "Role of heat treatments in the improvement of the sliding wear properties of $\text{Cr}_3\text{C}_2\text{-NiCr}$ coatings," *Surface and Coatings Technology*, vol. 157, pp. 207-213, 2002.
- [198] J. M. Guilemany, *et al.*, "Microstructural examination of HVOF chromium carbide coatings for high-temperature applications," *Journal of Thermal Spray Technology*, vol. 5, pp. 483-489, 1996.
- [199] S. Matthews, *et al.*, "Erosion of oxide scales formed on $\text{Cr}_3\text{C}_2\text{-NiCr}$ thermal spray coatings," *Corros. Sci.*, vol. 50, pp. 3087-3094, 2008.
- [200] N. K. Othman, *et al.*, "Effect of water vapour on cyclic oxidation of Fe-Cr alloys," *Materials and Corrosion*, vol. 62, pp. 496-503, 2011.

- [201] P. Berthod and L. Aranda, "Thermal expansion behaviour of ternary nickel-based, cobalt-based, and iron-based alloys containing very high fractions of carbides," *ISRN Metallurgy*, vol. 2012, 2012.
- [202] H.-J. Kim, *et al.*, "Assessment of wear performance of flame sprayed and fused Ni-based coatings," *Surface and Coatings Technology*, vol. 172, pp. 262-269, 2003.
- [203] L. M. Berger, *et al.*, "Microstructure and Properties of HVOF-Sprayed WC-(W,Cr)₂C-Ni Coatings," *J. Therm. Spray Technol.*, vol. 17, pp. 395-403, 2008.
- [204] Y. Ishikawa, *et al.*, "Sliding wear properties of HVOF sprayed WC-20%Cr₃C₂-7%Ni cermet coatings," *Surface and Coatings Technology*, vol. 201, pp. 4718-4727, 2007.
- [205] L. M. Berger, *et al.*, "Influence of feedstock powder characteristics and spray processes on microstructure and properties of WC-(W,Cr)₂C-Ni hardmetal coatings," *Surface and Coatings Technology*, vol. 205, pp. 1080-1087, 2010.
- [206] G.-L. Hou, *et al.*, "Microstructure and high-temperature friction and wear behavior of WC-(W,Cr)₂C-Ni coating prepared by High Velocity Oxy-Fuel spraying," *Surface and Coatings Technology*, vol. 206, pp. 82-94, 2011.
- [207] R. A. Miller and C. E. Lowell, "Failure mechanisms of thermal barrier coatings exposed to elevated temperatures," *Thin Solid Films*, vol. 95, pp. 265-273, 1982.
- [208] M. Kaur, *et al.*, "High-temperature behavior of a High-Velocity Oxy-Fuel sprayed Cr₃C₂-NiCr coating," 101 Philip Drive, Assinippi Park, Norwell, MA 02061, United States, 2012, pp. 2979-2993.
- [209] L. Vernhes, *et al.*, "HVOF Coating case study for power plant process control ball valve application," *Journal of Thermal Spray Technology*, vol. 22, pp. 1184-1192, 2013.
- [210] K. Parker, "Cladding with high power diode lasers," *Welding and Cutting*, vol. 11, pp. 288-289, 2012.
- [211] L. Vernhes, *et al.*, "Alternatives for hard chromium plating: Nanostructured coatings for severe-service valves," *Materials Chemistry and Physics*, vol. 140, pp. 522-528, 2013.
- [212] J. Kamminga, *et al.*, "Science and application of duplex coatings," in *Proceedings of the annual technical conference-society of vacuum coaters*, 2005, pp. 566-574.
- [213] E. Bemporad, *et al.*, "Modelling, production and characterisation of duplex coatings (HVOF and PVD) on Ti-6Al-4V substrate for specific mechanical applications," *Surface and Coatings Technology*, vol. 201, pp. 7652-7662, 2007.

- [214] T. Michler, *et al.*, "Properties of duplex coatings prepared by plasma nitriding and PVD Ti-C: H deposition on X20Cr13 ferritic stainless steel," *Thin Solid Films*, vol. 322, pp. 206-212, 1998.
- [215] G. Park, *et al.*, "Effect of plasma nitriding and nitrocarburizing on HVOF-sprayed stainless steel coatings," *Journal of Thermal Spray Technology*, vol. 22, pp. 1366-1373, 2013.
- [216] G. Bolelli, *et al.*, "HVOF-sprayed WC-Co as hard interlayer for DLC films," *Surface and Coatings Technology*, vol. 203, pp. 699-703, 2008.
- [217] G. Bolelli, *et al.*, "Wear and corrosion behaviour of HVOF WC-CoCr/CVD DLC hybrid coating systems deposited onto aluminium substrate," *Surface and Coatings Technology*, vol. 205, pp. 4211-4220, 2011.
- [218] Y. Zhuk, "Thick nano-structured CVD coating Hardide as enabler for engineering systems in extreme wear and erosion conditions," *Materials science and technology - Association for iron and steel technology*, vol. 3, pp. 1970-1982, 2007.
- [219] H. Zhang, *et al.*, "Laser cladding of Colmonoy 6 powder on AISI316L austenitic stainless steel," *Nuclear Engineering and Design*, vol. 240, pp. 2691-2696, Oct 2010.
- [220] Q. Y. Hou, *et al.*, "Microstructure and wear characteristics of cobalt-based alloy deposited by plasma transferred arc weld surfacing," *Surface and Coatings Technology*, vol. 194, pp. 238-243, 2005.
- [221] P. Ctibor and M. Hrabovsky, "Plasma sprayed TiO₂: The influence of power of an electric supply on particle parameters in the flight and character of sprayed coating," *Journal of the European Ceramic Society*, vol. 30, pp. 3131-3136, 2010.
- [222] D. J. Greving, *et al.*, "Effects of coating thickness and residual stresses on the bond strength of ASTM C633-79 thermal spray coating test specimens," *Journal of Thermal Spray Technology*, vol. 3, pp. 371-378, 1994.
- [223] L. T. Kabacoff, "Nanoceramic coatings exhibit much higher toughness and wear resistance than conventional coatings," *The AMPTIAC Newsletter*, vol. 6, pp. 37-42, 2002.
- [224] ASTM, "G40-13, Standard terminology relating to wear and erosion," ed. West Conshohocken, PA: ASTM International, 2013.

- [225] K. Holmberg, *et al.*, "Tribological contact analysis of a rigid ball sliding on a hard coated surface: Part II: Material deformations, influence of coating thickness and Young's modulus," *Surface and Coatings Technology*, vol. 200, pp. 3810-3823, 2006.

APPENDIX A NANOSTRUCTURED AND CONVENTIONAL Cr_2O_3 , TiO_2 AND TiO_2 - Cr_2O_3 THERMAL SPRAYED COATINGS FOR METAL- SEATED BALL VALVE APPLICATIONS IN HYDROMETALLURGY

A.1. Introduction

In collaboration with the NRC and Polytechnique Montréal, Velan undertook a detailed characterization project in order to assess the mechanical and tribological resistance of promising ceramic coatings for hydrometallurgy applications, including a novel nanostructured n- TiO_2 - Cr_2O_3 blend. All test results were compiled to facilitate Velan's selection of the most appropriate coating to optimize MSBV performance in POx and HPAL applications⁴.

Over the last two decades, metal-seated ball valves (MSBVs) have become the industry standard for hydrometallurgy applications. They ensure tight, reliable shut-off, a critical service that facilitates maintenance and contributes to a safe working environment. The typical MSBV design for hydrometallurgy applications consists of a floating ball in contact with a fixed seat. The ball and seats consist of either titanium or duplex stainless steel substrates protected by a ceramic coating. The primary function of the ceramic coating is to enhance the load-carrying capacity and tribological performance of the base material, thus extending the in-service life of the equipment, especially during ball motion phases.

Twenty years ago, conventional Cr_2O_3 applied by air plasma spraying (APS) was the preferred coating for protecting MSBVs from the extreme abrasion, pressure, and elevated temperature inherent to the pressure oxidation (POx) recovery process used in gold processing, in which gold ore is mixed with oxygen and sulfuric acid in an autoclave. Over time and based on field experiments, silicon dioxide (SiO_2) and titanium dioxide (TiO_2) were added to the original Cr_2O_3 blend to improve the ductility and toughness. Velan's Cr_2O_3 blend has proven effective in gold extraction at sites such as the NERCO Con Mine (Canada) and the Barrick Goldstrike and Lone

⁴ This appendix is based on a working paper coauthored with Craig Bekins and Nicolas Lourdel from Velan, Rogerio S. Lima and Dominique Poirier from National Research Council of Canada, and Duanjie Li and Jolanta E. Klemberg-Sapieha from Polytechnique Montréal.

Tree mines (USA). The Lihir and Porgera gold mines (Papua New Guinea) have also reported good results with Velan's Cr_2O_3 blend applied to MSBVs [86].

Similar to POx, high-pressure acid leaching (HPAL) is used in the nickel recovery process, whereby laterite ore is leached in a sulfuric acid environment in an autoclave at 4.1 bar (600 psi) and temperatures above 240 °C (464 °F). Unlike POx, HPAL operates at high pressure, which, combined with a higher chloride content, produces a more corrosive environment (e.g., titanium is susceptible to crevice corrosion in HPAL). Based on Velan's experience with different coating blends at Falconbridge Mines (Canada), the Cr_2O_3 blend optimized for POx corrodes prematurely when used in HPAL. Because it is relatively inert in this environment, TiO_2 would appear to be a promising choice for HPAL [7]. However, the mechanical and tribological performance of conventional TiO_2 are significantly lower than those of Cr_2O_3 , resulting in higher wear rates, as observed by Velan at the Cawse and Murin-Murin nickel mines (Australia).

The industry has been working to optimize coating solutions for HPAL [171]. Several options for mitigating corrosion have been considered and tested by various companies, with generally unsuccessful results. Attempts included the use of intermediate bond coats, such as gold and tantalum, placed between the base material and the Cr_2O_3 top coat. One engineering firm used a nanostructured TiO_2 coating, which has worked reasonably well at Ravensthorpe (Australia) and Ramu (Papua New Guinea) [84, 85]. Meanwhile, Velan developed a proprietary ceramic blend containing TiO_2 and Cr_2O_3 , designed to obtain the corrosion resistance of pure TiO_2 and the tribological performance of Cr_2O_3 . This coating has demonstrated superior performance in several HPAL projects, including Coral Bay (The Philippines), and has performed satisfactorily at most recent installations, such as Goro (New Caledonia) and Ambatovy (Madagascar) [86]. All critical isolation valves installed at the recent Taganito (The Philippines) project also used this optimized TiO_2 - Cr_2O_3 blend.

Section 2 describes the experimental procedures, including the materials and characterization methods. Section 3 presents the research findings and their analysis. Section 4 presents the conclusions and some directions for further research.

A.2. Experimental

A.2.1. Materials

A.2.1.1. Base Material

All coatings were applied onto titanium grade 5 coupons (ASTM B348) that were previously grit blasted (Al_2O_3 – grit 24). A nominal coating thickness of 0.020in (500 μm) was targeted.

A.2.1.2. Powder Materials

The following powder materials were selected based on a literature review and field experience:

- 1) Cr_2O_3 (Velan's proprietary blend),
- 2) $\text{TiO}_2\text{-Cr}_2\text{O}_3$ (Velan's proprietary blend),
- 3) n- TiO_2 (supplied by Millydine),
- 4) n- $\text{TiO}_2\text{-Cr}_2\text{O}_3$ (Velan's proprietary blend).

Cr_2O_3 and $\text{TiO}_2\text{-Cr}_2\text{O}_3$ are currently Velan's proprietary ceramic coatings for hydrometallurgy.

The authors consider selected n- TiO_2 as the finest TiO_2 available on the market. This powder is formed from nanosize constituents that are agglomerated and sintered into larger particles to allow spraying. Figure A-1 shows the n- TiO_2 powder microstructure, X-ray diffraction (XRD), and particle size distribution measured by laser diffraction.

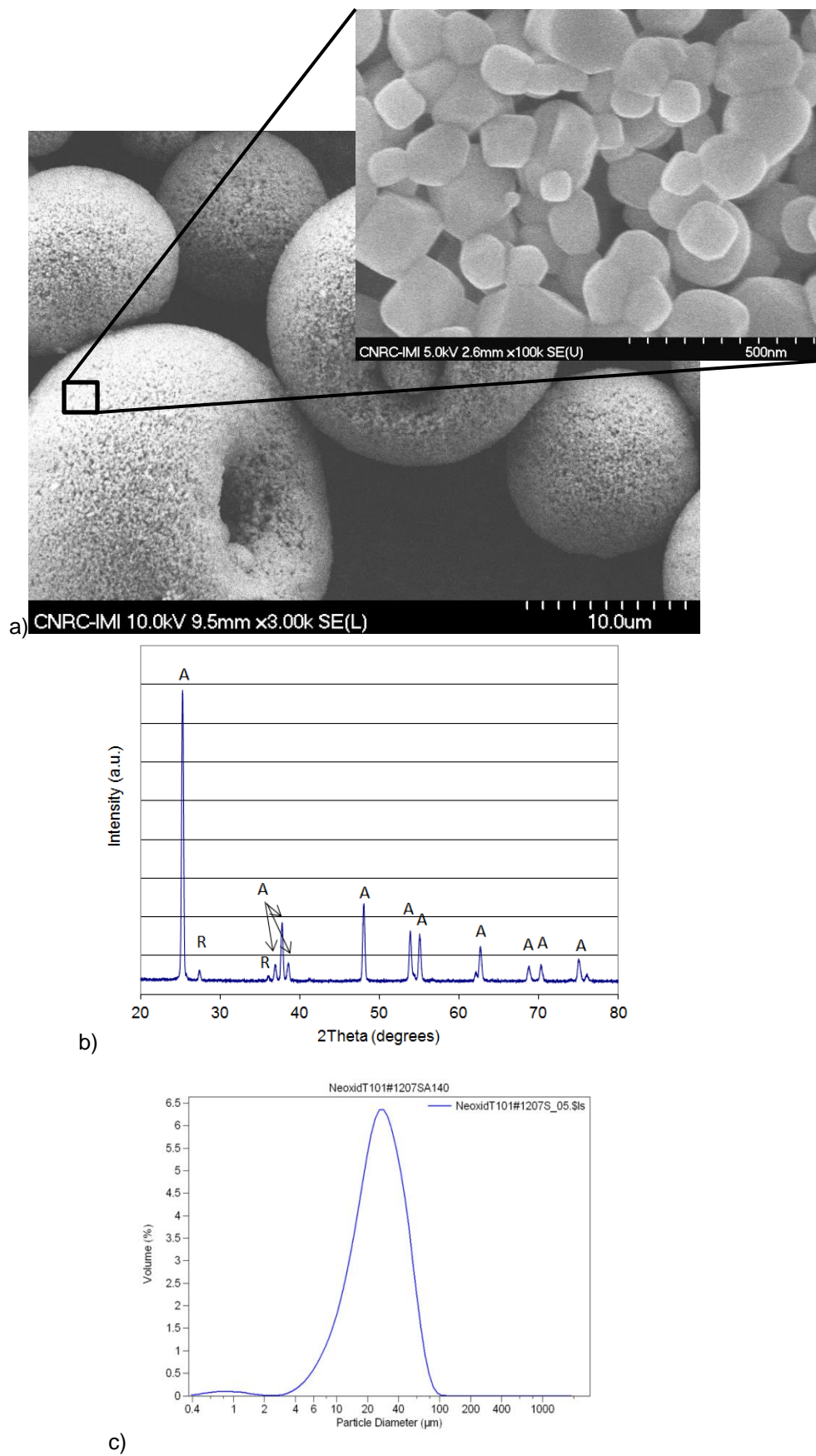


Figure A-1: n-TiO₂ powder characteristics: (a) SEM micrographs – A: anatase, R: rutile, (b) XRD pattern, and (c) particle size distribution – logarithmic scale

A novel blend of n-TiO₂ and Cr₂O₃ was specifically prepared by the authors for this project. The n-TiO₂ powder (supplied by Millydine) was mixed with Metco 106, a fused, sintered, and crushed Cr₂O₃ powder.

A.2.2. Deposition Techniques

High velocity oxygen fuel (HVOF) and APS are the two dominant thermal spray processes used to apply these coatings. APS, at an in-flight particle temperature ~2,600 °C (~4,700 °F), is more appropriate for applying Cr₂O₃ (melting point ~2,350 °C / 4,260 °F) compared to HVOF (maximum in-flight particle temperature ~2,300 °C / 4,172 °F). Consequently, all coatings were deposited using APS.

Velan's proprietary blends were deposited using an SG100 torch (Praxair Surface Technologies, USA), as presented in Table A.1.

Table A.1: Spraying parameters.

	Cr ₂ O ₃	TiO ₂ - Cr ₂ O ₃	n-TiO ₂	n-TiO ₂ - Cr ₂ O ₃
Torch	SG-100	SG-100	Mettech Axial III	Mettech Axial III
Ar flow (lpm)	53	53	37.5	62.5
H ₂ flow (lpm)	<i>Confidential</i>		37.5	62.5
N ₂ /He flow (lpm)	41 He	41 He	75 N ₂	125 N ₂
Current (A)	800	800	230*	230*
Voltage (V)	~42	~42	152	205
Power (kW)	33.6	33.6	105	141
Net Power (kW) or Enthalpy (kJ/L)	<i>Confidential</i>		15.0 kJ/L	18.2 kJ/L
Nozzle	730 Anode / 129 Cathode	730 Anode / 129 Cathode	3/8in	3/8in
Spraying Distance (cm)	6.35	6.35	14	14
Feedrate (g/min)	~30	~30	18	18
Ar Carrier Gas flow (lpm)	5	5	9	9
In-flight Temperature (°C)	<i>Confidential</i>		2578±166**	2590±258**
In-flight Velocity (m/s)			269±45**	457***±91**

*Current per electrode set – 3 electrode sets in the torch.

**The standard deviation corresponds to the sample distribution, not the experimental error.

***Approximation; velocity higher than the standardized range.

The n-TiO₂ and n-TiO₂-Cr₂O₃ coatings were deposited using a high power Mettech Axial III APS torch. The optimal set of spraying parameters for sliding wear performance of the n-TiO₂

feedstock was determined in a previous NRC study and used for the present study. The gas flows, current, and spraying distances for the n-TiO₂-Cr₂O₃ powder blend were varied to produce coatings with different structures and properties (preliminary trials). The parameter set that produced the hardest and toughest coating was selected for coating production.

All spraying parameters are presented in Table A.. In-flight particle temperature and velocity were measured with a DPV 2000 thermal spray sensor (Tecnar Automation, Canada).

A.2.3. Characterization techniques

A.2.3.1. Microstructure

Coating microstructures were obtained using SEM (JSM-6100 microscope, JEOL, Japan) or back-scattered electron (BSE) imaging (FE-SEM S4700 microscope, Hitachi, Japan). EDS analyses were performed using a JSM-840 SEM microscope (JEOL, Japan). Coatings were sectioned with a coolant-assisted diamond wheel and then cold-vacuum mounted in an epoxy resin. Cross-sections were then ground and polished using standard metallographic preparation procedures

A.2.3.2. Mechanical Property Characterization

Microhardness and shear strength were determined using microhardness indentation testers and universal tensile testing equipment, respectively.

Microhardness was measured on polished coating cross-sections with a Micromet II Tester (Buehler, USA) equipped with a Vickers tip under a 300 gf load. A minimum of 12 indentations were performed on each specimen (straight line pattern at the center of the coating cross-section), and the highest and lowest values were removed from the dataset.

Coating adhesion to the Ti substrate was assessed with shear tests (ASTM F1044). An Instron 5582 Universal Testing Machine (Instron, Canada) was used to determine the maximum shear loads required to obtain sample separation.

A.2.3.3. Tribological Behavior Assessment

Wear resistance of the coatings under different conditions such as sliding wear and abrasion were measured by standard pin-on-disc tests and abrasion tests, respectively. Galling resistance was measured using a custom-designed automated galling tester.

A custom-made pin-on-disc tribometer was used to assess the sliding wear behavior of the coatings. A normal load of 25 N was applied to a tungsten carbide ball (4.75 mm diameter) used as a counterpart material. A new ball was used for each test. The diameter of the wear track ring was 7 mm and the rotation speed was 546 revolutions per minute (rpm). This results in a linear speed of 20 cm/s (7.9 in/s). The coefficient of friction COF was recorded every second during the test. The wear rate K was assessed using the formula $K=V/(F \times s)$, where V is the worn volume, F is the normal load, and s is the sliding distance. Pin-on-disc wear track profiles were determined using a Sloan Dektak II profilometer, and the wear track morphology was examined by optical microscopy (Nikon Epiphot 200).

The dry abrasion resistance of coatings was tested with the dry sand/rubber wheel abrasion test (ASTM G65 / procedure D-modified, 45 N, 2000 wheel revolutions, Durometer A-60 wheel). Two samples were tested for each coating type. Prior to testing, sample surfaces were ground with a diamond wheel to produce a surface finish of approximately 0.2 to 0.3 μm . Sample volume loss due to testing was measured with an optical profilometer.

The wet abrasion resistance of the coatings was tested with the wet sand/rubber wheel and measured according to a modified ASTM G105-02 procedure using a Falex[®] sand abrasion test machine and controlled slurry. For each coating type, one rectangular-shaped specimen (1 in x 3 in x 0.5 in) was submitted to a 1000-cycle run at 22 N normal load using a 7 in diameter and an A-60 Durometer rubber wheel at a nominal speed of 245 rpm. The slurry mixture consisted of rounded quartz grain sand AFS 50/70 and deionized water at a ratio of 0.940 kg water / 1.500 kg sand. Prior to testing, sample surfaces were ground with a diamond wheel to produce a surface finish of approximately 0.2 to 0.3 μm . Sample volume loss due to testing was measured with an optical profilometer.

Galling resistance was measured using a custom-designed automated galling tester developed by Engineered Valve International Inc. (Glens Falls, USA) in collaboration with Velan (see Figure A-2). The test involves quarter-turn rotating an annular coated specimen (12.7 mm inside dia x 31.7 mm outside dia) against a second annular coated fixed specimen under controlled contact pressure, stroke motion, and temperature conditions.

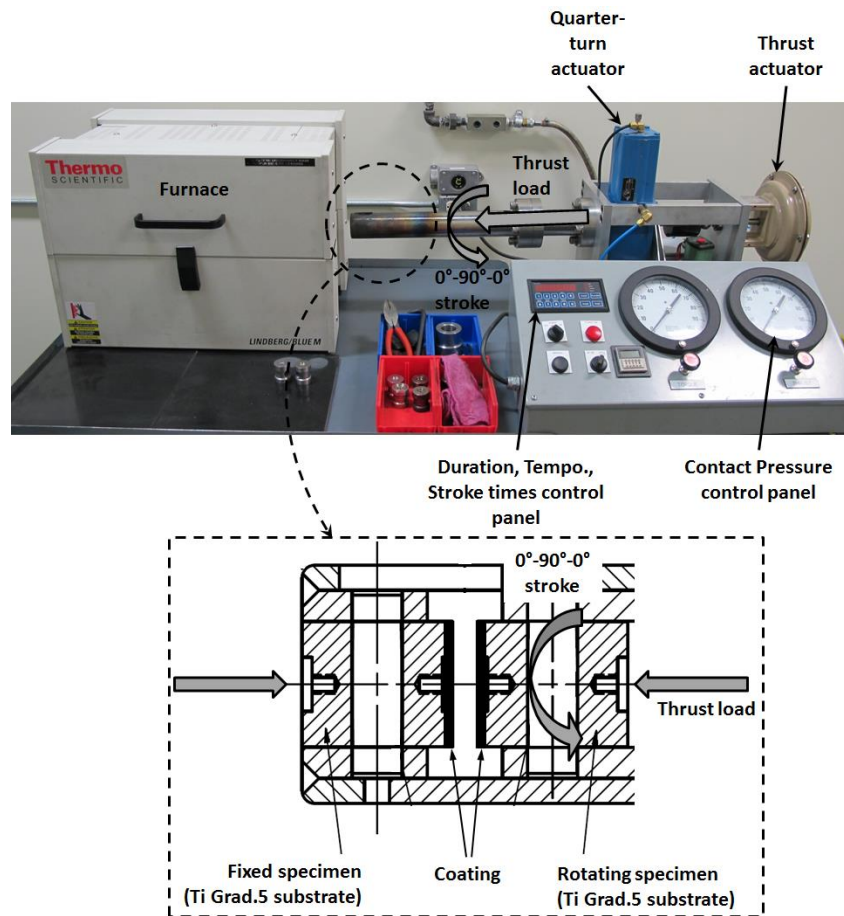


Figure A-2: Custom-designed automated variable temperature galling tester.

Contact load and stroke motion were applied with a pneumatic thrust actuator (Samson 3277) and a quarter-turn actuator (Metso B1CU6/20L), respectively, and temperature was adjusted with a radiation tube furnace (Lindberg Blue M Tube Furnace) coupled with a thermocouple Type K probe tack-welded onto one specimen. All test parameters were controlled from a centralized panel. Prior to testing, the coated surface of each specimen was prepared by manual polishing with several grades of polishing cloths (P320–P1200 grit) using a thin buffer of commercial machinery oil and then inspected. Specimens presenting a surface roughness R_a below $0.3 \mu\text{m}$,

flatness below 0.1 mm, and specimen mass ± 0.5 mg were selected for wear pattern tests. For each coating type, one set of two self-mated specimens was tested according to the procedure described in Table A.2. Testing was halted when a coated specimen displayed a significant wear pattern (e.g., micro-welding, scoring). The test procedure was repeated for each coating type to allow ranking the materials for galling resistance and total mass loss over a given period.

Table A.2: Variable temperature galling test procedure.

Step	Duration (no. of cycles)	Specimen temperature, °C (°F)	Nominal contact pressure, MPa (psi)	No. of cycles per minute	0° → 90° and 90° → 0° stroke times (s)	Temporization at 0° and 90° position (s)
1	50	R.T.	6.9 MPa \pm 0.3 (1,000 \pm 50)	0.2	10 \pm 0.5	140
2	50	220 \pm 7 * (428 \pm 12)	6.9 MPa \pm 0.3 (1,000 \pm 50)	0.2	10 \pm 0.5	140
3	50	220 \pm 7 * (428 \pm 12)	10.3 MPa \pm 0.3 (1,500 \pm 50)	0.2	10 \pm 0.5	140
4	50	220 \pm 7 * (428 \pm 12)	13.8 MPa \pm 0.3 (2,000 \pm 50)	0.2	10 \pm 0.5	140

*: Heating ramps are adjusted to 204 °C (400 °F) per hour.

A.3. Results and discussion

A.3.1. Microstructure

The microstructures of the Cr₂O₃, TiO₂, n-TiO₂, and n-TiO₂-Cr₂O₃ coatings are shown in Figure A-3. The two phases present in the coatings with the blend powder feedstock are Cr₂O₃ (light grey) and TiO₂ (dark grey), respectively. All coatings showed low porosity. The fine cracks seen in the particles and at particle boundaries are thought to be formed due to quenching. The large cracks are typically formed as stress relief due to stresses from CTE mismatch with the substrate and/or residual stresses within the coating.

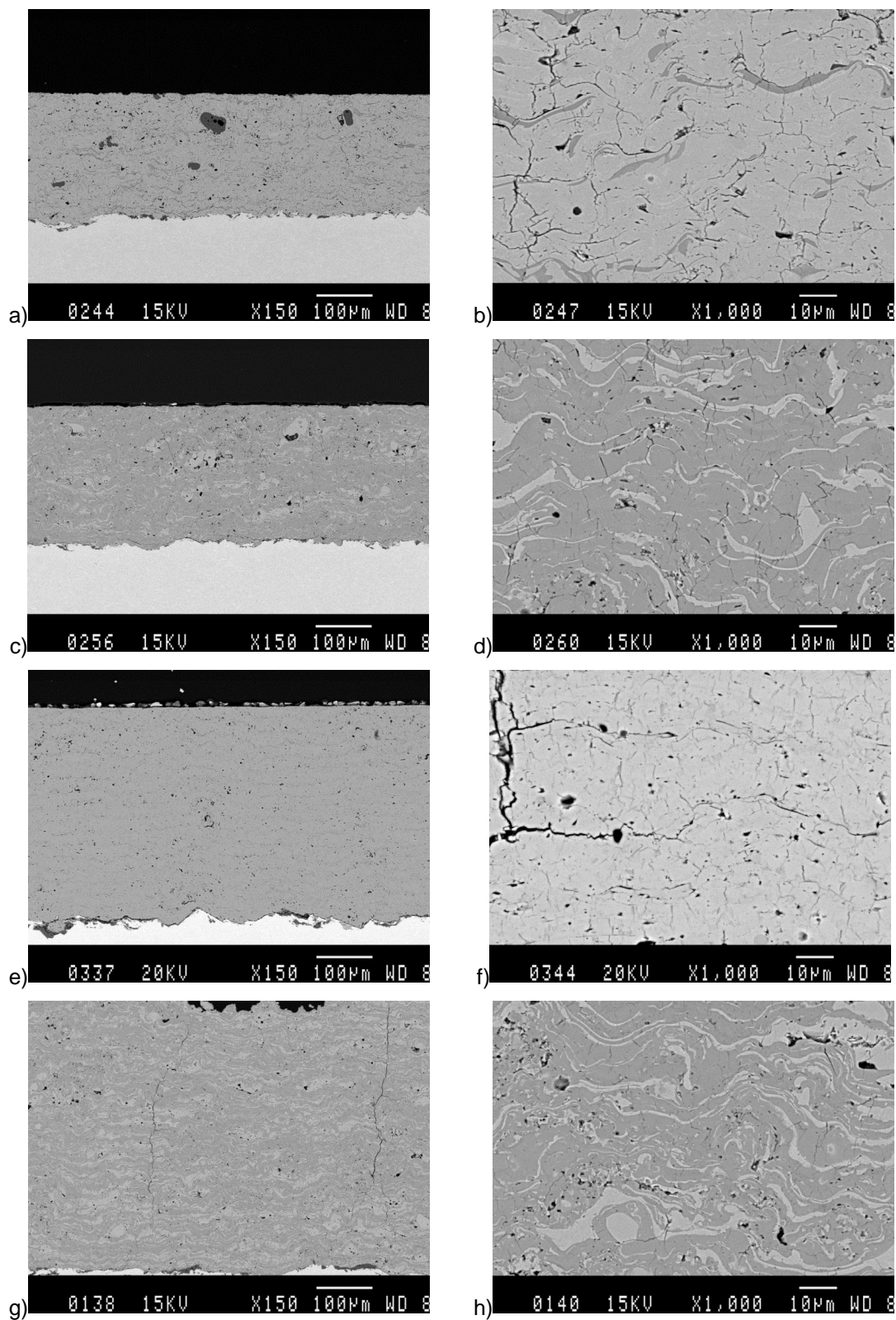


Figure A-3: Coating microstructures: Cr_2O_3 at (a) 150X and (b) 1000X. $\text{TiO}_2\text{-Cr}_2\text{O}_3$ at (c) 150X and (d) 1000X. n-TiO_2 at (e) 150X and (f) 1000X. $\text{n-TiO}_2\text{-Cr}_2\text{O}_3$ at (g) 150X and (h) 1000X.

EDS spectra acquired from the four different coatings are shown in Figure A-4. The chemical composition of each coating is confirmed.

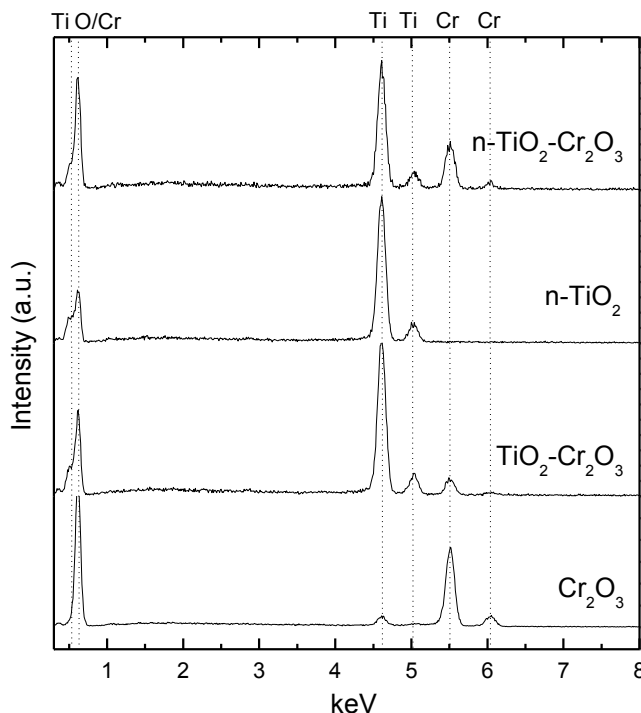


Figure A-4: EDS spectra of the Cr_2O_3 , $\text{TiO}_2\text{-Cr}_2\text{O}_3$, $\text{n-TiO}_2\text{-Cr}_2\text{O}_3$ and $\text{n-TiO}_2\text{-Cr}_2\text{O}_3$ materials.

A.3.2. Microhardness

Microhardness results are presented in Table A.3. As expected, the highest microhardness was achieved when the hardest phase, Cr_2O_3 , was used primarily for the coating. The $\text{n-TiO}_2\text{-Cr}_2\text{O}_3$ coating showed the second highest microhardness.

The improved hardness of $\text{n-TiO}_2\text{-Cr}_2\text{O}_3$ over conventional $\text{TiO}_2\text{-Cr}_2\text{O}_3$ was probably due to the use of the Mettech Axial III torch for spraying. The higher power of the torch together with the high gas flow used provides very high in-flight particle speed, which is known to contribute to overall coating quality [221].

Table A.3: Coating properties.

Coating	Microhardness (HV-300gf, n=10)	Dry Abrasion: Volume loss with ASTM G65 D-mod method(mm3, n=2)	Wet Abrasion: Volume loss with ASTM G105 mod method(mm3, n=2)	Shear Strength (MPa, n=5)
Cr_2O_3	1423 ± 62	17.1 ± 2.1	10.48 ± 0.1	$> 42 \pm 7^d$
$\text{TiO}_2\text{-Cr}_2\text{O}_3$	912 ± 42	20.5 ± 0.5	34.6 ± 0.1	$> 46 \pm 2^b$
n-TiO ₂	729 ± 45	31.6 ± 0.6	43 ± 3.2	36 ± 2^a
n-TiO ₂ -Cr ₂ O ₃	1200 ± 49	7.8 ± 0.6	8.5 ± 0.1	38 ± 5^a

^a Adhesive failure (occurs at bond line with substrate)

^b Epoxy failure (glue)

^c Cohesive failure (failure within the coating)

^d Mixed mode: all or partial failure of the above types.

Please note that it is inconceivable to have interface and epoxy failure without some cohesive failure.

A.3.3. Adhesion

All produced coatings provided good bonding to the substrate. The best coating adhesion in shear was achieved with $\text{TiO}_2\text{-Cr}_2\text{O}_3$. Although the variation in coating adhesion was relatively low, the n-TiO₂ and n-TiO₂-Cr₂O₃ coatings showed lower adhesion, probably due to the greater thickness of these coatings (Table 1). Thicker thermal sprayed coatings typically showed lower adhesion due to the buildup of residual stresses [222].

A.3.4. Tribomechanical properties

A.3.5. Sliding Wear Resistance

Figure A-5 shows the coefficient of friction COF as a function of the sliding distance. In the first 500 m sliding distance, the COFs for the different coatings range from 0.6 to 0.7. After the accommodation period (resulting in the high COF of ~0.65 at the beginning of the wear test for Cr_2O_3), the COF for Cr_2O_3 decreases progressively to reach a stable COF of ~0.5. The COF for the n-TiO₂-Cr₂O₃ coating fluctuates, ranging from ~0.6 to ~0.7 during its relatively long accommodation period, eventually reaching a COF of ~0.6. In comparison, the COFs for the $\text{TiO}_2\text{-Cr}_2\text{O}_3$ and n-TiO₂ coatings increase progressively, from ~0.6 to ~0.7 and from ~0.7 to ~0.8, respectively.

The frictional behavior of the different coatings correlates with their respective wear resistance, as shown in Figure A-6. The wear resistance of the Cr_2O_3 coating shows substantial improvement, at a wear rate of $\sim 5.5 \times 10^{-8} \text{ mm}^3/(\text{N.m})$, whereas the $\text{n-TiO}_2\text{-Cr}_2\text{O}_3$ coating shows a low wear rate of $\sim 1.3 \times 10^{-6} \text{ mm}^3/(\text{N.m})$. In contrast, the $\text{TiO}_2\text{-Cr}_2\text{O}_3$ and n-TiO_2 coatings show wear rates of $\sim 3.73 \times 10^{-5}$ and $\sim 7.6 \times 10^{-5} \text{ mm}^3/(\text{N.m})$, respectively, approximately three orders of magnitude higher than for the Cr_2O_3 coating. This is in agreement with the microscopy observation of the wear tracks after pin-on-disc tests, as shown in Figure A-7: the $\text{TiO}_2\text{-Cr}_2\text{O}_3$ and n-TiO_2 coatings have wide and deep wear tracks. In contrast, the Cr_2O_3 and $\text{n-TiO}_2\text{-Cr}_2\text{O}_3$ coatings show small wear scars on the shallow surface, indicating mild abrasive wear.

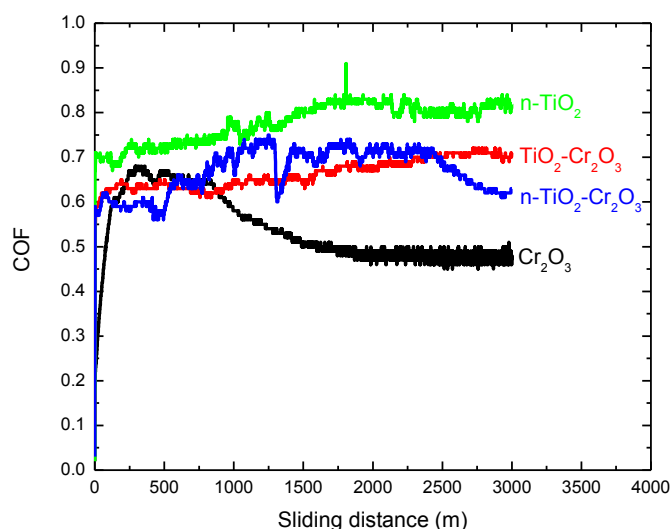


Figure A-5: Coefficient of friction vs. sliding distance for the different coatings.

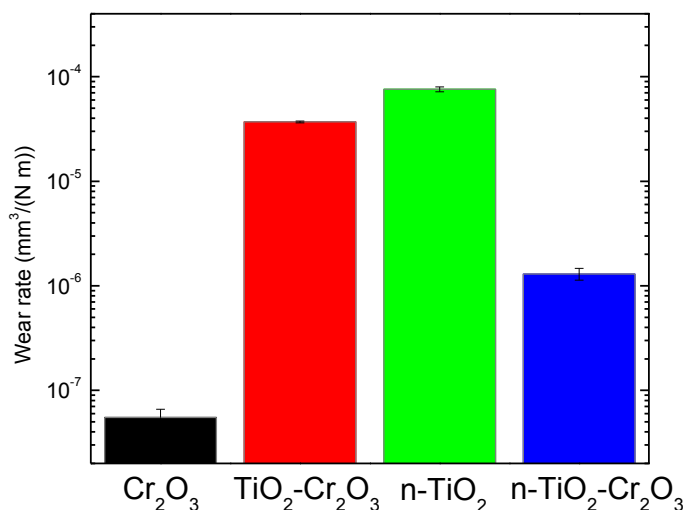


Figure A-6: Wear rate for the different coatings.

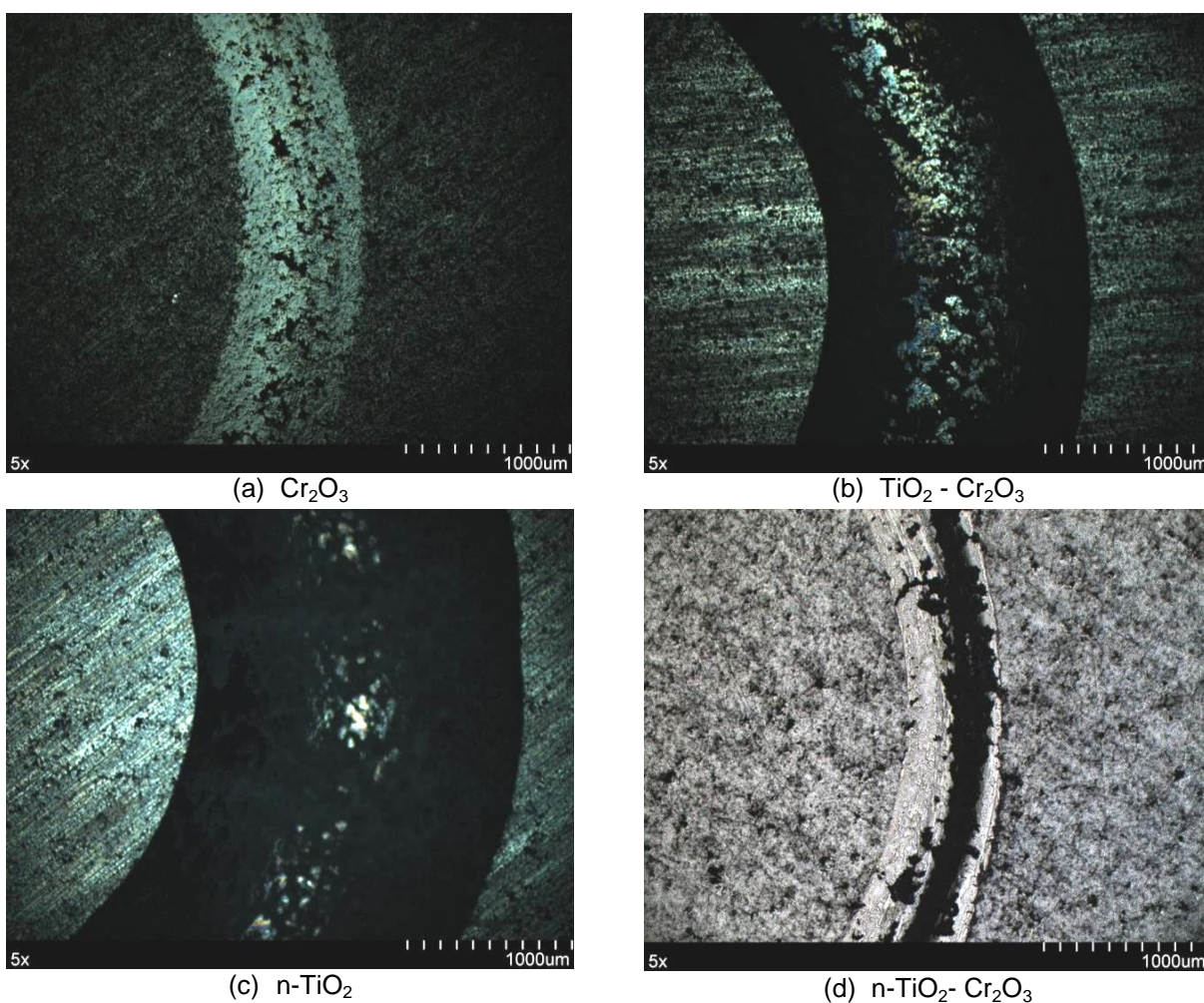


Figure A-7: Wear tracks after pin-on-disc tests at 50X.

A.3.5.1. Dry Sand Abrasion

Table A.3 shows that the best dry abrasion wear performance is achieved with the $\text{n-TiO}_2\text{-Cr}_2\text{O}_3$ coating, most probably due to the use of the Mettech torch combined with the use of the n-TiO_2 and Cr_2O_3 blend. However, improved coating wear performance with added n-TiO_2 was also shown to be due to improved coating toughness [85, 223].

In contrast, the n-TiO_2 coating, which showed the lowest hardness, showed the poorest wear performance. Despite the much higher hardness of the Cr_2O_3 coating, it showed only average wear performance. This disappointing performance is attributed to the brittleness of the Cr_2O_3 material. Wear tracks are shown in Figure A-8.

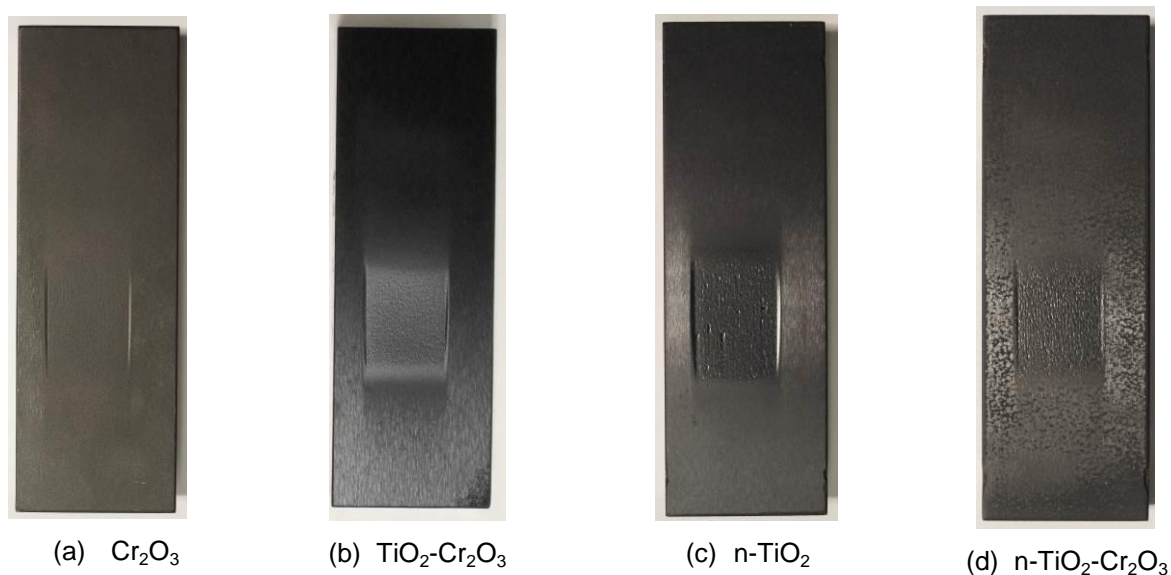


Figure A-8: Wear tracks for specimens after dry abrasion testing.

A.3.5.2. Wet Sand Abrasion

In line with the dry abrasion results, Table A.3 and Figure A-9 show that the n-TiO₂-Cr₂O₃ coating had the best wet abrasion wear performance with an average volume loss $\sim 8.5 \text{ mm}^3$. The Cr₂O₃ coating showed a slightly larger volume loss, and the n-TiO₂ and TiO₂-Cr₂O₃ coating showed the poorest performance and the largest volume loss. Substrate was reached on a small area that should not significantly affect the results.

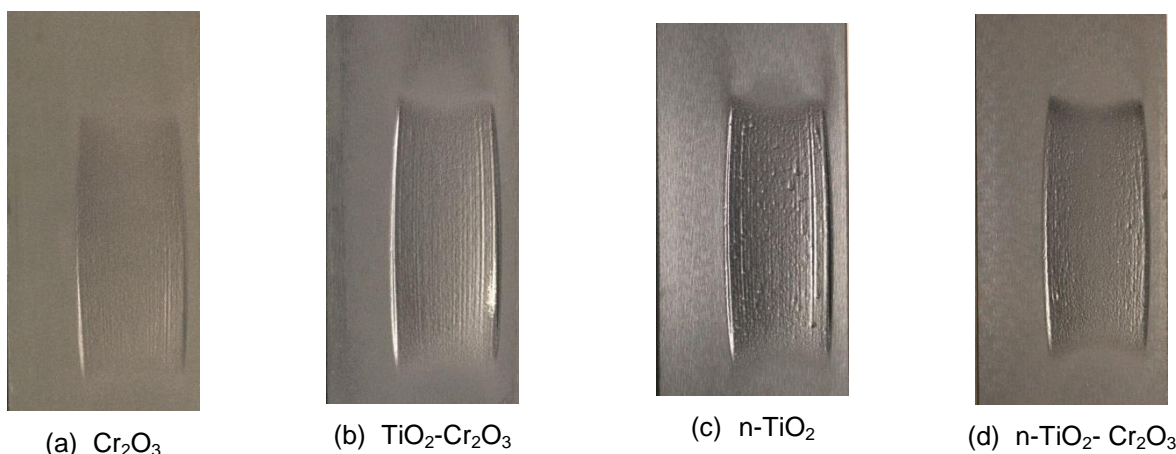


Figure A-9: Wear tracks for specimens after wet abrasion testing.

A.3.5.3. Variable Temperature Galling Resistance

Figure A-10 shows the number of steps prior to observing a significant wear pattern and the total mass loss for the different self-mated specimens (rotating + fixed specimens). Total mass loss was measured between 0 cycles (initial mass) and 100 cycles (i.e., after Step 2).

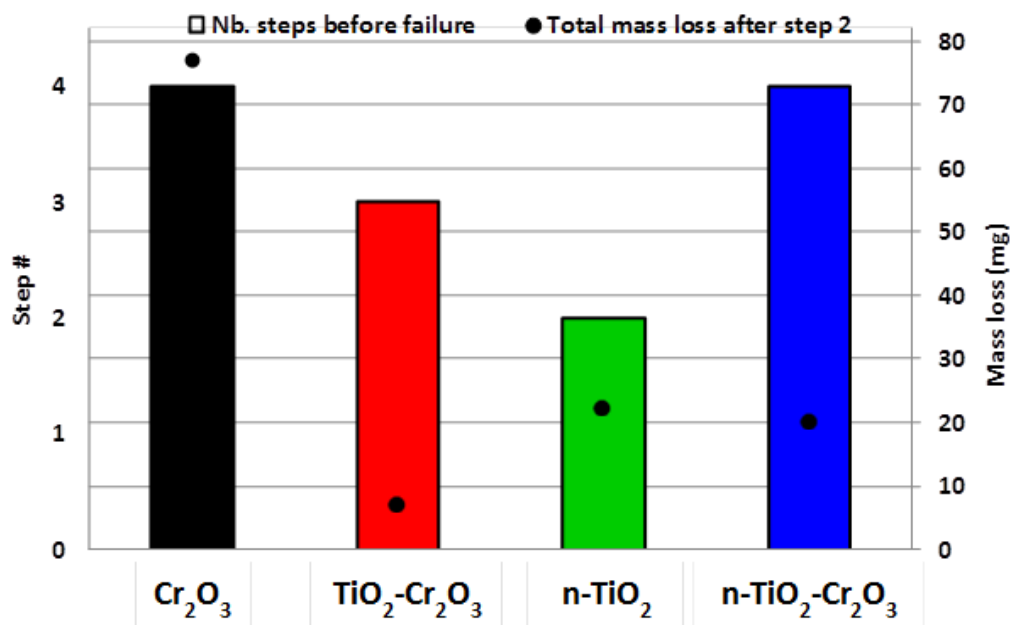


Figure A-10: Galling resistance of self-mated specimens after variable temperature galling resistance. Mass loss is given between 0 (initial mass) and 100 cycles (i.e., after Step 2).

(a) Cr_2O_3 fixed specimen after Step 4(b) Cr_2O_3 rotating specimen after Step 4(c) $\text{TiO}_2\text{-Cr}_2\text{O}_3$ fixed specimen after Step 3(d) $\text{TiO}_2\text{-Cr}_2\text{O}_3$ rotating specimen after Step 3(e) n-TiO_2 fixed specimen after Step 2(f) n-TiO_2 rotating specimen after Step 2(g) $\text{n-TiO}_2\text{-Cr}_2\text{O}_3$ fixed specimen after Step 4(h) $\text{n-TiO}_2\text{-Cr}_2\text{O}_3$ rotating specimen after Step 4

Figure A-11: Wear patterns of specimens after variable temperature galling test.

Figure A-11 shows macro-scale images of the specimens after the variable temperature galling test. The Cr_2O_3 (6-11-a and 6-11-b) and $\text{n-TiO}_2\text{-Cr}_2\text{O}_3$ (6-11-g and 6-11-h) coatings showed the best galling resistance, with the appearance of light material pick-up and scoring during Step 4 (200 cycles / 220 °C / 13.8 MPa). However, the Cr_2O_3 mass loss after 100 cycles (77 mg) was approximately four times higher than that for $\text{n-TiO}_2\text{-Cr}_2\text{O}_3$ (20 mg). In comparison, both the n-TiO_2 (6-11-e and 6-11-f) and $\text{TiO}_2\text{-Cr}_2\text{O}_3$ (6-11-c and 6-11-d) coatings combined moderate galling resistance with low mass loss: galling, micro-welding, and material pick-up at Step 2 (100 cycles / 220 °C / 6.9 MPa) and Step 3 (150 cycles / 220 °C / 10.3 MPa), respectively, with mass loss at below 22 mg after 100 cycles. The Cr_2O_3 coating lost more mass than the other specimens, probably due to brittleness. With the highest number of steps prior to observing a significant wear pattern combined with a low mass loss, the $\text{n-TiO}_2\text{-Cr}_2\text{O}_3$ coating was ranked 1st. The Cr_2O_3 , $\text{TiO}_2\text{-Cr}_2\text{O}_3$, and n-TiO_2 coatings were ranked 2nd, 3rd, and 4th, respectively.

A.4. Conclusions

We assessed the load-carrying capacity and tribological resistance of four ceramic coatings for potential suitability for HPAL.

The Cr_2O_3 ceramic material alone showed the highest hardness and best sliding wear resistance and COF, whereas the n-TiO_2 ceramic material showed the lowest hardness, the poorest wear rate, and the highest COF. As expected, the $\text{Cr}_2\text{O}_3\text{-TiO}_2$ and $\text{n-TiO}_2\text{-Cr}_2\text{O}_3$ blends produced hardness and sliding wear resistance between that for each of the ceramic constituents.

In terms of abrasion, the results are positive and counter-intuitive. The $\text{n-TiO}_2\text{-Cr}_2\text{O}_3$ blends produced superior resistance under both dry and wet abrasion testing compared to the ceramic materials alone. According to a study published by Velan, the high performance of the $\text{TiO}_2\text{-Cr}_2\text{O}_3$ coating was attributed to the optimized balance between the hard and brittle Cr_2O_3 phases and the soft and ductile TiO_2 phases. The results of the present study indicate that the synergy between these two materials produced abrasion performance that exceeded that for each material alone.

With respect to galling, the n-TiO₂-Cr₂O₃ coating ranked first, with the highest number of steps before observing a significant wear pattern and the lowest mass loss. The Cr₂O₃, TiO₂-Cr₂O₃, and n-TiO₂ ranked 2nd, 3rd, and 4th, respectively.

Promisingly, the novel mix of n-TiO₂ and Cr₂O₃ provided consistently superior tribological performance to Velan's proprietary TiO₂-Cr₂O₃ blend. Consequently, this novel blend appears to be a promising evolution of the current TiO₂-Cr₂O₃ blend. Further optimization is needed for commercial application.

Further work is also needed to optimize the surface preparation, spraying procedures, and post-treatment of the novel Cr₂O₃ and n-TiO₂ blend in order to achieve equivalent or better results compared to the current TiO₂-Cr₂O₃ blend, particularly in terms of bond and shear strength. In fact, the current TiO₂-Cr₂O₃ blend showed the highest bond and shear strength of all the materials, including nanocoatings. For instance, it would be useful to develop an HVOF process for TiO₂-Cr₂O₃ spraying. The challenge in this case would be to ensure that the Cr₂O₃ particles melt in order to avoid particle rebound when impacting the substrate, as well as erosion of the deposited TiO₂ layer by the same particles.

Further work is also needed to secure the supply chain and to develop quality standards for this novel material in order to prevent production delays and/or quality issues. Corrosion tests will also be required to fully assess material corrosion performance using different types of sealant.

In the meantime, our results indicate that TiO₂-Cr₂O₃ provides the best overall tribological performance compared to the other tested ceramics, namely Cr₂O₃ and n-TiO₂.

A.5. Acknowledgements

The authors wish to thank Rabih Matar (Velan), Jean-Claude Tremblay (NRC), Michel Thibodeau (NRC), and David De Lagrave (NRC) for their technical support, as well as David

Lee (Kennametal Stellite) for useful discussions. Finally, we greatly appreciate Velan's interest in and support of this research.

APPENDIX B TRIBOLOGY TERMS

Active Standard G40-13, published by ASTM International, provides the terms and their definitions used in tribology, tribology being defined as “the science and technology concerned with interacting surfaces in relative motion, including friction, lubrication, wear, and erosion” [224]. The following definitions based on G40-13 cover the key tribological terms used in this work.

B.1. Abrasion

Abrasion is “the process by which relative motion between a surface and hard particles or protuberances on an opposing surface produces abrasive wear of that surface.” Abrasive wear is “the result of hard particles or hard protuberances forced against and moving along a solid surface.” Hard particles can be debris detached from one of the sliding surfaces or particles stemming from a different source.

B.2. Adhesion

Adhesive wear is “wear due to localized bonding between contacting solid surfaces leading to material transfer between the two surfaces or loss from either surface.” The adhesive bonding is stronger than the local cohesive strength of the material. Galling is typically considered a severe form of adhesive wear. In some cases, adhesive wear can be beneficial when it favors the creation of a transfer film, whereby material is transferred from one surface to another, reducing the wear rate and/or coefficient of friction, as described in Chapter 4 of this doctoral thesis.

B.3. Coefficient of friction

The coefficient of friction (COF) is “the ratio of the friction force (F) between two bodies to the normal force (N) pressing these bodies together.”

$$\text{COF} = \frac{F}{N} \quad (20)$$

B.4. Debris

Debris is defined as “particles that have become detached in a wear or erosion process.” Depending on the type of contact and the debris evacuation system, debris may or may not play a role in the wear mechanism, including the formation of a transfer film.

B.5. Erosion

ASTM defines erosion as a “progressive loss of original material from a solid surface due to mechanical interaction between that surface and a fluid, a multicomponent fluid, or impinging liquid or solid particles.”

B.6. Galling

Galling is “a form of surface damage arising between sliding solids, distinguished by macroscopic, usually localized, roughening, and the creation of protrusions above the original surface; it is characterized by plastic flow and may involve material transfer.” The ASTM definition of galling does not refer to debris, and the ASTM G98 and G196 test specifications for evaluating galling resistance are based on extremely short tests generating very little if any debris.

B.7. Load-carrying capacity

The load-carrying capacity is the capacity of a surface to distribute peak stresses generated by localized loading to the base material, preventing plastic deformation. In this thesis, load-carrying capacity refers to the localized load, as discussed by Holmberg et al. [225]. This should be distinguished from the structural load-carrying capacity.

B.8. Plastic deformation

Plastic deformation occurs when the stress generated by the contact exceeds the yield strength of the material. Plastic deformation includes *plowing* for horizontal load (parallel to the surface) and *brinelling* for vertical load (perpendicular to the surface).

B.9. Sliding wear

Sliding wear is the wear due to the relative motion in the tangential plane of contact between two solid bodies. Sliding wear can produced *scoring*, which is a severe form of abrasion characterized by the formation of extensive grooves and scratches in the direction of sliding.

B.10. Spallation

Spallation is “the separation of macroscopic particles from a surface in the form of flakes or chips.” Two types of spallation are frequently reported in the literature: 1) spallation due to cohesive failure, which results from cracks propagating within a material; and 2) spallation due to adhesive failure, which results from cracks propagating at the interface between coating and substrate.

B.11. Wear

Wear is the “alteration of a solid surface by progressive loss or progressive displacement of material due to relative motion between that surface and a contacting substance or substances.” Mechanical solicitations can cause surface alteration by forming small debris (abrasion, erosion), by transferring material to another surface (adhesion, galling) or by resulting in permanent deformation (plowing, brinelling, eggshell effect). In addition, non-mechanical mechanisms are also considered as wear mechanisms such as corrosion (destruction of the passivation film), or melting / evaporation (flash temperature).